Detecting Ice Fabric and Englacial Structures with Phase-Sensitive Radar

Dissertation
der Mathematisch-Naturwissenschaftlichen Fakultät
der Eberhard Karls Universität Tübingen
zur Erlangung des Grades eines
Doktors der Naturwissenschaften
(Dr. rer. nat.)

vorgelegt von
Falk Marius Oraschewski
aus Bonn

Tübingen
2024

Gedruckt mit Genehmigung der Mathematisch-Naturwissenschaftlichen Fakultät der Eberhard Karls Universität Tübingen.

Tag der mündlichen Qualifikation: 27.02.2025
Dekan: Prof. Dr. Thilo Stehle
1. Berichterstatter/-in: Prof. Dr. Reinhard Drews
2. Berichterstatter/-in: Prof. Dr. Angelika Humbert

The pattern in the ice wall danced in the room,
the light shone more strongly.
Everything that should have been upright was
upside-down—everything was piercingly bright.
Not once did she think this was strange;
it was just as it should be.

— Tarjei Vesaas

ABSTRACT

Mountain glaciers and polar ice sheets are losing mass at accelerating rates in response to global warming. The rates of mass gain by snow accumulation and mass loss by calving and melting processes are primarily controlled by climatic factors. However, the flow dynamics of ice determine how fast mass is transported from accumulation to ablation zones. For this reason, ice dynamics are an important control on the stability and evolution of ice sheets and glaciers. Therefore, accurate parametrizations of ice-dynamical processes are essential for reliable projections of future mass loss and sea level rise. Ice dynamics imprint on ice fabric, which describes the orientation distribution of ice crystals, and on englacial structures, such as the stratigraphic layering of ice. These englacial features can be detected by radar as ice is highly transparent to radio waves. Consequently, past ice deformation can be inferred from radar data to study ice dynamical processes. This thesis presents two studies in which new acquisition methods for the phase-sensitive Radio Echo Sounder (pRES) are developed to detect the deep englacial stratigraphy of mountain glaciers and vertical ice fabric anisotropy.

In the first study, the pRES is mobilized to establish a phase-sensitive radar system suitable for deployment on mountain glaciers. A proof-of-concept survey conducted at Colle Gnifetti, Switzerland and Italy, demonstrates that the system can resolve the deep englacial stratigraphy, which could not be detected by previously deployed impulse radars. A layer-optimized synthetic aperture radar processing scheme is adapted to the mobile pRES data to suppress clutter and enhance the clarity of specular reflection horizons. In combination, these techniques enable the detection of englacial stratigraphy throughout essentially the entire ice thickness. This improvement is exemplified by the oldest reflection horizon that is continuously traceable in the acquired data, which has an age of $288 \pm 35\,\mathrm{a}$, compared to $78 \pm 12\,\mathrm{a}$, achieved in previous surveys. However, previously suggested ice-dynamically induced complex englacial structures, such as layer disturbances and englacial folds, could not be detected. Instead, the change in reflectivity is attributed to an increased deposition rate of acidic impurity layers in the upper ice, correlating with the onset of industrialization.

The second study focuses on detecting vertical ice fabric anisotropy through phase-based polarimetric wide-angle radar observations. Previous polarimetry studies typically employed nadir-looking antenna configurations, which are primarily sensitive to horizontal ice fabric anisotropy. These studies rely on the assumption that ice fabric is vertically aligned, a presumption that may not hold in complex flow regimes. Previous theoretical studies suggest that vertical ice fabric anisotropy and tilted ice fabric patterns can be inferred from polarimetric wide-angle radar surveys that feature oblique radio wave propagation. To test this approach, a polarimetric common midpoint radar survey was conducted on Ekström Ice Shelf, East Antarctica. The presented survey is sensitive to both vertical and horizontal ice fabric anisotropy, utilizing phase shifts between differently polarized radar waves caused by the anisotropy of the dielectric permittivity. An inversion framework is implemented to infer all relevant ice fabric components, indicating that ice fabric alone cannot explain the observed phase differences. Structural firn anisotropy is identified as an additional source of dielectric anisotropy that superimposes the ice fabric signatures. As the firn structure primarily impacts the vertical dielectric anisotropy, it has been neglected in previous nadir-looking polarimetry studies. By demonstrating that radar can measure firn anisotropy, this study suggests that targeted radar polarimetry can contribute to an improved understanding of structural firn anisotropy and provide ground-truth data for satellite remote sensing of firn.

In synthesis, the presented studies expand the application range of phase-sensitive and polarimetric radar and provide new perspectives for interpreting phase-sensitive radar data. However, both studies only represent first proof-of-concepts for these new acquisition techniques, paving the way for their broader application in future research to investigate complex ice dynamical processes. To foster these efforts, this thesis encourages the development of new radar systems that are specifically designed for detecting the newly identified radar targets.

ZUSAMMENFASSUNG

Gebirgsgletscher und polare Eisschilde verlieren als Reaktion auf die globale Erwärmung in zunehmender Geschwindigkeit an Masse. Der Massenzuwachs durch Schneeakkumulation und der Masseverlust durch Kalbung und Schmelzen werden in erster Linie durch klimatische Faktoren gesteuert. Die Fließdynamik des Eises bestimmt jedoch, wie schnell die Masse von den Akkumulations- zu den Ablationszonen transportiert wird. Aus diesem Grund ist die Eisdynamik ein wichtiger Einflussfaktor für die Stabilität und Entwicklung von Eisschilden und Gletschern. Daher sind genaue Parametrisierungen der eisdynamischen Prozesse für zuverlässige Vorhersagen über den künftigen Massenverlust und den Anstieg des Meeresspiegels unerlässlich. Die Eisdynamik prägt darüber hinaus die Eiskristallstruktur, welche die Orientierungsverteilung der Eiskristalle beschreibt, und englazialen Strukturen, wie die stratigraphische Schichtung des Eises. Diese Strukturen können durch Radare erfasst werden, da Eis eine hohe Transparenz für Radiowellen aufweist. Folglich kann aus Radardaten auf vergangene Eisverformungen geschlossen werden, um dynamische Prozesse im Eis zu untersuchen. Diese Arbeit präsentiert zwei Studien, in denen neue Erfassungsmethoden für ein phasensensitives Radar (pRES) entwickelt werden, um die tiefe englaziale Stratigraphie von Gebirgsgletschern und die vertikale Anisotropie der Eiskristallstruktur zu bestimmen.

In der ersten Studie wird das pRES mobilisiert, um ein phasensensitives Radarsystem zu erhalten, das für den Einsatz auf Gebirgsgletschern geeignet ist. Eine Proof-of-Concept-Studie, die am Colle Gnifetti, Schweiz und Italien, durchgeführt wurde, zeigt, dass das System die tiefe englaziale Stratigraphie abbilden kann, die von zuvor eingesetzten Impulsradaren nicht erfasst werden konnte. Ein schichtoptimiertes Verarbeitungsschema für das Radar mit synthetischer Apertur wird an die mobilen pRES-Daten angepasst, um Störsignale zu unterdrücken und die Klarheit der Reflexionshorizonte zu erhöhen. In Kombination ermöglichen diese Techniken die Erkennung der englazialen Stratigraphie über nahezu die gesamte Eisdicke. Diese Verbesserung wird durch den ältesten Reflexionshorizont veranschaulicht, der in den gewonnenen Daten durchgängig nachweisbar ist und ein Alter von $288 \pm 35\,\mathrm{a}$ aufweist, verglichen mit $78 \pm 12\,\mathrm{a}$, das in früheren Untersuchungen erreicht wurde. Allerdings konnten die zuvor vorgeschlagenen eisdynamisch geformten komplexen englazialen Strukturen, wie Schichtstörungen und englaziale Falten, nicht nachgewiesen werden. Stattdessen wird die Veränderung der Reflektivität auf eine erhöhte Ablagerungsrate säurehaltiger Verunreinigungen im oberen Eis zurückgeführt, die mit dem Beginn der Industrialisierung korreliert.

Die zweite Studie behandelt die Erkennung vertikaler Kristallanisotropie durch phasenbasierte polarimetrische Weitwinkelradarmessungen. Bisherige Polarimetriestudien verwendeten typischerweise Nadir-ausgerichtete Antennenkonfigurationen, die in erster Linie für horizontale Kristallanisotropie sensitiv sind. Diese Studien setzen die Annahme voraus, dass die Eiskristallstruktur vertikal ausgerichtet ist, eine Annahme, die in komplexen Eisflussregimen möglicherweise nicht gilt. Frühere theoretische Studien haben vorgeschlagen, dass die vertikale Anisotropie der Eiskristallstruktur und deren Neigung mittels polarimetrischer Weitwinkelmessungen mit schrägen

Einfallswinkeln der Radarwellen bestimmt werden können. Um diesen Ansatz zu testen, wurde auf dem Ekström-Schelfeis, Ostantarktis, eine polarimetrische *Common-Midpoint*-Radarmessung durchgeführt. Die vorgestellte Untersuchungsmethode ist sowohl für die vertikale als auch die horizontale Kristallanisotropie sensitiv. Diese wird über Phasenverschiebungen zwischen unterschiedlich polarisierten Radarwellen erreicht, die durch die Anisotropie der dielektrischen Permittivität verursacht werden. Es wird ein Inversionsverfahren eingesetzt, um alle relevanten Komponenten der Eiskristallstruktur abzuleiten. Dabei zeigt sich, dass die Kristallanisotropie die beobachteten Phasenunterschiede nicht alleine erklären kann. Die strukturelle Firnanisotropie wird als zusätzliche Quelle dielektrischer Anisotropie identifiziert, welche die Signaturen der Eiskristallstruktur überlagert. Da die Firnstruktur in erster Linie die vertikale dielektrische Anisotropie beeinflusst, wurde sie in früheren Polarimetriestudien mit Nadir-ausgerichteten Antennen vernachlässigt. Durch den Nachweis, dass Radar die Firnanisotropie detektieren kann, legt diese Studie nahe, dass gezielte Radarpolarimetriemessungen zu einem besseren Verständnis der strukturellen Firnanisotropie beitragen und Kalibrierungsdaten für die Satellitenfernerkundung von Firn liefern können.

Zusammenfassend lässt sich sagen, dass die vorgestellten Studien den Anwendungsbereich von phasensensitiven und polarimetrischen Radaren erweitern und neue Perspektiven für die Interpretation phasensensitiver Radardaten bieten. Beide Studien stellen jedoch nur erste Proof-of-Concepts für diese neuen Erfassungstechniken dar und ebnen den Weg für ihre Anwendung bei der Untersuchung komplexer dynamischer Prozesse im Eis in der zukünftigen Forschung. Um diese Bemühungen zu fördern, regt diese Arbeit die Entwicklung neuer Radarsysteme an, die speziell für die Erkennung der neu identifizierten Radarziele ausgelegt sind.

ACKNOWLEDGMENTS

I am deeply grateful to Reinhard Drews for welcoming me into the Geophysics Tübingen research group to pursue my PhD. You gave me the support and trust to develop my own project and secure my own funding, providing me with the freedom to focus on the research questions I found most intriguing, and helped me build scientific confidence and autonomy. Your guidance was invaluable, and you were always there when needed. I also truly appreciate your support for building connections in the community and your commitment to making things possible; most notably, the field campaigns to Colle Gnifetti and the Ekström Ice Shelf. During these campaigns, I was able to personally collect the data that form the foundation of this thesis.

I am further thankful to my second supervisor, Paul Bons. Listening to your enthusiastic explanations of folds and ice fabric not only taught me a lot but also always reminded me to not forget how great and fascinating science is. I also greatly appreciate your efforts to promote ethical practices and mental health in academia. I further thank Angelika Humbert for agreeing to review this thesis. The coincidence of meeting you on a train, while being on the way to Antarctica, was a memorable and enjoyable start into the expedition.

I am grateful to all the friendly people in the Geophysics Tübingen research group who not only do smart science, but also bake great cakes! Special thanks go to my PhD-office mates Clara, Leah and Reza for all the small and big help, and restorative distractions, that you provided over the past years. I particularly enjoyed traveling to Karthaus and Vernagtferner with Clara and spending almost three months in Antarctica with Reza, experiences which I will never forget. Thanks go to Inka for your unbreakable good mood while helping me organize the Colle Gnifetti campaign. In Tübingen, I have been privileged to work with so many great people that I cannot adequately express how grateful I am to each of you! Therefore, I just want to say a big thank you to Vjeran, Christian, Alexandra, Rebecca, Guy, Anne, Akash, Michael, Susanne, Greta, Pauline, Markus, Leonie, Julius and Jonas. Because of all of you, coming to the office was always something to enjoy.

I would also like to thank all the welcoming and open colleagues and friends in the glaciological community. Meeting you at the next conference is always a great motivation to keep going. Thanks go to Jonathan Hawkins for helping me with all my finicky radar questions and to Steven Franke for providing me with non-pRES radar data. I thank Anja Rutishauser for inviting me to join the fieldwork for her FYDRO project and Olaf Eisen, Nanna Karlsson and Nicholas Rathmann for many good suggestions over the past years.

Thanks to all my friends for helping me over the last four years to think about more than just ice, and for your understanding during the times when I still did.

Most of all, I sincerely thank my family, Annika, Monika and in particular my parents Claudia and Ralf. Their trust in me and my ideas gave me the freedom to discover the amazing research field of glaciology, allowing me to work on something I truly enjoy.

FUNDING

This PhD was funded through a scholarship provided by the Studienstiftung des deutschen Volkes. The field campaigns to Colle Gnifetti and Ekström ice shelf were funded by the Deutsche Forschungsgemeinschaft (DFG) Emmy Noether grant (DR 822/3-1) awarded to Reinhard Drews. I further acknowledge the logistic support from Neumayer-Station III for fieldwork on Ekström ice shelf (grant AWI_ANT_18).

PUBLICATIONS

FIRST-AUTHOR PUBLICATIONS WITHIN PHD

PUBLISHED

Oraschewski, F. M., Koch, I., Ershadi, M. R., Hawkins, J. D., Eisen, O., & Drews, R. (2024c). Layer-optimized synthetic aperture radar processing with a mobile phase-sensitive radar: A proof of concept for detecting the deep englacial stratigraphy of Colle Gnifetti, Switzerland and Italy. *The Cryosphere*, *18*(8), 3875–3889. https://doi.org/10.5194/tc-18-3875-2024

Oraschewski, F. M., Ershadi, M. R., & Drews, R. (2025c). Polarimetric wide-angle radar detects competing signatures of ice fabric and structural firn anisotropy. *Geophysical Research Letters*, *52*(14), e2024GL113096. https://doi.org/10.1029/2024GL113096

RESEARCH HIGHLIGHTS ARTICLE

Oraschewski, F. M. (2024b). Phase-sensitive radar measurements of glacial processes. *Nature Reviews Earth & Environment*, *5*(7), 485–485. https://doi.org/10.1038/s43017-024-00571-9

CO-AUTHOR PUBLICATIONS WITHIN PHD

Koch, I., Drews, R., Franke, S., Jansen, D., Oraschewski, F. M., Muhle, L. S., Višnjević, V., Matsuoka, K., Pattyn, F., & Eisen, O. (2023). Radar internal reflection horizons from multisystem data reflect ice dynamic and surface accumulation history along the Princess Ragnhild Coast, Dronning Maud Land, East Antarctica. *Journal of Glaciology*, 1–19. https://doi.org/10.1017/jog.2023.93

Ershadi, M. R., Drews, R., Tison, J.-L., Martín, C., Henry, A. C. J., Oraschewski, F. M., Tsibulskaya, V., Sun, S., Wauthy, S., Koch, I., Bons, P. D., Eisen, O., & Pattyn, F. (2025). Investigating the dynamic history of a promontory ice rise using radar data. *Journal of Glaciology*, *71*, e1. https://doi.org/10.1017/jog.2024.70

Moss, G., Višnjević, V., Eisen, O., Oraschewski, F. M., Schröder, C., Macke, J. H., & Drews, R. (2025). Simulation-based inference of surface accumulation and basal melt rates of an Antarctic ice shelf from isochronal layers. *Journal of Glaciology*, *71*, e44. https://doi.org/10.1017/jog.2025.13

Hills, B. H., Young, T. J., Lilien, D. A., Babcock, E., Bienert, N., Blankenship, D., Bradford, J., Brighi, G., Brisbourne, A., Dall, J., Drews, R., Eisen, O., Ershadi, M. R., Gerber, T. A., . . . Zeising, O. (2025b). Radar polarimetry in glaciology: Theory, measurement techniques, and scientific applications for investigating the anisotropy of ice masses. *Reviews of Geophysics*, *63*(4), e2024RG000842. https://doi.org/10.1029/2024RG000842

Bingham, R. G., Bodart, J. A., Cavitte, M. G. P., Chung, A., Sanderson, R. J., Sutter, J. C. R., Eisen, O., Karlsson, N. B., MacGregor, J. A., Ross, N., Young, D. A., Ashmore, D. W., Born, A., Chu, W., . . . Zuhr, A. (2025). Review article: AntArchitecture – building an age–depth model from Antarctica's radiostratigraphy to explore ice-sheet evolution. *The Cryosphere*, *19*(10), 4611–4655. https://doi.org/10.5194/tc-19-4611-2025

PUBLICATIONS OUTSIDE PHD

Oraschewski, F. M., & Grinsted, A. (2022). Modeling enhanced firn densification due to strain softening. *The Cryosphere*, *16*(7), 2683–2700. https://doi.org/10.5194/tc-16-2683-2022

The Firn Symposium team, Amory, C., Buizert, C., Buzzard, S., Case, E., Clerx, N., Culberg, R., Datta, R. T., Dey, R., Drews, R., Dunmire, D., Eayrs, C., Hansen, N., Humbert, A., . . . Wouters, B. (2024). Firn on ice sheets. *Nature Reviews Earth & Environment*. https://doi.org/10.1038/s43017-023-00507-9

CONTENTS

LIST OF FIGURES

ACRONYMS

AIS	Antarctic ice sheet
ApRES	Autonomous phase-sensitive Radio Echo Sounder
CMP	Common midpoint
COF	Crystal-orientation fabric
FFT	Fast Fourier transform
FMCW	Frequency-modulated continuous-wave
GNSS	Global navigation satellite system
GPR	Ground-penetrating radar
GrIS	Greenland ice sheet
HF	High frequency
IRH	Internal reflection horizon
LO-SAR	Layer-optimized synthetic aperture radar
MIMO	Multiple-input–multiple-output
pRES	Phase-sensitive Radio Echo Sounder
Radar	Radio detection and ranging
RES	Radio echo sounding
RTK	Real-time kinematic
Rx	Receiver
SAR	Synthetic aperture radar
SNR	Signal-to-noise ratio
TWTT	Two-way traveltime
Tx	Transmitter
UHF	Ultra high frequency
VHF	Very high frequency

PREFACE: PHASE-SENSITIVE RADAR MEASUREMENTS OF GLACIAL PROCESSES

PUBLICATION DETAILS

This chapter has first been published as a *Tools of the Trade* article by *Springer Nature*:

Oraschewski, F. M. (2024b). Phase-sensitive radar measurements of glacial processes. *Nature Reviews Earth & Environment*, *5*(7), 485–485. https://doi.org/10.1038/s43017-024-00571-9

AUTHORS AND AFFILIATIONS

Falk M. Oraschewski
Department of Geosciences, University of Tübingen, Tübingen, Germany.

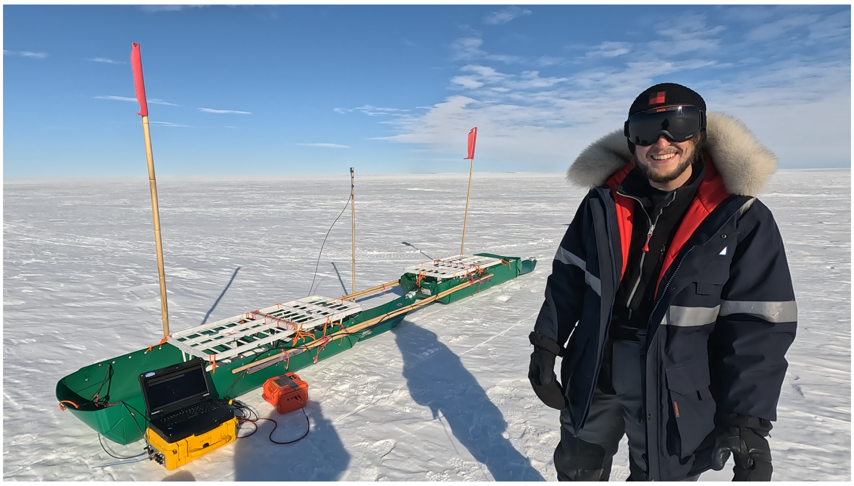

The stability and evolution of ice sheets, ice shelves and glaciers are determined by their mass balance and flow dynamics. The Antarctic ice sheet is surrounded by ice shelves, where mass is lost through iceberg calving at the ice shelf fronts and ocean-induced basal melting. The transport of mass by ice flow from the interior to the ice shelves is influenced by the ice fabric, which describes the distribution of the orientation of ice crystals. In situ data of basal melting and ice fabric are therefore needed to accurately predict ice sheet evolution. However, such data are scarce because conventional observation methods, such as ice coring, are time-intensive and expensive.

The Autonomous phase-sensitive Radio Echo Sounder (ApRES) overcomes these limitations. Like other ground-penetrating radars, it measures the two-way travel time of a radio wave to englacial reflection horizons or the ice–ocean interface. However, by transmitting frequency-modulated continuous radio waves that are mixed with the received signals, the ApRES achieves phase-sensitivity. Therefore, ApRES measurements are sensitive to travel time changes within a fraction of a wave period, which correspond to millimetre-scale changes in the reflector depth, enabling accurate measurements of englacial deformation and basal melt rates. Moreover, ice fabric can be inferred by rotating the polarized radar antennas to measure the polarization dependence of the radio wave propagation velocity.

ApRES measurements can be performed efficiently at multiple locations across large areas. For example, ApRES devices have been used to measure the basal melt rate and ice fabric across 120 km of the central flowline of the Ekström ice shelf. Additionally, stationary deployments provide high temporal resolution and coverage (hourly over the course of a year), facilitating the observation of dynamic processes such as tidal effects on basal melting or seasonally varying englacial deformation. ApRES devices are low cost and processing codes are open source. Therefore, similar surveys have been conducted by multiple research groups at many sites. The magnitude of available ApRES data has improved understanding of many glacial processes and facilitates their incorporation into ice flow models.

ACKNOWLEDGEMENTS The author thanks the German Academic Scholarship Foundation (Studienstiftung des deutschen Volkes) for Financial support through a doctoral scholarship. The Autonomous phase-sensitive Radio Echo Sounder (ApRES) was developed by the British Antarctic Survey (BAS) and University College London (UCL).

COMPETING INTERESTS The author declares no competing interests.

1

INTRODUCTION

1.1 MOTIVATION

Global ice masses are retreating and are dominant contributors to the projected global mean sea level rise of 0.43–0.84 m by 2100, relative to the period from 1986–2005 (IPCC, 2022). Mass loss of the global glaciers (Hugonnet et al., 2021; Rounce et al., 2023) affects the food and water security of up to 1.9 billion people (Immerzeel et al., 2020), endangers specialized species adapted to glacial conditions (Cauvy-Fraunié & Dangles, 2019), and increases the risk of natural hazards such as glacial lake outburst floods (Taylor et al., 2023). Although glaciers were the main contributor to sea level rise over the last century, 99 % of the global ice is stored in the polar ice sheets (IPCC, 2022). Both the Antarctic ice sheet (AIS) (The IMBIE team, 2018; Rignot et al., 2019) and the Greenland ice sheet (GrIS) (Bamber et al., 2018; The IMBIE Team, 2020) have been losing mass at accelerating rates in the past two decades, increasing their contribution to future sea level rise projections. The enhanced freshwater discharge from the polar ice sheets impacts marine ecosystems, for example, by altering biological productivity (Hopwood et al., 2020; Oksman et al., 2022). Moreover, it can substantially weaken global ocean circulation (He & Clark, 2022; An et al., 2024; van Westen et al., 2024).

1.1.1 MASS BALANCE OF GLACIERS AND ICE SHEETS

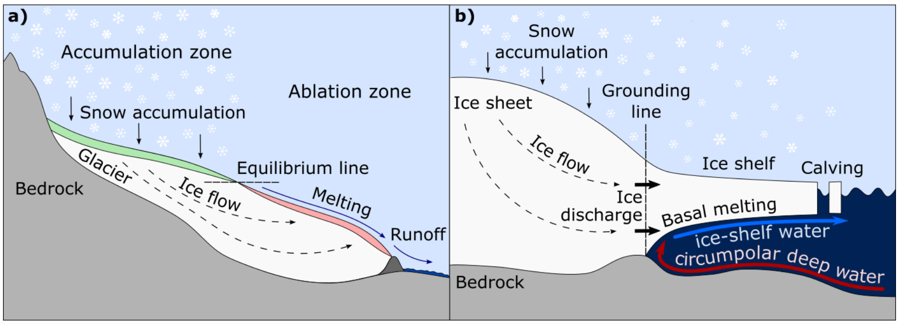

Figure 1.1: Mass balance configurations and dominant mass gain and mass loss processes of (a) mountain glaciers and (b) the Antarctic ice sheet.

The accelerating mass loss is set by fundamental glacial processes. A glacier is a large aggregation of snow that compacts into ice and deforms under its own weight, thereby transporting ice into a zone of ablation. For mountain glaciers in a stable climate, this results in an equilibrium configuration between mass gain in the accumulation zone and mass loss in the ablation zone, mostly by surface melting (Figure 1.1a). The two zones are separated by the equilibrium line, represented by the extent of the snow cover at the end of the ablation season. The equilibrium line altitude is primarily determined by climatic factors, including the snow accumulation rate and temperature (Huss & Hock, 2015).

The AIS exhibits a similar balance between predominant snow accumulation in the interior and mass loss at the floating ice shelves that surround it and buttress the grounded ice (Fürst et al., 2016; Reese et al., 2018). The mass loss occurs through basal melting (Wåhlin et al., 2024) and iceberg calving at the ice shelf edges (Figure 1.1b, Alley et al., 2023). The boundary between grounded and floating ice defines the grounding line. Ice flow across it is termed ice discharge, because once the ice becomes buoyant it contributes to sea level rise. Although grounding lines do not directly correspond to equilibrium lines, the lateral grounding line position is indicative of the ice sheet stability (Reese et al., 2023). Grounding line retreat is primarily attributed to oceanic forcing (Alley et al., 2015), which also correlates with increasing ice discharge (Davison et al., 2023). In contrast, the GrIS is drained by both land- and marine-terminating glaciers and has only a few remaining ice shelves (Millan et al., 2023). Accordingly, it represents an intermediate scenario between the mountain glacier and the AIS configuration.

1.1.2 IMPORTANCE OF ICE DYNAMICS

In all configurations, ice flow determines the rate of mass transport between the zones of predominant mass gain and mass loss. Therefore, the dynamics of ice flow are an important control on the stability of glaciers and ice sheets. The ice dynamics are defined by the rheology of the ice, which relates applied stress to induced strain. For ice, it is temperature-dependent, non-linear, and anisotropic (Glen, 1955; Azuma, 1994). Both the degree of non-linearity (Bons et al., 2018; Ranganathan et al., 2021; Millstein et al., 2022) and the evolution and impact of ice anisotropy (Richards et al., 2021; Llorens et al., 2022; Gerber et al., 2023; Kufner et al., 2023) are topics of ongoing glaciological research. Ice deformation imprints on englacial structures, such as the folding of englacial stratigraphy and the distribution of ice crystal orientations, also referred to as ice fabric (Hudleston, 2015; Jennings & Hambrey, 2021). Therefore, past ice flow can be inferred from observations of these structural features (Brisbourne et al., 2019; Koch et al., 2023).

However, ice fabric and the englacial structure also directly influence future ice deformation and cause internal dynamic feedback processes (Minchew et al., 2018; Jordan et al., 2022). In particular, mechanical ice anisotropy is induced by ice fabric in the first place. This means that the ice crystal orientations not only align according to flow (Llorens et al., 2022), but in turn cause direction-dependent softening of the ice (Duval et al., 1983; Gerber et al., 2023). The anisotropic rheology can promote further complex flow processes, such as large-scale englacial folding (Bons et al., 2016; Ross et al., 2020) and the localization of ice stream shear margins (Gerber et al., 2023; Jansen et al., 2024), where, in combination with shear heating, it can trigger further softening (Minchew et al., 2018). Consequently, ice anisotropy strongly influences ice flow in regions of fast-flowing ice that account for large portions of the AIS (Bamber et al., 2000) and GrIS (van den Broeke et al., 2009) mass loss.

Despite this importance, large-scale ice sheet models used for projecting the evolution of the polar ice sheets and their contribution to sea level rise do not routinely consider ice fabric anisotropy (e.g., Larour et al., 2012). They mostly define constant flow enhancement factors for different flow regimes to account for first-order variations in the viscosity (Winkelmann et al., 2011; Pollard & DeConto, 2012; Berends et al., 2022). However, ice flow is strongly sensitive to the enhancement factor (Humbert et al., 2005), and a constant factor does not capture its full spatial variability. This can be improved by the implementation of stress-adaptive enhancement factors (Ma et al., 2010; W. Wang et al., 2012; McCormack et al., 2022). Nevertheless, representing the aforementioned complex dynamical processes induced by ice fabric requires ice flow models that include a complex description of ice fabric anisotropy, such as a tensorial description (Gillet-Chaulet et al., 2006; Gagliardini et al., 2013; Lilien et al., 2021a; Henry, 2024). However, the applicability of these approaches is not only limited by their computational requirements and numerical instabilities, but also by a lack of ice fabric observations for constraining the models, particularly in fast-flowing ice.

1.1.3 GEOPHYSICAL OBSERVATIONS OF ICE FABRIC

The orientations of individual ice crystals, and therefore ice fabric, are directly observable in ice cores (Faria et al., 2014; Weikusat et al., 2017). However, they provide only limited spatial information. The azimuthal ice core orientation is usually not preserved for deep ice and can only be reconstructed under certain conditions (Westhoff et al., 2021). Moreover, with few exceptions (Stoll et al., 2021), ice cores are typically drilled at weakly dynamic ice domes and divides. At these ice core sites, deformation is primarily confined to vertical compression, and the ice fabric is not representative of flow regimes and evolution processes that occur in highly dynamic regions (Lilien et al., 2021a; Richards et al., 2023).

For these reasons, geophysical observations of ice fabric beyond ice core sites are needed. Ice fabric can be inferred by radar and seismics, which both complement each other (Brisbourne et al., 2019). Single active (Diez et al., 2014; Brisbourne et al., 2019) and passive (Smith et al., 2017; Kufner et al., 2023) seismic measurements can primarily infer the depth-averaged ice fabric anisotropy. Although this can be improved by long-time deployments of large passive seismic arrays or active-source borehole seismics (Lutz et al., 2020), the depth resolution remains limited. Yet, seismic methods are sensitive to both vertical and horizontal anisotropy via longitudinal compressional (P) and transversal shear (S) waves (Wittlinger & Farra, 2015). In contrast, radar-based ice fabric observations achieve a better depth resolution by detecting polarization-dependent traveltime delays and anisotropic scattering signatures from multiple englacial reflections (Dall, 2010; Jordan et al., 2019; Young et al., 2021a; Ershadi et al., 2022; Zeising et al., 2023). But as radio waves are transverse and radar is typically operated with quasi-monostatic antenna configurations in which transmitter and receiver are closely spaced, the sensitivity of radar to vertical anisotropy is limited.

In this thesis, I aim to develop and advance observational techniques for detecting ice fabric and englacial structures with phase-sensitive radio echo sounding. The following sections describe the dielectric properties of ice and the dielectric signatures of the main radar targets considered in this thesis: englacial stratigraphy, ice fabric, and structural firn anisotropy. Finally, the advancements by phase-sensitive radio echo sounding are described, providing improved detection capabilities for the considered radar targets.

1.2 DIELECTRIC PROPERTIES AND RADAR SIGNATURES OF ICE AND FIRN

1.2.1 WAVE PROPAGATION IN ISOTROPIC ICE AND FIRN

The suitability of radar for observing the interior of ice is set by the dielectric properties of ice, which make it highly transparent to radio waves. Radio waves in ice propagate according to the electromagnetic wave equation

$$\left(\nabla^2 - \frac{1}{c_{\text{ice}}}\frac{\partial^2}{\partial t^2}\right)\mathbf{E} = 0, \tag{1.1}$$

with the electric field $\mathbf{E}$ and time t. The radio wave velocity in ice

$$c_{\text{ice}} = \frac{1}{\sqrt{\mu_0 \varepsilon_0 \varepsilon_{\text{r}}}}, \tag{1.2}$$

is determined by the relative permittivity ε_{r}, with $\mu_0 \approx 4\pi \times 10^{-7}\,\text{H}\,\text{m}^{-1}$ and $\varepsilon_0 \approx 8.854 \times 10^{-12}\,\text{F}\,\text{m}^{-1}$ being the constant magnetic permeability and permittivity of free space, respectively. As ice is non-magnetic, its relative permeability is $\mu_{\text{r}} = 1$ and does not affect the radio wave velocity. The relative permittivity is complex-valued

$$\varepsilon_{\text{r}} = \varepsilon' - i\varepsilon'', \tag{1.3}$$

where both the real part, ε', and the imaginary part, ε'', depend on frequency, temperature, density, acidity, and ice fabric anisotropy (T. Matsuoka et al., 1997; Fujita et al., 2000).

Essentially, it is the real part that determines the radio wave velocity:

$$c_{\text{ice}} = \frac{c}{\sqrt{\varepsilon'}}, \tag{1.4}$$

where $c = 1/\sqrt{\mu_0 \varepsilon_0}$ is the speed of light in vacuum. At high frequencies (HFs) and above, i.e., above $3\,\text{MHz}$, variations of the real-valued permittivity in ice are low and ε' attains a value of approximately 3.17 for pure isotropic ice at temperatures of around $-20°\text{C}$. This value increases up to 3.19 for temperatures near the melting point (Fujita et al., 2000), corresponding to a reduction of the radio wave velocity.

In porous firn, consisting of an ice-matrix with air inclusions, the density is reduced and the real relative permittivity can be described by a mixture model for heterogeneous media (Looyenga, 1965):

$$\varepsilon'_{\text{firn}} = \left(\nu \varepsilon'^{1/3} + (1 - \nu)\right)^3, \tag{1.5}$$

where $\nu = \rho/\rho_{\text{ice}}$ is the ice–air volume fraction and ρ and ρ_{ice} are the densities of firn and glacial ice, respectively. This mixture model is in good agreement with the empirical relation determined by Kovacs et al. (1995):

$$\varepsilon' = (1 + 0.845\rho)^2. \tag{1.6}$$

The effects of dielectric anisotropy are described in Section 1.2.3.

The imaginary part of the relative permittivity is related to the electrical conductivity by

$$\sigma = \omega \varepsilon_0 \varepsilon'', \tag{1.7}$$

where $\omega = 2\pi f$ is the angular radio wave frequency and f is the frequency in Hz. The conductivity of ice at radio frequencies is generally low, with typical values on the order of $10^{-5}\,\mathrm{S\,m^{-1}}$ (Fujita et al., 2000). However, strong conductivity contrasts can occur at ice layers with high concentrations of acidic impurities, which is discussed in Section 1.2.2. Because of its low electrical conductivity, signal attenuation in ice is generally weak, particularly at low temperatures.

Similarly, scattering in ice is low because of the typically minor inhomogeneities. Exceptions include ice with entrained sediments (K. Winter et al., 2019; Franke et al., 2024) and temperate ice that has a temperature of $0°\mathrm{C}$ and contains liquid water inclusions (Eisen et al., 2009; Delcourt et al., 2013; Schannwell et al., 2014). The degree of scattering depends on the radio wave length. For this reason, radio waves with lower frequencies and longer wavelengths can penetrate deeper into the ice. In combination, the low scattering and low electrical conductivity of ice favor its high transparency to radio waves, making radar a powerful tool for studying the interior of glaciers and ice sheets.

1.2.2 ENGLACIAL RADIOSTRATIGRAPHY

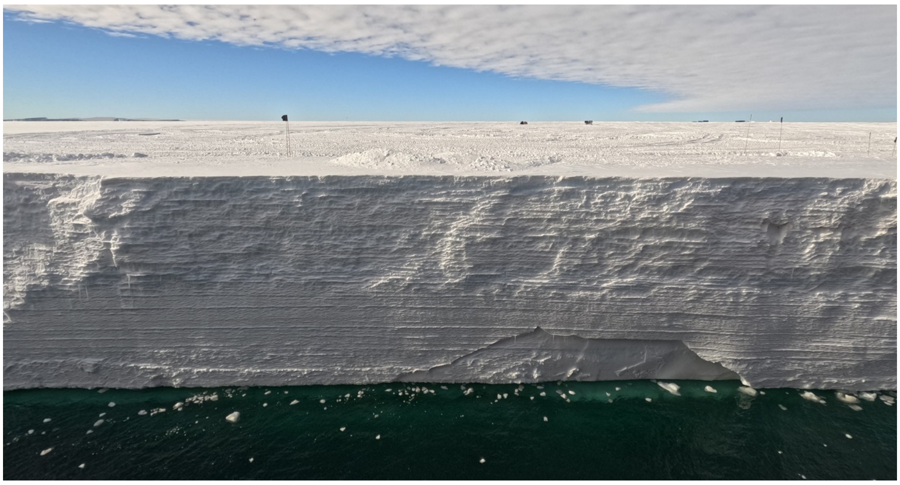

Figure 1.2: Englacial stratigraphy at the front of Ekström ice shelf.

Glacial ice is stratified when it originates from surface accumulation and has not undergone intensive deformation. The stratification evolves as new layers gradually build up during successive accumulation events. Individual ice layers are therefore isochronous and have differing properties, such as density, microstructure, and enclosed gas and impurity concentrations. Many of these properties are determined by the climatic conditions at the time when the snow accumulates at the surface or when the gases get enclosed in the ice. The climatic forcing varies on seasonal to orbital scales (Gow, 1965; Bender, 2002), which is archived in the ice. Ice coring can extract these climatic records and provide a dating of the ice (Rasmussen et al., 2013; Buizert et al., 2015; Mojtabavi et al., 2020).

Radar detects stratigraphic layers that alter the dielectric properties (Gudmandsen, 1975). The reflection amplitude of a specular horizon between two layers $n-1$ and n depends on the strength of the dielectric contrasts and can be computed by

$$r_n \approx \frac{Z_{n-1} - Z_n}{Z_{n-1} + Z_n}, \tag{1.8}$$

when changes in the impedance Z_n are small (Ackley & Keliher, 1979; Moore, 1988; Fujita et al., 2000). The impedance of the nth layer is given by

$$Z_n = \frac{i\mu_0\omega}{\gamma_n}, \tag{1.9}$$

where γ_n is the propagation constant:

$$\gamma_n = \sqrt{\varepsilon_0\mu_0\varepsilon_{\mathrm{r},n}\omega^2 + i\mu_0\sigma_n\omega}. \tag{1.10}$$

Here, $\varepsilon_{\mathrm{r},n}$ and σ_n are the relative permittivity and conductivity of the nth layer, respectively. Variations in both quantities are potential reflection sources.

In the firn, reflections primarily occur through permittivity variations induced by seasonal fluctuations in the layer density. In compacted glacial ice, reflection horizons are caused by conductivity contrasts due to acidic impurity layers. These layers can, for example, originate from volcanic deposits, providing distinct time markers and strong reflection horizons in the ice (Jacobel & Welch, 2005), which enable linking the radiostratigraphy with the ice core chronology (Eisen et al., 2004; Konrad et al., 2013; Bodart et al., 2021). Although the assumption that internal reflection horizons are isochronous is generally justified, ice slabs (Rutishauser et al., 2024) or abrupt changes in ice fabric anisotropy can also produce potentially non-isochronous reflection horizons (Fujita et al., 1999; Eisen et al., 2007).

Internal reflection horizons from strong volcanic events are detectable over hundreds of kilometers. Radar profiling can therefore provide spatial accumulation patterns (Cavitte et al., 2018; Karlsson et al., 2020), the depth of the glacial–interglacial transition (Karlsson et al., 2013), and the age-depth structure over large portions of the AIS (Cavitte et al., 2016; A. Winter et al., 2019; Z. Wang et al., 2023) and the entire GrIS (MacGregor et al., 2015). The spatially extended radiostratigraphy products are moreover a valuable resource for calibrating ice-sheet flow models (Born & Robinson, 2021; Sutter et al., 2021).

In addition to these spatial surveys, the englacial radiostratigraphy can be used to infer the ice-dynamic history (Elsworth et al., 2020; Koch et al., 2023) and to investigate complex ice-dynamic effects. For example, the structure of Raymond arches below ice domes and divides, caused by hardening of the ice due to its non-linear and anisotropic rheology, is an indicator for the stability of ice rises (Martín et al., 2009; Martín & Gudmundsson, 2012; Kingslake et al., 2014; Henry, 2024; Ershadi et al., 2025). Englacial folding of the stratigraphy can aid in inferring the age of ice streams (Jansen et al., 2024) or indicate ice stream shutdown (Holschuh et al., 2018; Franke et al., 2022). Moreover, large-scale folding induced by a variable ice rheology (Bons et al., 2016; Ross et al., 2020), sticky spots (Wolovick & Creyts, 2016), and basal freeze-on (Bell et al., 2011, 2014; Leysinger Vieli et al., 2018) are recorded in the englacial stratigraphy.

The latter features are observed in the deep glacial ice, in a zone that was considered radio echo-free in the past (Drews et al., 2009), before these structures could be revealed by advanced radar techniques (Section 1.3.2). Mountain glaciers exhibit a similar decrease in reflectivity in the deeper ice (Eisen et al., 2003; Bohleber, 2011; Konrad et al., 2013). Chapter 2 addresses how to improve the detection of the englacial stratigraphy of mountain glaciers.

1.2.3 DIELECTRIC ANISOTROPY DUE TO ICE FABRIC

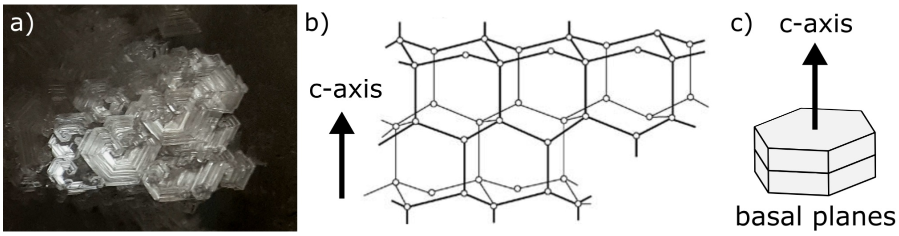

Figure 1.3: (a) Photo of hexagonal ice crystals. (b) Hexagonal ice crystal structure for ice Ih with white dots indicating oxygen atoms (adapted from Cuffey & Paterson, 2010). (c) Simplified illustration of an ice crystal with multiple basal planes.

Under the temperature and pressure conditions on Earth, natural ice occurs in the form of hexagonal ice Ih (Hansen, 2021), which is imprinted in the hexagonal shapes of snowflakes and ice crystals (Figure 1.3a). In this phase, individual ice crystals have a hexagonal lattice structure (Figure 1.3b), meaning that oxygen atoms in the basal plane of an ice crystal form hexagonal rings. The crystal c-axis points perpendicular to the basal plane. Single ice crystals have a strong mechanical anisotropy, because slip along basal planes is facilitated by a factor of at least 60 compared to c-axis-parallel deformation (Figure 1.4a–b, Duval et al., 1983). For this reason, the basal planes of ice crystals that are subjected to compressive strain rotate toward a stress-perpendicular orientation, and the c-axes align with the direction of maximum stress (Figure 1.4a–b).

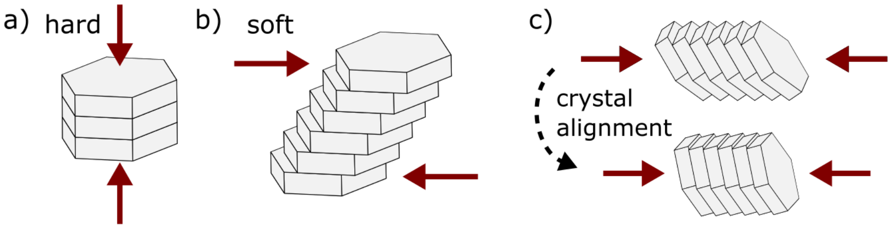

Figure 1.4: Deformation of ice crystals under compressive stress. (a) Compression along the c-axis. (b) Shear along basal planes. (c) Lattice rotation with c-axes alignment toward the direction of maximum compressive stress.

Glacial ice is polycrystalline, meaning that it consists of multiple ice crystals, in this context also termed ice grains. The bulk ice inherits the mechanical anisotropy of the individual ice crystals when they are preferentially oriented, resulting in direction-dependent softening or hardening of the ice. The preferential orientation patterns are termed ice fabric and evolve according to the experienced stress (Llorens et al., 2022). Crystal alignment occurs predominantly through lattice rotation, but additional recrystallization processes become significant under higher temperature and stress conditions (Montagnat et al., 2015; Fan et al., 2020).

The distribution of c-axes is described by the ice fabric tensor:

$$\boldsymbol{\lambda} = \begin{pmatrix} \lambda_1 & 0 & 0 \\ 0 & \lambda_2 & 0 \\ 0 & 0 & \lambda_3 \end{pmatrix}, \tag{1.11}$$

where $\lambda_1 < \lambda_2 < \lambda_3$ are the eigenvalues (following the ordering convention typically used in radioglaciology) which are normalized ($\lambda_1 + \lambda_2 + \lambda_3 = 1$).

A higher eigenvalue indicates that on average more c-axes are oriented toward the associated eigenvector directions $\boldsymbol{v}_1$, $\boldsymbol{v}_2$ and $\boldsymbol{v}_3$. Ice is isotropic when the c-axes are equally distributed ($\lambda_1 \approx \lambda_2 \approx \lambda_3 \approx 1/3$). This is often assumed for the near-surface, as snow precipitates with random orientation. Ice that has undergone deformation is generally anisotropic. Single-maximum fabrics ($\lambda_1 \approx \lambda_2 \ll \lambda_3$) are typically caused by vertical compression and present at the base of ice sheets. Vertical-girdle fabrics ($\lambda_1 \ll \lambda_2 \approx \lambda_3$) evolve by horizontal extension and occur for example in ice streams and ice shelves with flow acceleration along the flow path. As the ice fabric adapts to the flow regime that forms it, further deformation under the same flow regime is facilitated. However, the ice can be more resistant to deformation under a different flow regime, which can slow down its adaptation to changing flow conditions (Llorens et al., 2022).

Ice fabric anisotropy induces dielectric anisotropy, because electrons can be displaced more easily along the basal plane of an ice crystal than perpendicular to it, making its dielectric permittivity direction-dependent. For typical radar sounding frequencies and temperatures of around $-20°\mathrm{C}$, the dielectric permittivities of a single ice crystal parallel and perpendicular to the c-axis are $\varepsilon'_{\parallel} = 3.17$ and $\varepsilon'_{\perp} = 3.14$, respectively (Fujita et al., 2000; Bohleber et al., 2012). As electromagnetic waves are transversely polarized, a wave that propagates along the c-axis always experiences a dielectric permittivity of $\varepsilon'_{\perp}$. It will therefore propagate faster than a wave that propagates along the basal plane of the ice crystal with a polarization parallel to the c-axis. The corresponding dielectric anisotropy of a single ice crystal at $-20°\mathrm{C}$ is $\Delta\varepsilon' = (\varepsilon'_{\parallel} - \varepsilon'_{\perp}) = 0.034$, independent of the radio wave frequency (T. Matsuoka et al., 1997).

Polycrystalline ice inherits the dielectric anisotropy of the individual ice crystals. Its bulk dielectric permittivity is given by the second-order dielectric permittivity tensor and is linearly dependent on the ice fabric (Hargreaves, 1978):

$$\begin{aligned}\boldsymbol{\varepsilon}' &= \begin{pmatrix} \varepsilon'_1 & 0 & 0 \\ 0 & \varepsilon'_2 & 0 \\ 0 & 0 & \varepsilon'_3 \end{pmatrix} \\ &= \begin{pmatrix} \varepsilon'_{\perp} + \lambda_1 \Delta\varepsilon' & 0 & 0 \\ 0 & \varepsilon'_{\perp} + \lambda_2 \Delta\varepsilon' & 0 \\ 0 & 0 & \varepsilon'_{\perp} + \lambda_3 \Delta\varepsilon' \end{pmatrix}. \end{aligned} \tag{1.12}$$

In the general case of $\lambda_1 \neq \lambda_2 \neq \lambda_3$, ice is a dielectrically biaxial medium and the permittivity tensor describes an ellipsoid (K. Matsuoka et al., 2009; Jordan et al., 2020a). The propagation velocity of a radio wave that travels through the ice along an arbitrary ray path is given by the plane perpendicular to the ray path that cuts the ellipsoid through its center. This plane describes an ellipse with the two principal axes and their radii defining the two possible polarizations and their associated permittivities, respectively. A radio wave maintains its polarization when it is polarized parallel to one of the principal axes. When the polarization does not align, the wave is depolarized and split into two principal components (analogous to the ordinary and extraordinary waves in uniaxial crystals). The two wave components propagate independently and can be depolarized again when the ice fabric orientation changes along the ray path, resulting in different birefringence phenomena.

Radar is sensitive to the bulk dielectric properties of ice, because typically used radar wavelengths (decimeters to meters) are significantly larger than individual ice crystals (millimeters). Therefore, radar can infer the dielectric anisotropy of ice and, hence, the ice fabric. This is typically done by analyzing polarimetric birefringence patterns that can be observed using differently cross- and co-polarized radar antennas. Radar signatures originating from ice fabric are relative traveltime or phase-shifts between differently polarized radar waves (Dall, 2010; Jordan et al., 2019; Young et al., 2021a; Ershadi et al., 2022; Zeising et al., 2023) and extinction nodes and beat signatures that occur in the reflection power due to interference phenomena that are associated with these phase shifts (Fujita et al., 2006; K. Matsuoka et al., 2009, 2012; Li et al., 2018; Young et al., 2021b).

Previous polarimetry studies of ice fabric typically used quasi-monostatic radar configurations. Although the ice fabric can theoretically be arbitrarily oriented, these studies relied on the assumption that one ice fabric eigenvector (typically $\boldsymbol{v}_3$ associated with the highest eigenvalue) is vertical. This assumption holds particularly in the interior of the ice sheets, where single-maximum fabrics due to vertical compression occur (e.g., Jordan et al., 2019; Ershadi et al., 2022), but it may not be valid in complex flow deformation regimes.

1.2.4 DIELECTRIC ANISOTROPY DUE TO STRUCTURAL FIRN ANISOTROPY

Firn in the near-surface has an anisotropic structure, characterized by vertically elongated ice grains and pore spaces (Figure 1.5, Alley, 1987b; Pfeffer & Mrugala, 2002; Fujita et al., 2009). This structure forms in the uppermost $3\,\mathrm{m}$ (Hörhold et al., 2009; Lomonaco et al., 2011; Inoue et al., 2024) by insolation-driven temperature gradient metamorphism (Hutterli et al., 2009; Fujita et al., 2009). In addition to insolation, the degree of anisotropy depends on the accumulation rate and the local wind conditions. The accumulation rate determines the residence time of the firn in the near-surface (Hörhold et al., 2009), promoting stronger firn anisotropy at low-accumulation sites or during time periods of low accumulation. Wind-driven snow-compaction determines the initial snow properties, particularly the surface density, with more pronounced firn anisotropy developing in firn layers with initially higher density (Inoue et al., 2024). In combination, these factors cause a high spatial and temporal variability of firn anisotropy (Fujita et al., 2016; Inoue et al., 2024).

Firn densifies through multiple processes that are dominant at different firn densification stages. In stage I, densification occurs through rearrangement of ice grains by grain boundary sliding (Alley, 1987a; Schultz et al., 2022) until closest packing of grains is reached at the critical density of about 550 to $600\,\mathrm{kg\,m^{-3}}$. From there on, dislocation creep becomes the dominant densification process in stage II (Maeno & Ebinuma, 1983). Firn layers that originate from summer accumulation typically exhibit an initially higher density and finer grain sizes than winter layers and, therefore, develop a stronger structural anisotropy. As a result, grain rearrangement in the summer layers is slowed, while the initially low-density winter layers densify more quickly. This effect acts in conjunction with higher impurity concentrations that also enhance densification (Hörhold et al., 2012; Freitag et al., 2013; Fujita et al., 2014), resulting in a density crossing of both layer types around the critical density, where minimal density variability occurs (Freitag et al., 2004). In parallel, firn

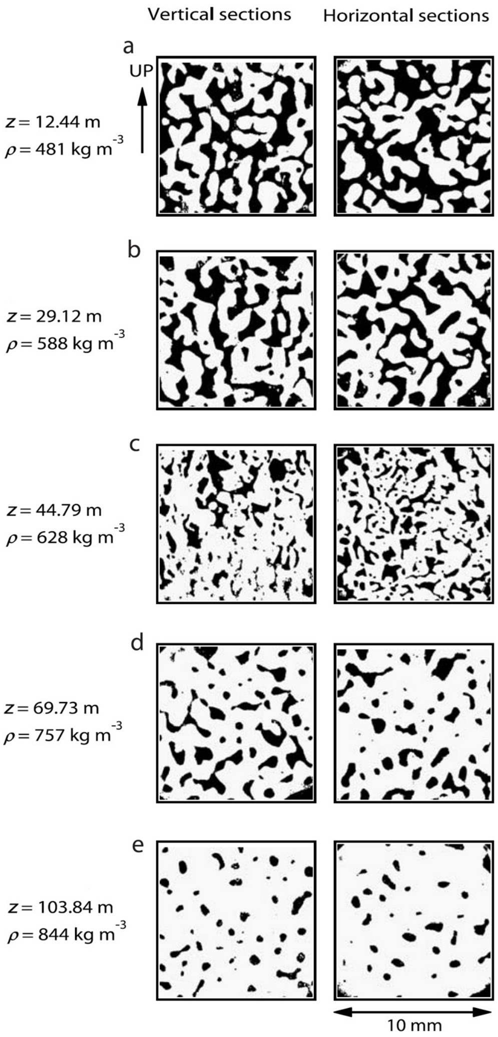

Figure 1.5: Vertical and horizontal X-ray absorption microtomography images of firn. Structural firn anisotropy due to elongated ice grains (white areas) and pore spaces (black areas) occurs in upper vertical sections (a–c). Lower (d–e) and horizontal sections show no structural anisotropy (Figure from Fujita et al., 2009).

anisotropy diminishes rapidly in stage I and more slowly in stage II (Fujita et al., 2014).

Although firn anisotropy decreases with depth, its imprint on the microstructure is preserved until pore close-off and affects the firn permeability (Fujita et al., 2009, 2014). In this way, firn anisotropy can influence the duration of the firn-to-ice transition and consequently the age difference $\Delta\mathrm{age}$ between ice and enclosed air bubbles (Keegan et al., 2019), the total air content and gas fractionations (Fujita et al., 2014). This facilitates inferring the past firn porosity at the firn–ice transition from the shape, size, and distribution of air bubbles in ice cores (Ueltzhöffer et al., 2010). In particular, firn anisotropy can explain the correlation between orbital tuning parameters, i.e., insolation, and total air content and the gas fractionation of oxygen and nitrogen ($\mathrm{O_2/N_2}$ ratio), observed by Bender (2002). Consequently, firn anisotropy is an important property for the analysis of ice core climate records.

Because ellipsoidal air bubbles affect radio wave propagation in firn and ice (Drews et al., 2012), firn structure is a source of dielectric anisotropy (Sihvola & Kong, 1988) and detectable by radar. Vertical firn anisotropy can be parametrized by the axial ratio $R_\mathrm{a} = l_\mathrm{v}/l_\mathrm{h}$ between the correlation lengths

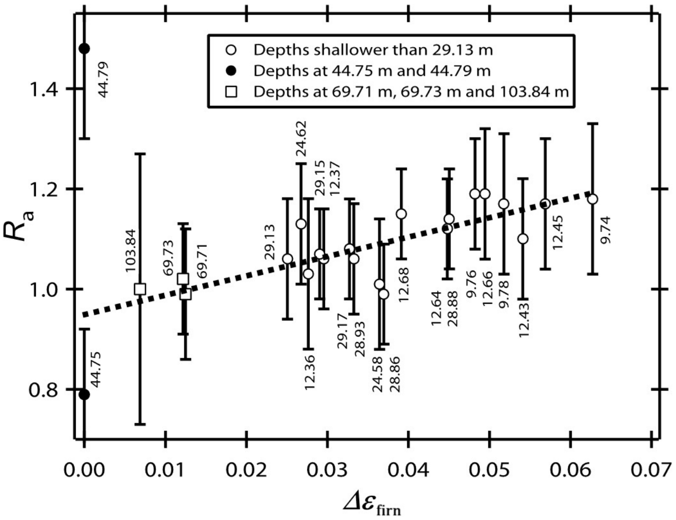

Figure 1.6: Relation between structural firn anisotropy described by the axial ratio R_a and the dielectric anisotropy $\Delta\varepsilon_\mathrm{firn}$. The residual $\Delta\varepsilon_\mathrm{firn} = 0.1$ at $R_\mathrm{a} = 1$ is suggested to be caused by ice fabric anisotropy (Figure from Fujita et al., 2009)

of vertical and horizontal structures, which is proportional to the induced dielectric anisotropy of firn $\Delta\varepsilon_\mathrm{firn}$ (Figure 1.6). Dielectric firn anisotropy can reach a value of 0.08 (Lytle & Jezek, 1994; Fujita et al., 2009), which is more than twice as big as the maximally possible dielectric ice fabric anisotropy of single-maximum fabrics ($\Delta\varepsilon' = 0.034$).

1.3 RADIO ECHO SOUNDING TECHNIQUES

Radioglaciology takes advantage of the radio-wave transparency of ice to investigate englacial and subglacial structures and properties of glaciers and ice sheets using ground-based or airborne radio detection and ranging (radar), also referred to as radio echo sounding (RES) (Robin, 1975; Schroeder et al., 2020). First experiments for determining the thickness of a glacier with electrodynamic methods were performed by Stern (1929). The broad application of RES in glaciology initiated in the 1960s after Waite and Schmidt (1962) demonstrated that pulsed radar altimeters used in aircraft can detect the ice base of a glacier. The main principle of RES is that a transmitter (Tx) emits a radio wave that propagates into the ice, where it gets reflected at subsurface targets, so that the multiple reflected signals arriving at the receiver (Rx) are recorded. Thereby, the range of a target is determined by the two-way traveltime τ of the reflected signal

$$R = \frac{c_\mathrm{ice}}{2\tau}. \tag{1.13}$$

In addition, the reflection amplitude comprises information about the target's reflectivity and geometry, as well as radio wave attenuation along the ray path.

Radar systems used in glaciology typically operate in the high frequency (HF) to lower ultra high frequency (UHF) range, i.e., at frequencies of about 3 MHz to 1 GHz. As penetration depth decreases at higher frequencies, HF and very high frequency (VHF) systems are typically used for imaging the entire ice column and the ice base, whereas UHF systems offer finer range resolution and are utilized for surveying the snow and firn.

This section describes the principles of different radio echo sounding techniques, starting with conventional pulsed or impulse systems, before highlighting the technical advancements provided by phase-sensitive RES.

1.3.1 PULSED AND IMPULSE RADAR

Pulsed radars transmit narrow-bandwidth pulse signals with pulse duration T_{pulse}, typically in the range of $10\,\text{ns}$ to $1\,\mu\text{s}$ (Schlegel et al., 2022). Their range resolution depends on the pulse duration:

$$\delta R_{\text{pulsed}} = \frac{c_{\text{ice}}\, T_{\text{pulse}}}{2}. \tag{1.14}$$

Very short pulses can only be achieved at UHF frequencies, which have a limited penetration depth, restricting the achievable range resolution of pulsed radars (Zirizzotti et al., 2010).

In contrast to pulsed radars, impulse radars transmit individual pulse signals, e.g., a single sine wave cycle or a Ricker wavelet, and have a wide bandwidth B as their short pulses contain energy over a wider frequency range (Navarro & Eisen, 2009). This is the technique used by commercial ground-penetrating radars (GPRs). Their range resolution is given by

$$\delta R_{\text{impulse}} = \frac{c_{\text{ice}}}{2B}. \tag{1.15}$$

For both the pulsed and impulse systems, the operating frequency is chosen as a compromise between penetration depth and range resolution. To probe several hundreds of meters deep into the ice, radars operating in the HF to VHF range are required, achieving resolutions on the decimeter- to meter-scale (Evans & Smith, 1969; Gudmandsen, 1969). This is not sufficient to measure relative reflection range changes between two spatially or temporally separated radar acquisitions, for example, to infer thickness changes of a glacier. These changes are often on the order of centimeters and require taking phase information into account. Phase-based radar systems can be phase-coherent or phase-sensitive. The two concepts are closely related and not always clearly distinguished in the literature. In the following, an overview of phase-based radar processing is given.

1.3.2 PHASE-COHERENT RADAR AND SYNTHETIC APERTURE RADAR PROCESSING

Phase-coherent radars transmit radio waves with a stable phase relationship and record the in-phase (I) and quadrature (Q) components of the received signal, preserving information about the amplitude and phase. The use of coherent radar systems in glaciology evolved in the 1990s (Raju et al., 1990; Gogineni et al., 1998; Rodriguez-Morales et al., 2014). Coherent radar data processing typically includes pulse compression and coherent integration (Navarro & Eisen, 2009).

In pulse compression, the received signal is correlated with a reference pulse for the transmitted signal. This improves the range resolution and signal-to-noise ratio (SNR), and effectively reduces the power requirements of the instrument (Navarro & Eisen, 2009; Zirizzotti et al., 2010).

Coherent integration of the received power improves horizontal resolution, particularly for point reflectors that appear as reflection hyperbolas in radar images. This method is also referred to as synthetic aperture radar (SAR) processing (Hamran & Aarholt, 1993; Leuschen et al., 2000; Legarsky et al., 2001; Paden, 2006; Peters et al., 2007; Hélière et al., 2007) and is closely related to migration techniques in seismics. The simplest form of coherent integration is unfocused SAR, describing the coherent summation of the power of subsequent radar traces. In focused SAR, the signal is corrected for the expected phase variation, and in migrated focused SAR the coherent integration of power is in addition performed across multiple range bins (Schroeder et al., 2019). Typically employed SAR processing techniques are matched filtering (Leuschen & Plumb, 2000; Hélière et al., 2007), back projection (Kusk & Dall, 2010; Xu et al., 2022), and frequency-wavenumber (f-k) migration (Stolt, 1978; Gogineni et al., 2001). Lastly, coherent along-feature SAR processing was introduced by Castelletti et al. (2017) specifically for detecting specular reflections, i.e., the englacial stratigraphy.

Phase-coherent radars in combination with SAR processing facilitate the imaging of deep structures in ice sheets in a zone that was previously considered radio-echo free (Drews et al., 2009), revealing signatures of complex flow, such as large-scale englacial folding (Bell et al., 2011, 2014; Bons et al., 2016; Leysinger Vieli et al., 2018). The phase-coherent radar systems deployed on polar ice sheets are typically heavy and are operated using tracked vehicles or aircraft, limiting their applicability in mountainous terrain. This is addressed in Chapter 2 by mobilizing a lightweight phase-sensitive radar, suitable for SAR processing.

1.3.3 PHASE-SENSITIVE RADIO ECHO SOUNDING

In phase-sensitive radars, the signal of the received wave is mixed with the transmitted signal. Thereby, the relative phase relationship between the two signals is obtained. Because of this, phase-sensitive radars do not strictly rely on transmitting radio waves with a stable phase relationship, which distinguishes phase-sensitive from phase-coherent radars. Nonetheless, when the two-way traveltime of the received radio wave to a reflector changes, the relative phase difference is equally modulated, and analogous processing methods can be applied. This approach was proposed by Nye et al. (1972) for measuring relative thickness changes of the AIS. A first phase-sensitive radar instrument was successfully deployed in the 1970s on ice caps in Arctic Canada to investigate the glacier bed using SAR techniques (Walford et al., 1977; Walford & Harper, 1981). Widespread use of phase-sensitive RES in glaciology was promoted by the development of the phase-sensitive Radio Echo Sounder (pRES, Corr et al., 2002) and the further developed Autonomous phase-sensitive Radio Echo Sounder (ApRES, Brennan et al., 2014), designed for measuring melt rates at the base of ice shelves (Jenkins et al., 2006; Nicholls et al., 2015). The ApRES is more robust and power-efficient than its precursor. It can be deployed autonomously to measure the temporal variability of basal melt in long-term deployments (Brennan et al., 2014). All experiments in this thesis are conducted with the ApRES. However, because the introduced survey methods are not autonomous, the instrument is hereafter referred to as pRES.

Most literature discusses the improvements of phase-sensitive radar processing in terms of the range resolution. However, the essential advantage of the pRES is that it can measure relative traveltime changes between two measurements with high precision. Therefore, the pRES is not only sensitive to the range, but also to the dielectric permittivity of the ice. This facilitates a multitude of acquisition techniques to infer different properties:

1. Spatial reflector range changes in combination with SAR processing can inform about the englacial and basal geometry (Young et al., 2018).
2. Temporal range changes provide basal melt rates (Marsh et al., 2016; Lindbäck et al., 2019; Vaňková et al., 2021; Zeising et al., 2022, 2024), englacial deformation rates (Kingslake et al., 2014, 2016; Vaňková et al., 2020a) and firn compaction rates (Case & Kingslake, 2022).
3. Incidence angle-dependent permittivity measurements provide the firn density (Arthern et al., 2013)
4. Temporal permittivity changes can inform about englacial hydrological processes (Vaňková et al., 2018).
5. Polarization-dependent permittivity measurements can infer the ice fabric anisotropy (Doake et al., 2002; Jordan et al., 2020a; Young et al., 2021b; Ershadi et al., 2022; Zeising et al., 2023).

This thesis expands this list by coherent radar profiling of englacial stratigraphy (Chapter 2) and wide-angle polarimetry (Chapter 3) to detect vertical ice fabric anisotropy and structural firn anisotropy.

1.3.4 PHASE-SENSITIVE RADIO ECHO SOUNDING WITH FREQUENCY-MODULATED CONTINUOUS-WAVE RADAR

The pRES is a frequency-modulated continuous-wave (FMCW) radar. In its standard configuration, it transmits a linear chirp with a bandwidth of $B = 200\,\mathrm{MHz}$, a center frequency of $f_\mathrm{c} = 300\,\mathrm{MHz}$, and a chirp duration of $T = 1\,\mathrm{s}$. This section describes the principles of phase-sensitive FMCW radars based on Brennan et al. (2014) for a single reflection.

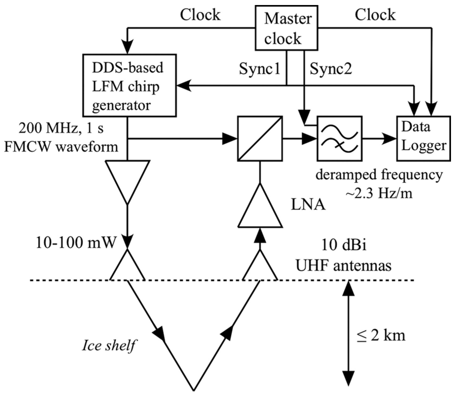

Figure 1.7: Simplified block diagram of the pRES. A linear frequency-modulated chirp is generated, and both the transmitted and received signals are mixed and low-pass filtered before the data logger stores the deramped waveform (Figure from Brennan et al., 2014).

The instantaneous frequency of the transmitted chirp is described by

$$f_\mathrm{t}(t) = 2\pi f_\mathrm{c} + K\left(t - \frac{T}{2}\right), \quad 0 \leq t \leq T, \tag{1.16}$$

where $K = 2\pi B/T$ is the sweep rate of the FMCW radar. The instantaneous phase is obtained by integrating the instantaneous frequency in time:

$$\phi_\mathrm{t}(t) = 2\pi f_\mathrm{c} t + \frac{Kt^2}{2} - \frac{KTt}{2} + \mathrm{const.} \tag{1.17}$$

The transmitted signal with amplitude A_t is then

$$s_\mathrm{t}(t) = A_\mathrm{t} \cos\big(\phi_\mathrm{t}(t)\big). \tag{1.18}$$

The received signal, reflected from a ground target at range R, arrives with a time delay $\tau = 2R\sqrt{\varepsilon'}/c$. Its corresponding instantaneous phase is

$$\phi_\mathrm{r}(t) = 2\pi f_\mathrm{c}(t-\tau) + \frac{K(t-\tau)^2}{2} - \frac{KT(t-\tau)}{2} + \mathrm{const.} \tag{1.19}$$

and the received signal can be described by

$$s_\mathrm{r}(t) = A_\mathrm{r} \cos\big(\phi_\mathrm{r}(t)\big), \tag{1.20}$$

with the reduced amplitude A_r.

In an FMCW radar, the transmitted and the received signals are mixed (Figure 1.7). Mathematically, this corresponds to a multiplication, which can be solved with the trigonometric product-to-sum identity:

$$\begin{aligned} s_\mathrm{t}(t)s_\mathrm{r}(t) &= A_\mathrm{t}A_\mathrm{r}\cos(\phi_\mathrm{t})\cos(\phi_\mathrm{r}) \\ &= \frac{A_\mathrm{t}A_\mathrm{r}}{2}\big(\cos(\phi_\mathrm{t}+\phi_\mathrm{r}) + \cos(\phi_\mathrm{t}-\phi_\mathrm{r})\big). \end{aligned} \tag{1.21}$$

The mixed signal consists of a high-frequency carrier wave (first term), which is modulated by the low-frequency envelope (second term). The envelope wave entails the essential information about the frequency and phase difference between the transmitted and received radio waves. It can be isolated by low-pass filtering (Figure 1.7), resulting in the deramped signal:

$$s_\mathrm{d}(t) = \frac{A_\mathrm{t}A_\mathrm{r}}{2}\cos(\phi_\mathrm{t}-\phi_\mathrm{r}). \tag{1.22}$$

The phase of the deramped signal is then:

$$\begin{aligned} \phi_\mathrm{d}(t) &= \phi_\mathrm{t}(t) - \phi_\mathrm{r}(t) \\ &= 2\pi f_\mathrm{c}\tau + K\tau\left(t - \frac{T}{2}\right) - \frac{K\tau^2}{2}. \end{aligned} \tag{1.23}$$

The second term represents the angular frequency of the envelope wave. It can be differentiated and divided by 2π to obtain the so-called deramped frequency that corresponds to a reflection with two-way traveltime τ:

$$f_\mathrm{d} = \frac{K\tau}{2\pi} = \frac{B\tau}{T} = \frac{2BR\sqrt{\varepsilon'}}{cT}. \tag{1.24}$$

During the FMCW signal processing (Section 1.3.6), the phase of the deramped signal is inferred at the center of the chirp. This center phase for $t = T/2$ is given by

$$\phi_\mathrm{c} = 2\pi f_\mathrm{c}\tau - \frac{K\tau^2}{2} = 2\pi f_\mathrm{c}\tau - \frac{\pi B\tau^2}{T}, \tag{1.25}$$

where the second term is negligible because f_c and B are on the same order of magnitude and $\tau \ll T$. The measured phase is therefore described by the term $2\pi f_\mathrm{c}\tau$. Conversely, this means that an FMCW radar is sensitive to small traveltime changes that are associated with relative phase shifts between two measurements, as given by

$$\Delta\tau = \frac{\Delta\phi_\mathrm{c}}{2\pi f_\mathrm{c}}. \tag{1.26}$$

1.3.5 DERAMPED WAVEFORM FOR MULTIPLE ENGLACIAL REFLECTIONS

In practice, an FMCW radar simultaneously receives echoes from multiple reflectors, each arriving after a different two-way traveltime τ_n. Figure 1.8a illustrates the frequencies of the transmitted chirp (Equation 1.16) and of three received signals for the first $0.5\,\mu\mathrm{s}$ of the chirp duration. The delayed return times of the received signals correspond to frequency offsets that are constant over the entire chirp duration. These frequency offsets are the deramped frequencies (Equation 1.24, Figure 1.8b). As all signals arrive simultaneously at the FMCW radar, it records a deramped waveform given by the superposition of all wave components that are associated with the deramped frequencies (Figure 1.8c). During FMCW signal processing, the frequency spectrum is obtained using a fast Fourier transform (FFT). Because the deramped frequency components correspond to two-way traveltimes τ or reflector ranges R, respectively, the obtained frequency spectrum directly represents a power spectrum in the traveltime or range domain (Figure 1.8d). In addition, the FFT provides the phase values of each reflection, which facilitates inferring relative traveltime changes between two measurements according to Equation 1.26.

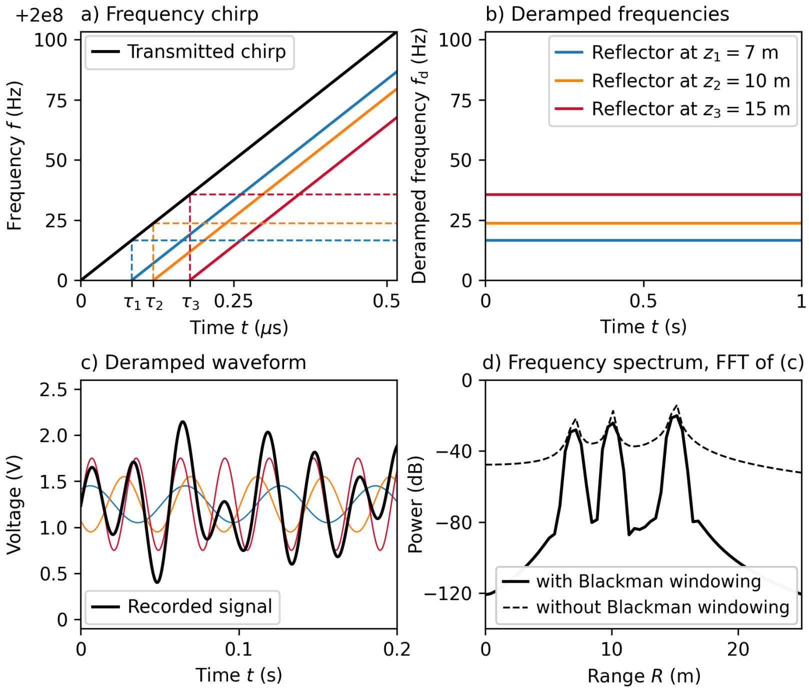

Figure 1.8: Illustration of FMCW radar principles for multiple reflections. (a) The transmitted chirp is linearly modulated. Received signals exhibit the same frequency relation, but arrive with a small time delay (Note the zoom into the first $0.5\,\mu\mathrm{s}$). (b) Differentiating the transmitted and received signals yields the deramped frequencies which are constant over the chirp duration. (c) The recorded deramped waveform is given by the superposition of the deramped wave components (Zoom into the first $0.2\,\mathrm{s}$). (d) During FMCW signal processing, the frequency spectrum is obtained, corresponding to a traveltime or range spectrum. Blackman windowing applied before FFT processing improves the dynamic range but causes a widening of the reflection lobes.

1.3.6 FMCW SIGNAL PROCESSING

Before the FFT processing can be applied, a few pre-processing steps are required (Figure 1.9). First, the deramped waveform is demeaned, and a Blackman window is applied to avoid spectral leakage and improve the dynamic range of the FFT output (Figures 1.8d, 1.9a–b). Next, the deramped waveform can be zero-padded in the time domain, meaning that zeros are appended to the signal to lengthen it by a padding factor p (Figure 1.9c). This is done because the discrete FFT samples the input signal with a frequency resolution of $\Delta f_\mathrm{d} = 1/T$, which corresponds to a range resolution of

$$\delta R = \frac{c}{2B\sqrt{\varepsilon'}}. \tag{1.27}$$

By increasing the length of the input by p, the signal is sampled at a higher rate of $\Delta f_\mathrm{d} = 1/pT$. No information is added through zero-padding, as it essentially corresponds to a sinc interpolation of the frequency spectrum. This means that it cannot improve the range resolution. Nonetheless, zero-padding provides a more detailed view of the decomposed signal, allowing features such as peaks in the frequency spectrum to be depicted more clearly. With zero-padding, the sampling rate of the decomposed signal in terms of the two-way traveltime is given by

$$\mathrm{d}\tau = \frac{1}{Bp}, \tag{1.28}$$

and in terms of the range by

$$\mathrm{d}R = \frac{\delta R}{p} = \frac{c}{2Bp\sqrt{\varepsilon'}}. \tag{1.29}$$

The final processing step before applying the FFT is a circular shift of the deramped waveform by $-T/2$ (Figure 1.9d). This step is required so that the FFT evaluates the phase of the deramped wave components at the center frequency, as given by Equation 1.25.

Eventually, FFT processing provides the amplitude and phase of the deramped frequency components that are associated with the traveltime bins

$$\tau_n = \frac{n}{Bp}. \tag{1.30}$$

The expected phase for a reflection with traveltime τ_n is

$$\phi_{\mathrm{ref},n} = \frac{n 2\pi f_\mathrm{c}}{Bp}. \tag{1.31}$$

Brennan et al. (2014) suggested subtracting this reference phase from the raw phase given by the FFT to obtain a corrected phase, representing a fine range offset relative to the range bin center. As noted in Chapter 2, this approach requires that the signals received in each range bin are independent of one another. In practice, strong reflections spread out over multiple bins (also without zero-padding) and exhibit an approximately stable phase over this range, indicating that the actual range resolution is worse than the theoretical value give by Equation 1.27. This can be explained by a widening of the reflection lobes due to the applied windowing (Figure 1.8d). This effect prevents obtaining independent fine range offsets for each bin. However, in Chapter 2, it is demonstrated that the depth-constant phase along reflectors, in combination with the reference phase correction, can be utilized to trace englacial reflection horizons.

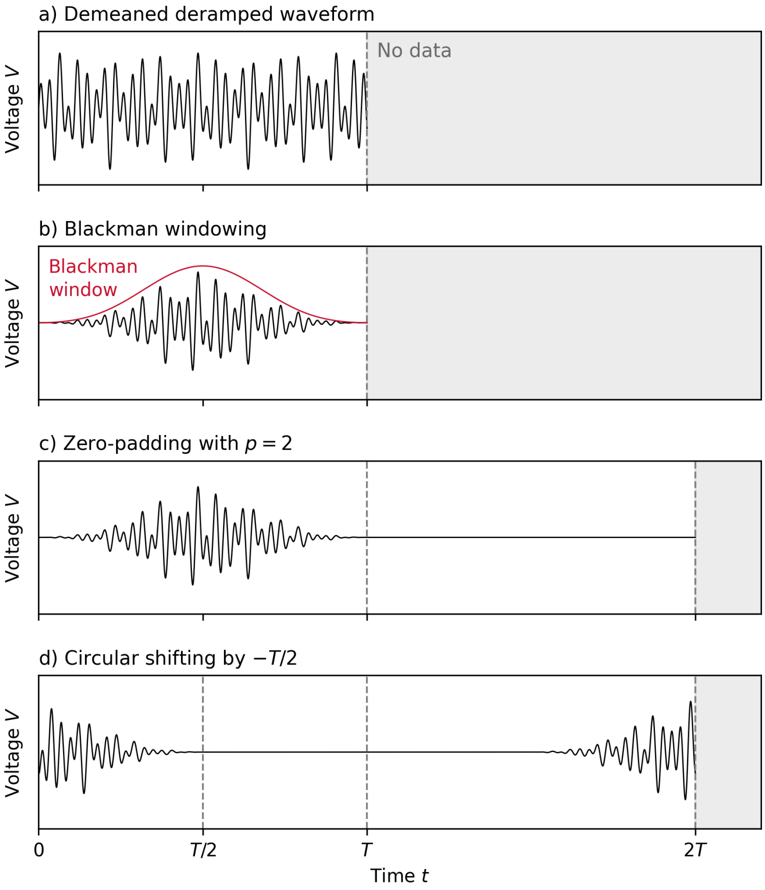

Figure 1.9: Pre-processing steps before FFT processing of the deramped waveform. (a) Demeaning of deramped waveform. (b) Blackman windowing to avoid spectral leakage. (c) Zero-padding to improve the sampling rate of the FFT. (d) Circular shifting to evaluate the phase of the wave components at the center frequency. (Figure adapted from Hawkins, 2023)

1.4 RESEARCH OBJECTIVES

This thesis addresses the overarching research question of how ice deforms in glaciers and ice sheets. I approach this question by developing new radar acquisition methods to detect ice fabric and englacial structures shaped by ice dynamics. This section presents the specific research objectives pursued in this work.

- **O1: Develop a method for detecting the deep englacial stratigraphy of mountain glaciers.** Previous GPR surveys conducted with conventional impulse radars often show the deep englacial stratigraphy of mountain glaciers as radio echo-free. In the past, radar images of polar ice exhibited a similar drop in backscattered power in the deep ice, which can now be resolved using phase-coherent radars and focused SAR processing techniques. Therefore, I hypothesize that phase-based radar techniques can also reveal the deep englacial stratigraphy of mountain glaciers. In Chapter 2, I aim to develop a radar method that is sensitive to structures in the deep ice and applicable to mountain glaciers.

- **O2: Investigate the deep stratigraphy and origin of the apparent echo-free zone at Colle Gnifetti.** Provided the developed method can detect the deep englacial stratigraphy of Colle Gnifetti, I will investigate the origin of the observed drop in reflectivity. I hypothesize that, unlike the typically flat stratigraphy near the surface, the deep englacial stratigraphy exhibits a more complex structure, affected by ice-dynamically induced buckling and folding. This is supported by a discontinuity in the age–depth structure observed by Hoffmann et al. (2018) in a Colle Gnifetti ice core. Observing these structures in alpine glaciers would offer an accessible, polar-equivalent study site for investigating complex ice-dynamical processes.

- **O3: Develop a phase-based radar technique for inferring vertical ice fabric anisotropy.** Polarimetric radar surveys are typically conducted in a quasi-monostatic radar geometry, which is particularly sensitive to horizontal ice fabric anisotropy due to permittivity-induced variations in wave propagation velocity. In these surveys, sensitivity to vertical ice fabric anisotropy is limited and can only be inferred through changes in the reflection ratio. In Chapter 3, I aim to develop a polarimetric wide-angle radar technique that is directly sensitive to vertical ice fabric anisotropy via variations in propagation velocity, as observed through phase shifts between differently polarized radar measurements.

- **O4: Implement an inversion method for the full ice fabric anisotropy tensor.** For analyzing polarimetric wide-angle radar surveys, I aim to implement an ice fabric inversion method that provides all eigenvalues without relying on the assumption that one ice fabric eigenvector is vertical. The combination of the wide-angle acquisition technique and the full ice fabric inversion method will provide a tool for detecting and investigating ice fabric anisotropy in complex flow regimes, where more variable and non-vertical ice fabric configurations may occur.

- **O5: Analyze the dielectric signatures of structural firn anisotropy.** Previous polarimetry studies neglected the influence of structural firn anisotropy. However, firn anisotropy needs to be considered in polarimetric wide-angle surveys as it primarily affects the vertical dielectric anisotropy. To understand its imprint on polarimetric surveys, I aim to analyze its signatures in the obtained polarimetric wide-angle data.

1.5 FIELD CAMPAIGNS

During the preparation of this thesis, I have participated in four field campaigns to acquire the underlying data. However, the studies presented here cover only a fraction of the performed experiments. This section provides an overview of the further surveys that were conducted.

COLLE GNIFETTI, SWITZERLAND/ITALY – SEPTEMBER 2021

Figure 1.10: Phase-coherent radar profiling in mountainous terrain with mobile pRES on Colle Gnifetti (Photo taken by Reinhard Drews).

For this first field campaign of my PhD, I have led the planning and organization. In addition to setting the scientific goals, I have organized the provisions, accommodations, logistics, and helicopter transport. In this campaign, Inka Koch, Reza Ershadi, Reinhard Drews, and I investigated the deep englacial stratigraphy of Colle Gnifetti by mobilizing the pRES, resulting in a first-author publication (Chapter 2, Oraschewski et al., 2024c). In addition to the radar profiling, we have acquired polarimetric radar data at multiple sites on the mobile pRES profile and a polarimetric common midpoint (CMP) next to the drill site of the KCC ice core.

HINTEREISFERNER, AUSTRIA – APRIL 2022

Figure 1.11: Performing reflection seismics to measure the thickness of Hintereisferner (Photo taken by Inka Koch).

This field campaign was conducted by the same field team. We acquired reflection seismics and polarimetric radar data on an across-flow profile ranging from the left margin to the center of the glacier. These surveys were conducted to measure the thickness of Hintereisferner and test the hypothesis that, despite of its low reflection power, the base of the glacier can be detected via the phase coherence of the basal return.

EKSTRÖM ICE SHELF, DRONING MAUD LAND, EAST ANTARCTICA – DECEMBER 2022 TO MARCH 2023

Figure 1.12: Mobile multiple-input multiple-output pRES survey for SAR processing of the englacial and basal structure of Ekström ice shelf acquired using the autonomous rover presented by Ershadi et al. (2024).

This three-month field expedition by Reza Ershadi and me was the second field season of the ReMeltRadar project. The central aim of the campaign was to acquire GPR and pRES radar data across Ekström ice shelf to infer spatial patterns of basal melt and to analyze the temporal evolution of basal terraces by repeated radar profiling.

The pRES repeat measurements of basal melt rates were acquired using a quad-polarimetric antenna setup mounted on two sleds for efficient deployment (shown in the Preface), which also provide ice fabric observations across the ice shelf. A study of this data, co-led by Clara Henry and me, is currently in preparation. In this study, we investigate the spatial, and thereby implicitly the temporal, evolution of ice fabric anisotropy by analyzing the ice fabric along the central flowline and across the shear margins of the ice shelf. As part of this study, I have obtained the depth-averaged ice fabric anisotropy from the polarization-dependent variations in the two-way traveltime of the basal reflection (Figure 1.13). These ice fabric data provide the basis for a data-model comparison experiment that considers various ice flow models and approaches for describing ice fabric evolution.

My main responsibility during the expedition was the acquisition of GPR data of the ice thickness and the englacial stratigraphy using the PulseEKKO radar system. I collected part of the GPR profile that was inverted in Moss et al. (2025) for accumulation rates and basal melt rates using a novel Simulation-Based Inference method. I moreover acquired VHF and UHF GPR data over kinematic wave structures (Figure 1.14) that occur along the central flowline of Ekström ice shelf, upstream of the grounding line. These structures are shaped by the interactions between ice flow and topographically induced variations in snow accumulation (Arcone et al., 2005, 2012; Ng & King, 2011), enabling us to study both processes.

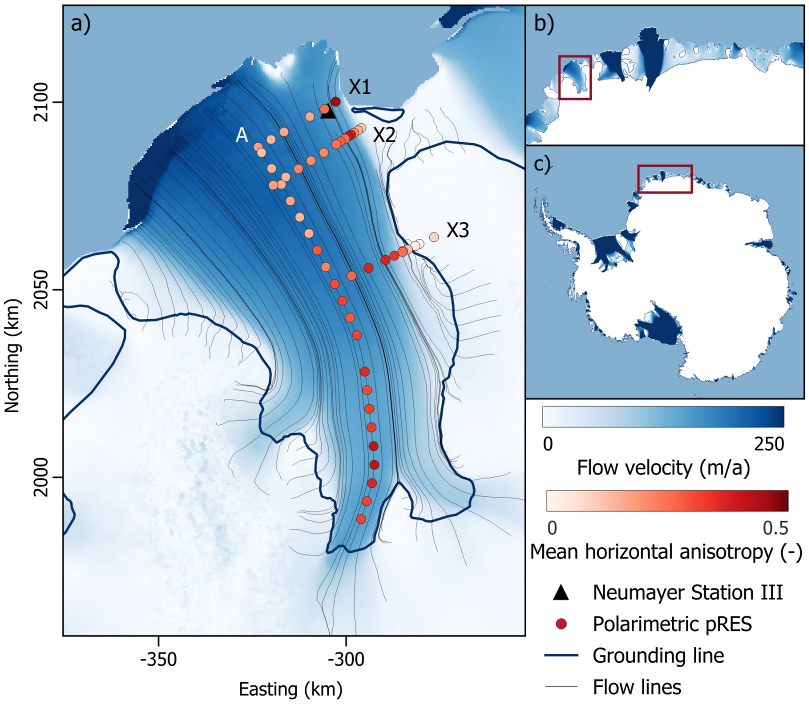

Figure 1.13: Depth-averaged horizontal ice fabric anisotropy inferred across Ekström ice shelf from polarization-dependent traveltime differences of the basal reflection in quad-polarimetric pRES data.

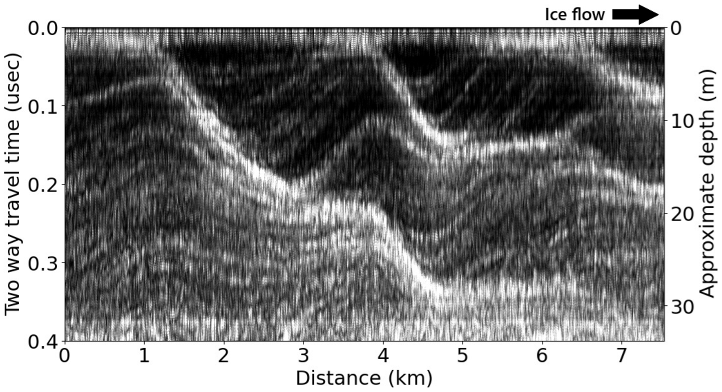

Figure 1.14: Kinematic wave structures observed upstream of the grounding line of Ekström Ice Shelf.

In addition to the main projects, I had the opportunity to conduct two experiments, which I designed myself. First, I acquired the polarimetric CMP survey presented in Chapter 3 to detect vertical ice fabric anisotropy. Second, I conducted a mobile pRES survey for SAR processing of englacial and basal structure that builds on the results of Chapter 2. This survey expands mobile pRES surveying to larger scales by employing a multiple-input multiple-output antenna configuration and an ice rover (Ershadi et al., 2024) for autonomous data acquisition (Figure 1.12).

NORTH-WEST GREENLAND – JUNE 2023

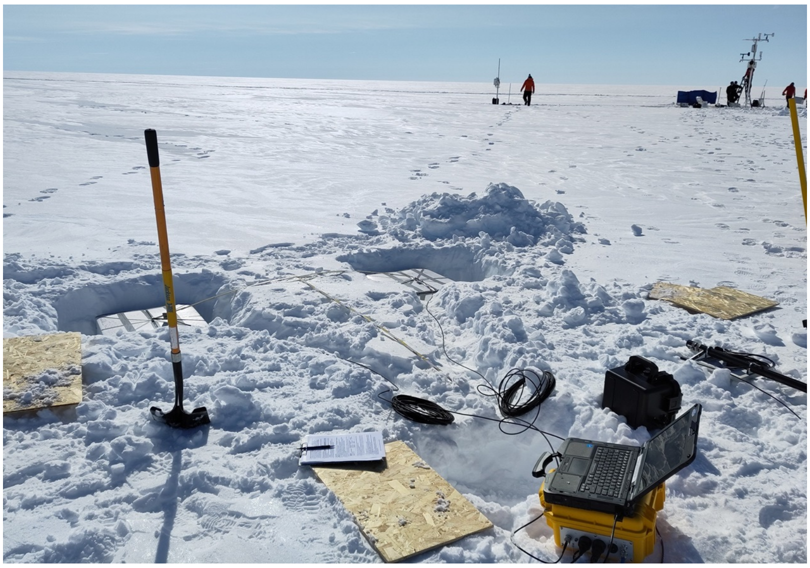

Figure 1.15: Preparation of long-term ApRES deployment at Camp Century, North-West Greenland.

At the invitation of the Geological Survey of Greenland and Denmark (GEUS), I participated in the 2023 GC-NET North-West Greenland campaign. As part of the FYDRO project led by Anja Rutishauser, Kirk Scanlan and I acquired quad-polarimetric pRES data and deployed an ApRES for long-term monitoring of englacial deformation and firn hydrological processes (Figure 1.15).

1.6 CO-AUTHOR CONTRIBUTIONS

- **Koch et al. (2023):** This study infers internal radar reflection horizons across three ice rises and intermediate ice shelves in Dronning Maud Land, East Antarctica. These data inform about the history of ice dynamics and surface accumulation in the climatically sensitive margins of Antarctica. I contributed to this study by co-developing the semi-automatic picking software to extract reflection horizons from multi-instrument radar data.

- **Ershadi et al. (2025):** This study analyses the flow dynamics of an East Antarctic promontory ice rise through radar and ice coring, with a focus on the impact of ice fabric. My contribution to this study was the extraction of vertical strain rates from repeat pRES measurements, supporting the analysis of englacial deformation. The vertical strain rates demonstrate hardening below the ice divide, which correlates with the vertical ice fabric eigenvalue and is a signature of the Raymond effect.

- **Moss et al. (2025):** This study develops an inversion method using Simulation-Based Inference to jointly extract surface accumulation and basal melt rates with uncertainties from internal reflection horizons. I contributed to this study by leading part of the radar data acquisition along a flow line of the Ekström ice shelf, picking reflection horizons, and performing the data curation.

- **Hills et al. (2025b):** This community review presents the state of the art in radiopolarimetric research. I acted as a co-author of the section on innovations in polarimetric surveying and provided the internal review for the section on the theory of wave propagation theory in anisotropic media.

- **Bingham et al. (2025):** This community review summarizes previous research on extracting the radiostratigraphy of the Antarctic ice sheet to support efforts for obtaining a continent-wide age-depth model. My contribution was to perform an internal review of the introduction, the background section on internal architecture, and the sections on glaciological applications.

2

LAYER-OPTIMIZED SYNTHETIC APERTURE RADAR PROCESSING WITH A MOBILE PHASE-SENSITIVE RADAR: A PROOF OF CONCEPT FOR DETECTING THE DEEP ENGLACIAL STRATIGRAPHY OF COLLE GNIFETTI, SWITZERLAND AND ITALY

PUBLICATION DETAILS

This chapter has been published in *The Crysophere*:

Oraschewski, F. M., Koch, I., Ershadi, M. R., Hawkins, J. D., Eisen, O., & Drews, R. (2024c). Layer-optimized synthetic aperture radar processing with a mobile phase-sensitive radar: A proof of concept for detecting the deep englacial stratigraphy of Colle Gnifetti, Switzerland and Italy. *The Cryosphere*, *18*(8), 3875–3889. https://doi.org/10.5194/tc-18-3875-2024

AUTHOR CONTRIBUTIONS

FMO led the data acquisition, analysis and writing of the paper. FMO, RD and OE designed the study outline and FMO, RD, IK and MRE conducted the data acquisition. JH supported the analysis of the data and designed Figure 2.1a. All authors contributed to the writing of the final paper.

Falk M. Oraschewski[1], Inka Koch[1], M. Reza Ershadi[1], Jonathan D. Hawkins[2], Olaf Eisen[3,4], Reinhard Drews[1]

[1]Department of Geosciences, University of Tübingen, Tübingen, Germany
[2]School of Earth and Environmental Sciences, Cardiff University, Cardiff, Wales, United Kingdom
[3]Alfred Wegener Institute, Helmholtz Centre for Polar and Marine Research, Bremerhaven, Germany
[4]Department of Geosciences, University of Bremen, Bremen, Germany

ABSTRACT

Radio-echo sounding is a standard technique for imaging the englacial stratigraphy of glaciers and ice sheets. In most cases, internal reflection horizons (IRHs) represent former glacier surfaces, comprise information about past accumulation and ice deformation, and enable the linking of ice core chronologies. IRHs in the lower third of the ice column are often difficult to detect or coherently trace. In the polar ice sheets, progress in IRH detection has been made by using multistatic, phase-coherent radars, enabling focused synthetic aperture radar (SAR) processing. However, these radar systems are often not suitable for deployment on mountain glaciers. We present a proof-of-concept study for a lightweight, phase-coherent and ground-based radar system, based on the phase-sensitive Radio Echo Sounder (pRES). To improve the detectability of IRHs we additionally adapted a layer-optimized SAR processing scheme to this setup. We showcase the system capability at Colle Gnifetti, Switzerland and Italy, where specular reflections are now apparent down to the base of the glacier. Compared to previously deployed impulse radar systems, with the mobile pRES the age of the oldest continuously traceable IRH could be increased from 78 ± 12 to $288 \pm 35\,\mathrm{a}$. Corresponding reflection mechanisms for this glacier are linked to stratified acidic impurities which in the upper part were deposited at a higher rate due to increased industrial activity in the area. Possible improvements to the system are discussed. If successfully implemented, these may provide a new way to map the deep internal structure of Colle Gnifetti and other mountain glaciers more extensively in future deployments.

2.1 INTRODUCTION

Polar midlatitude glaciers store information about past regional climate change (Wagenbach et al., 2012) and hold natural (Clifford et al., 2019) and anthropogenic (Gabrieli & Barbante, 2014; Sigl et al., 2018a) impurity records that can be extracted by ice-coring. Being located in the vicinity of highly industrialized regions (Sigl et al., 2018a), these archives are an important complement to ice core records from the polar ice sheets spanning deep time (EPICA community members, 2004; NEEM community members, 2013). However, the interpretation of these records can be limited by uncertainties in ice core dating (Jenk et al., 2009). Using radar surveys to laterally trace internal reflection horizons (IRHs) between multiple ice core sites, their chronologies can be compared to reduce uncertainties (Eisen et al., 2003; Bohleber, 2011; Licciulli et al., 2020). IRHs represent discontinuities of the dielectric permittivity or conductivity between different layers of ice. Permittivity is controlled through density and crystal-orientation fabric (COF), whereas conductivity is determined through acidity (Fujita et al., 2006). IRHs are isochronous when they are formed by seasonal snow-density variations or impurities that were initially deposited at the surface. Besides supporting the ice core dating, IRHs can be used to infer spatial accumulation patterns (Cavitte et al., 2018; Koch et al., 2023), past ice deformation (Drews, 2015; Koutnik et al., 2016) and upstream effects for ice core records (Eisen et al., 2003) and to find new ice core sites with an intact stratigraphy (Lilien et al., 2021b). In many of these applications the deep and old stratigraphy is of particular interest.

Both on mountain glaciers (Eisen et al., 2003; Konrad et al., 2013) and on polar ice sheets (Drews et al., 2009) the lowest third of the ice column is often difficult to image, for example due to increased radio-wave attenuation, weakening of density contrasts, or buckling and folding of reflection interfaces. For polar ice sheets, the emergence of phase-coherent radars and linked synthetic aperture radar (SAR) processing have significantly improved the detection of the deep englacial stratigraphy (Hélière et al., 2007; Peters et al., 2007). These heavy and power-intensive systems are pulled by tracked vehicles (Paden, 2006) or mounted on aircraft (Shi et al., 2010), neither of which are applicable on many mountain glaciers. Instead, smaller, typically incoherent, impulse ground-penetrating radars (GPRs) available in a variety of off-the-shelf products are used. Here, we address the need for a lightweight, low-power, phase-coherent and ground-based system suitable for SAR processing.

SAR processing improves the along-track resolution and suppresses clutter in the radargram by coherently focusing the backscattered power of point targets illuminated across multiple traces (Peters et al., 2005; Kusk & Dall, 2010). Similar to migration, this will collapse along-track hyperbolas from off-nadir reflections, providing improved imaging of, e.g., basal structures. However, in the case of specular reflections from IRHs, the signal quality can also deteriorate during SAR processing due to destructive interference (Holschuh et al., 2014). Castelletti et al. (2019) addressed this shortcoming by introducing a layer-optimized SAR (LO-SAR) processing method that corrects for along-track phase shifts in specular reflections before coherent summation. Other approaches for improving the detection of IRHs are based on filtering the IRH contribution in the azimuth frequency domain of the radargram (Heister & Scheiber, 2018) or on incorporating spatial correlation information into SAR processing (Xu et al., 2022). In addition, most of these algorithms determine the slope of IRHs, which can support the automated tracing of IRHs (MacGregor et al., 2015) and provide an alternative metric for radar data–model comparison (Holschuh et al., 2017).

In this study, we showcase a mobile, phase-coherent radar system that is suitable for SAR processing and can be deployed on mountain glaciers. We use the existing phase-sensitive radio-echo sounder (pRES, also ApRES for autonomous and stationary surveying), a lightweight, low-power and inexpensive frequency-modulated continuous-wave (FMCW) radar operating at 200–400 MHz (Brennan et al., 2014; Nicholls et al., 2015). This instrument has been widely used, most prominently in determining basal melt rates beneath ice shelves (Vaňková et al., 2021; Zeising et al., 2022) for which it was originally designed. Ershadi et al. (2024) presented a mobile acquisition of polarimetric pRES data using an autonomous rover to measure the COF on large spatial scales with postings of several tens of meters. The feasibility of using the pRES for profiling with sub-meter spacing has only theoretically been assessed by Kapai et al. (2022), who investigated artifacts that can arise from moving the pRES during data acquisition. Here, we present the first mobile deployment of the pRES for profiling and demonstrate its capability to detect deep IRHs that were unresolved in previous surveys. In the following, we first outline the mobile pRES setup and the data acquisition approach (Section 2.2) before describing the applied FMCW signal and LO-SAR processing (Section 2.3). In a proof-of-concept survey, mobile pRES radargrams are compared to GPR data from impulse systems and to available ice core data to interpret the imaged signatures in the glaciological context (Section 2.4). Finally, limitations of the mobile pRES are discussed including suggestions for further developments (Section 2.5).

2.2 MOBILE PRES

Coherent profiling with the pRES requires decimeter-scale postings with a relative positioning accuracy on the centimeter level. Here, we describe the hardware design and data acquisition approach for mobilizing the pRES, as applied in our proof-of-concept study (Section 2.4). Potential improvements to this system are discussed in Section 2.5.2.

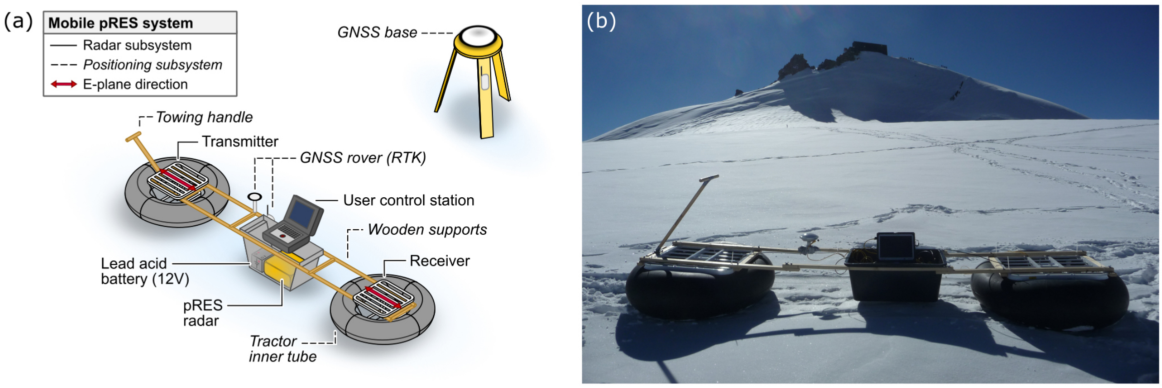

Figure 2.1: Mobile pRES setup with **(a)** a schematic of its components and **(b)** a photograph of the deployment on Colle Gnifetti.

2.2.1 HARDWARE DESIGN

To mobilize the pRES for profiling, we placed the transmit and receive skeleton slot antennas in inflated tractor inner tubes with the antennas separated by 2.7 m and elevated a few centimeters above the snow surface (Figure 2.1). Both antennas were oriented such that the E-plane was parallel to the profiling direction (also denoted as HH orientation). Positioning was controlled by the Trimble R9s global navigation satellite system (GNSS) receiver, operated in real-time kinematic (RTK) mode with the baseline between the GNSS base station and rover being typically below 200 m. This setup provided the relative position of the pRES to the base station with centimeter accuracy in real time. Both the positioning system and the pRES (operated in “attended mode”) were connected to a control station for automatic triggering of radar signal acquisition based on the position.

2.2.2 DATA ACQUISITION

In our survey, we used the standard configurations of the pRES, including a chirp time of 1 s. This makes data collection in stop-and-go mode necessary because moving the pRES during signal recording can cause Doppler blurring (Kapai et al., 2022), promote incoherent backscatter and increase system noise from cable movement. We therefore aimed to minimize the stopping time per point by first recording two and later only one chirp per point/trace. When two chirps were recorded, only the one with the lower noise floor was selected for further processing. Using the control station, chirping was triggered once the system was hand-towed by more than 9 cm, and audible signals indicated the operator to start/stop towing. With this approach, an average trace spacing of approximately $\Delta d = 13\,\mathrm{cm}$ and a median data acquisition time of 10 s per trace were achieved, giving a total survey speed of around 3 h per 100 m.

2.3 DATA PROCESSING

This section outlines the LO-SAR processing routine (Figure 2.2), starting with the standard FMCW signal processing and survey-specific adaptations which provide the background for estimating IRH slopes from the phase signal during the subsequent LO-SAR processing.

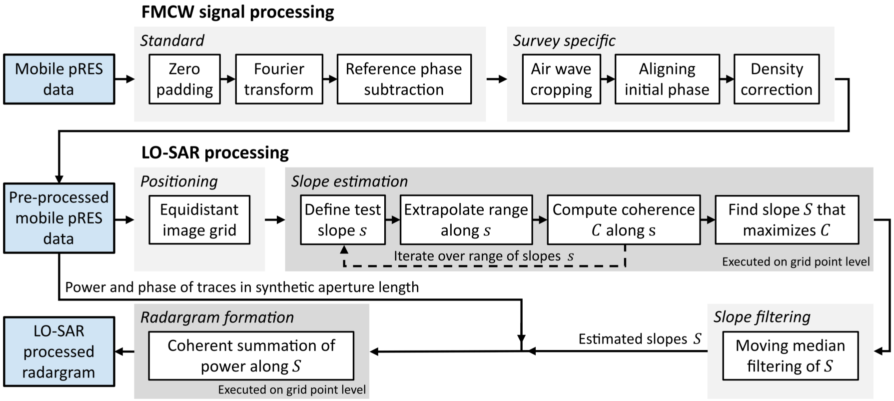

Figure 2.2: Overview of FMCW signal and LO-SAR processing scheme. Blue boxes represent the radar data at different processing stages. Gray blocks summarize the main processing steps, where a darker gray indicates that these are executed on the grid point level.

2.3.1 FMCW SIGNAL PROCESSING

The description of the standard FMCW signal processing and the notation broadly follow Brennan et al. (2014). The pRES transmits a linearly frequency-modulated chirp with a center frequency of $f_\mathrm{c} = 300\,\mathrm{MHz}$ and a bandwidth of $B = 200\,\mathrm{MHz}$ over a chirp time of $T = 1\,\mathrm{s}$. On the hardware side, the reflected signals are mixed with the transmitted signal and subsequently low-pass filtered. This results in the deramped waveform which, by using a fast Fourier transform (FFT), is decomposed into the deramped frequencies:

$$f_\mathrm{d} = \frac{2B\tilde{R}\sqrt{\varepsilon_\mathrm{r,ice}}}{Tc}, \tag{2.1}$$

which relate to the reflection range $\tilde{R}$ using the speed of light in vacuum c and the real-valued relative permittivity of ice $\varepsilon_\mathrm{r,ice} = 3.17$ (Brennan et al., 2014). Note that this formulation does not allow the use of a variable relative permittivity and the reflection range does not consider the lower density of firn (indicated by $\sim$). A density correction will be described below, and from here on, the general relative permittivity of firn or ice ε_r is used.

The range resolution δ_R of FMCW radars is determined by their bandwidth:

$$\delta_\mathrm{R} = \frac{c}{2B\sqrt{\varepsilon_\mathrm{r}}}, \tag{2.2}$$

giving a resolution of the pRES of $\delta_\mathrm{R} = 0.42\,\mathrm{m}$ in ice (Brennan et al., 2014). For each frequency component, or range bin n, the FFT returns the amplitude a_n (Figure 2.3c) and phase $\phi_{\mathrm{raw},n}$ (Figure 2.3a) in complex form:

$$A_{\mathrm{raw},n} = a_n \exp(i\phi_{\mathrm{raw},n}). \tag{2.3}$$

Prior to the FFT the deramped waveform is zero-padded, i.e., lengthened with zeros by a padding factor p. This increases the sampling rate of the FFT and reduces the range bin increment to $\Delta R_\mathrm{bin} = \delta_R/p$, effectively corresponding to a sinc interpolation of the decomposed amplitude and phase signals. Brennan et al. (2014) suggest using $p \geq 2$ for resolving ambiguities in the phase because otherwise the range bins are separated by more than a full phase cycle (or wavelength) at the center frequency of the pRES.

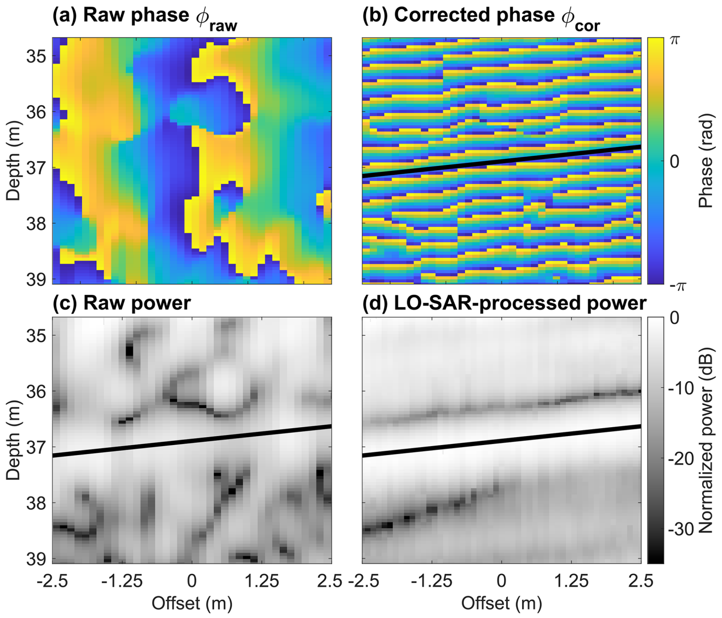

Figure 2.3: An example segment of the pRES profile over one synthetic aperture length. Phase signal before **(a)** and after **(b)** correction with the reference signal. Power before **(c)** and after **(d)** LO-SAR processing. The slope of the central reflection is indicated by a black line and obtained in **(b)** by fitting to a coherent section of the reference-corrected phase.

Note, however, that because zero-padding is essentially an interpolation, the intermediate phase cycles cannot be recovered. Nevertheless, the signal phase is typically interpreted relative to an idealized reference phase which, for the center of the nth range bin, is given by (Brennan et al., 2014)

$$\phi_{\mathrm{ref},n} = n\frac{2\pi f_{\mathrm{c}}}{Bp} - n^2\frac{\pi}{Bp^2T}. \tag{2.4}$$

The second term is negligible over the operation range of the pRES because $f_{\mathrm{c}} \gg 1/T$, so that $\Delta\phi_{\mathrm{ref,bin}} = 2\pi f_{\mathrm{c}}/(Bp)$. Therefore, $p \geq 2$ ensures that the phase variation in the reference phase between range bins is smaller than 2π. In addition, a high padding improves the representation of the reference phase, which is why we apply a padding factor of $p = 8$ for the subsequent LO-SAR processing.

Subtracting the reference phase ϕ_{ref} from the raw signal results in

$$\begin{aligned} A_{\mathrm{cor},n} &= a_n \exp(i\,(\phi_{\mathrm{raw},n} - \phi_{\mathrm{ref},n})) \\ &= a_n \exp(i\phi_{\mathrm{cor},n}), \end{aligned} \tag{2.5}$$

where the phase difference between raw and reference phase is denoted as the corrected phase ϕ_{cor}.

We note that the corrected phase appears constant along sloped IRHs (Figure 2.3b), which we will exploit during the following LO-SAR processing for estimating these slopes. The reason for this is that changes in the reflection range ΔR are directly related to changes in the raw phase (MacGregor et al., 2015):

$$\Delta\phi_{\mathrm{raw}} = \frac{4\pi\Delta R}{\lambda_{\mathrm{c}}}, \tag{2.6}$$

where $\lambda_{\mathrm{c}} = c/\left(\sqrt{\varepsilon_{\mathrm{r}}}f_{\mathrm{c}}\right)$ is the wavelength that corresponds to the center frequency. For sloped IRHs, this results in an along-track gradient of the raw phase between adjacent traces $\Delta\phi_{\mathrm{trace}}$ (Figure 2.3a) which is related to the IRH slope S by

$$S = \arctan\left(\frac{-\Delta R_{\mathrm{trace}}}{\Delta d}\right) = \arctan\left(\frac{-\lambda_{\mathrm{c}}\Delta\phi_{\mathrm{trace}}}{4\pi\Delta d}\right). \tag{2.7}$$

As the raw phase is approximately constant in the vertical (Figure 2.3a), the horizontal phase gradient due to a change in an IRH range by ΔR_{bin} is exactly compensated by the subtraction of the reference phase, causing the corrected phase to be constant along IRHs (Figure 2.3b).

In this study, we expand the standard FMCW signal processing by cropping the traces at the air wave return and shifting the phase at zero travel time to a uniform value. This accounts for spurious π offsets which appear in some of our traces for unknown reasons. Finally, we apply a density correction to account for faster radar wave propagation in firn, which can constitute a significant portion of the thickness of mountain glaciers, whereas the reflection range $\tilde{R}$ as given in Equation 2.1 is computed by assuming a constant permittivity of $\varepsilon_{\mathrm{r,ice}}$. To allow for a variable permittivity, $\tilde{R}$ is translated into two-way travel time $\tau = 2\tilde{R}\sqrt{\varepsilon_{\mathrm{r,ice}}}/c$ and then converted back into a density-corrected range R by

$$R(\tau) = \int_0^{\tau} \frac{c}{2\sqrt{\varepsilon_{\mathrm{r}}}}\,\mathrm{d}\tau', \tag{2.8}$$

using the relative permittivity ε_{r} as given by the Looyenga (1965) mixture model and density data from an ice core. This approach is justified because the permittivity of ice and air are approximately constant over the frequency range of the pRES (Bohleber et al., 2012).

2.3.2 LAYER-OPTIMIZED SAR PROCESSING

Castelletti et al. (2019) introduced LO-SAR processing to improve the detection of inclined IRHs in a radargram. This method aims to enhance the signal strength of IRHs by coherently integrating their backscattered power over a fixed synthetic aperture length L_{SAR}, where the signal-to-noise ratio (SNR) increases proportional to L_{SAR} (Castelletti et al., 2019). Because according to Equation 2.6 the phase varies in the along-track direction for inclined IRHs, it is necessary to correct for this phase gradient before the coherent integration to avoid destructive interference. In the implementation of LO-SAR processing of Castelletti et al. (2019), for each grid point on the radargram the backscattered power is integrated along its range bin over L_{SAR} after applying an iteratively found optimal phase shift that maximizes the SNR. Following Equation 2.7, this optimal phase shift then provides the local slope of IRHs as a byproduct.

Here, we tailor the LO-SAR implementation of Castelletti et al. (2019) to mobile pRES data, where we follow the different approach of first determining the englacial slopes before using these to perform the coherent integration directly along the IRHs. This has the two advantages that the slopes can be filtered prior to the coherent summation to remove outliers and that the spurious integration of signal power from nearby IRHs is avoided for any grid point on the radargram. A comparison between our approach, the original implementation and moving average filtering that does not correct for the phase gradient is provided in Figure A.1.

In our implementation, the LO-SAR-processed radargram is formed on an equidistant grid where the processed traces are located on a smoothed version of the observed profile line with a spacing of $10\,\mathrm{cm}$. The processing is done grid point by grid point. In the following, we characterize these points (x, z) by their positions x and depths z. For every position, all M observed traces within a distance of $L_{\mathrm{SAR}}/2$ are considered in the radargram formation. We use $L_{\mathrm{SAR}} = 5\,\mathrm{m}$, which gives a good improvement in radargram quality while ensuring that IRHs can be assumed to be linear over the full synthetic aperture length.

The local englacial slopes S at all grid points are determined first. Following MacGregor et al. (2015), these can in theory be inferred from the unwrapped along-track phase gradient, as given by Equation 2.7. However, this method directly translates uncertainties in the phase, e.g., due to occasional faulty traces and phase jumps at the transition between IRHs, into uncertainties in the slope, which in our data limits the accuracy of slope detection in this way.

We circumvent this problem by considering not only the phase gradient, but also the spatial coherence of the phase during slope estimation. For this we exploit the fact that the corrected phase is constant along IRHs (Figure 2.3b). In practice, we iterate for each grid point over a range of slopes s (from $-30°$ to $30°$ in steps of $0.2°$; a discussion of this range is provided in Section 2.5.3) to compute the coherence of the corrected phase along a line with length L_{SAR} and slope s, centered around (x, z). Its range at the M observed traces within the synthetic aperture length is given by

$$R_m(x, z, s) = z + (x_m - x)\tan(s), \tag{2.9}$$

with the position of the observed traces x_m. The corrected signal of the mth trace on that line $A_{\mathrm{cor},m}(x, z, s)$ is then obtained by weighting the values in the adjacent range bins above and below $R_m(x, z, s)$. Using these, we define the local phase coherence at (x, z) along slope s:

$$\begin{aligned} C(x, z, s) &= \left| \frac{1}{M} \sum_{m=1}^{M} \frac{A_{\mathrm{cor},m}(x, z, s)}{|A_{\mathrm{cor},m}(x, z, s)|} \right| \\ &= \left| \frac{1}{M} \sum_{m=1}^{M} \exp(i\phi_{\mathrm{cor},m}(x, z, s)) \right| . \end{aligned} \tag{2.10}$$

The slope along which the coherence is largest then gives the local englacial slope S:

$$S(x, z) = \arg\max_{s}(C(x, z, s)) . \tag{2.11}$$

This approach gives a more consistent slope estimate than the direct computation using Equation 2.7 but still may provide erroneous values at the interface between different IRHs. To remove these, we apply a moving median filter to the slope field using a filtering window of $2\,\mathrm{m} \times 2\,\mathrm{m}$.

Finally, the LO-SAR-processed radargram is obtained by coherent summation of A_{cor} along the determined slope S:

$$A_{\text{LO-SAR}}(x, z) = \left| \frac{1}{M} \sum_{m=1}^{M} A_{\mathrm{cor},m}(x, z, S(x, z)) \right| . \tag{2.12}$$

This defines the LO-SAR-processed amplitude $A_{\text{LO-SAR}}$ at each grid point (Figure 2.3d).

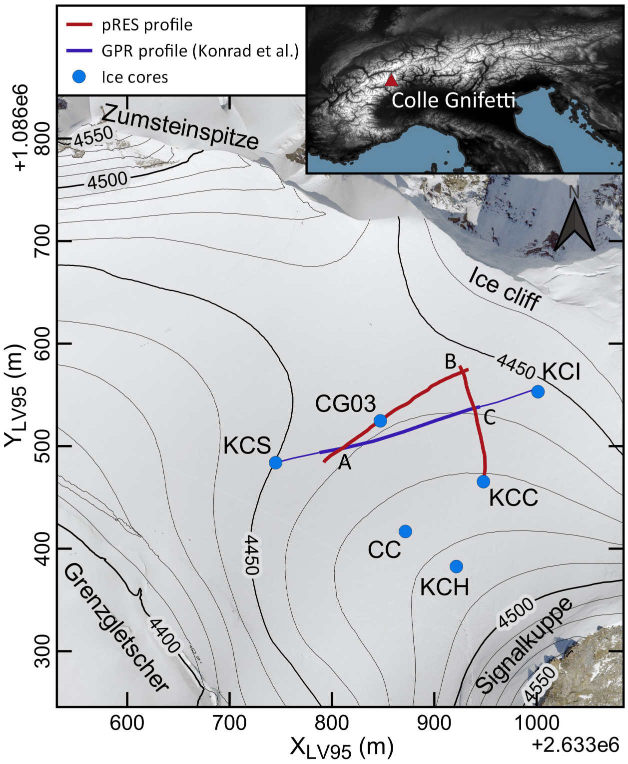

Figure 2.4: Overview of Colle Gnifetti indicating the location of the acquired mobile pRES profiles (red lines). The blue line marks a GPR profile from Konrad et al. (2013) that is used for comparison, with the thick part indicating the section shown in Figure 2.5a. The intersection points between the radar profiles are labeled (A–C), and blue dots mark ice core drill locations at the time of drilling. The inset shows the location of Colle Gnifetti within the European Alps. Source of orthophoto and local elevation model: Federal Office of Topography swisstopo. Source of global elevation model: NASA Shuttle Radar Topography Mission (2013).

2.4 PROOF OF CONCEPT AT COLLE GNIFETTI

The presented mobile pRES setup is tested in a proof-of-concept study which aims to image the deep englacial stratigraphy of Colle Gnifetti.

2.4.1 STUDY SITE

Colle Gnifetti is located in the Monte Rosa massif (Swiss–Italian Alps) at an altitude of around 4450 m a.s.l. and forms the upper accumulation zone of Grenzgletscher. It is characterized by low accumulation rates due to wind-driven snow erosion (Alean et al., 1983), englacial temperatures below 0°C (Hoelzle et al., 2011) and low horizontal flow velocities near the divide (Lüthi & Funk, 2000). In combination, these conditions favor the formation of the longest, still-well-preserved glacial climate record in the European Alps. Several ice cores have been drilled at the site (Figure 2.4), providing more than 1000-year-long climate and environmental records (Bohleber et al., 2018).

This study considers in particular the CG03 and KCC ice cores (Figure 2.4). CG03 was drilled in 2003 and analyzed by Sigl et al. (2018a) over its upper 57.2 m. Firn density data of CG03 were obtained by weighting ice core segments of ∼70 cm length (Michael Sigl, personal communication, 2023; Sigl et al., 2018b). In addition, ion concentrations of calcium, sodium, ammonium, nitrate and sulfate (Ca^{2+}, Na^{+}, NH_4^{+}, NO_3^{-} and SO_4^{2-}) were measured, with the record being extended at the top by the shallow core CG15, drilled at the same location in 2015 (Sigl et al., 2018a, 2018b). Using radiocarbon dating, Jenk et al. (2009) found indications of more than 10 kyr old ice at the base of the CG03 ice core, reaching potentially back into the last glacial period. The KCC ice core was drilled in 2013 at the southern flank of Colle Gnifetti. For this core, firn density data were obtained by X-ray computer tomography in $\sim 2\,\mathrm{mm}$ resolution (Freitag et al., 2018). The deep stratigraphy at KCC is moreover interesting because of a discontinuity in its chronology near the base, perhaps caused by englacial folding (Hoffmann et al., 2018).

2.4.2 DETECTION OF DEEP ENGLACIAL STRATIGRAPHY

The previous ice core drilling efforts at Colle Gnifetti were supported by radar profiling surveys to reveal the englacial stratigraphic structure and to link the different ice core chronologies (Eisen et al., 2003; Konrad et al., 2013). These surveys used conventional impulse GPR systems, for which the transect between the KCS and KCI ice cores (Figure 2.5a) from Konrad et al. (2013) is a representative example. In these studies, IRHs were mapped in the upper 30–50 % of the ice column, whereas the deeper ice appeared basically echo-free (Eisen et al., 2003). The deepest IRH detectable in the KCS–KCI transect had an age of $78 \pm 12\,\mathrm{a}$ at the time of data acquisition, which corresponds to the year 1930 CE. Note that Konrad et al. (2013) did not assign an age value to this IRH, and we repeated their approach for younger IRHs of averaging the KCS and KCI ages. In these data, the ice–bedrock interface is inconsistently detected and in some cases cannot be identified (e.g., Figure 3.8 in Bohleber, 2011).

In this proof-of-concept study, we aim to expand the depth range over which IRHs can be detected. In September 2021, we acquired 285 m of phase-coherent radar data using the mobile pRES (Figure 2.4). It is divided into a 166 m long profile across the saddle that passes the CG03 ice core and intersects with the KCS–KCI transect by Konrad et al. (2013) and a second 119 m long upstream profile towards KCC (south). Already in the raw mobile pRES data ice and bedrock are clearly distinguishable, and deeper IRHs than previously observed are visible (Figure 2.5c). In parts these IRHs are yet difficult to trace due to persistent speckle noise and because their quality deteriorates in the flanks of the saddle where they are more inclined. For these reasons, LO-SAR processing is applied as described in Section 2.3.2. In this process the IRH inclination relative to the surface is quantified, and values of about 10° are attained at both ends of the across-saddle profile (Figure 2.5b). The LO-SAR-processed data reveal deep IRHs which were not apparent in the previous surveys (Figures 2.5d and A.1).

In the second profile collected upstream towards KCC (Figure 2.5e–f), LO-SAR processing also reveals the presence of deep specular reflections. However, in this part the quality of our data got diminished by technical problems during data acquisition, which might have arisen from overexerting the data writing capacity of the pRES after collecting more than 1000 individual traces in a single folder. Thereby, various later recorded traces were lost or showed an enhanced noise level. In addition, this profile might have been affected by a less stable positioning of the mobile pRES system at each point due to the increased surface slope. As a consequence, deep IRHs in the upstream profile are disturbed and not continuously traceable, which prevents studying

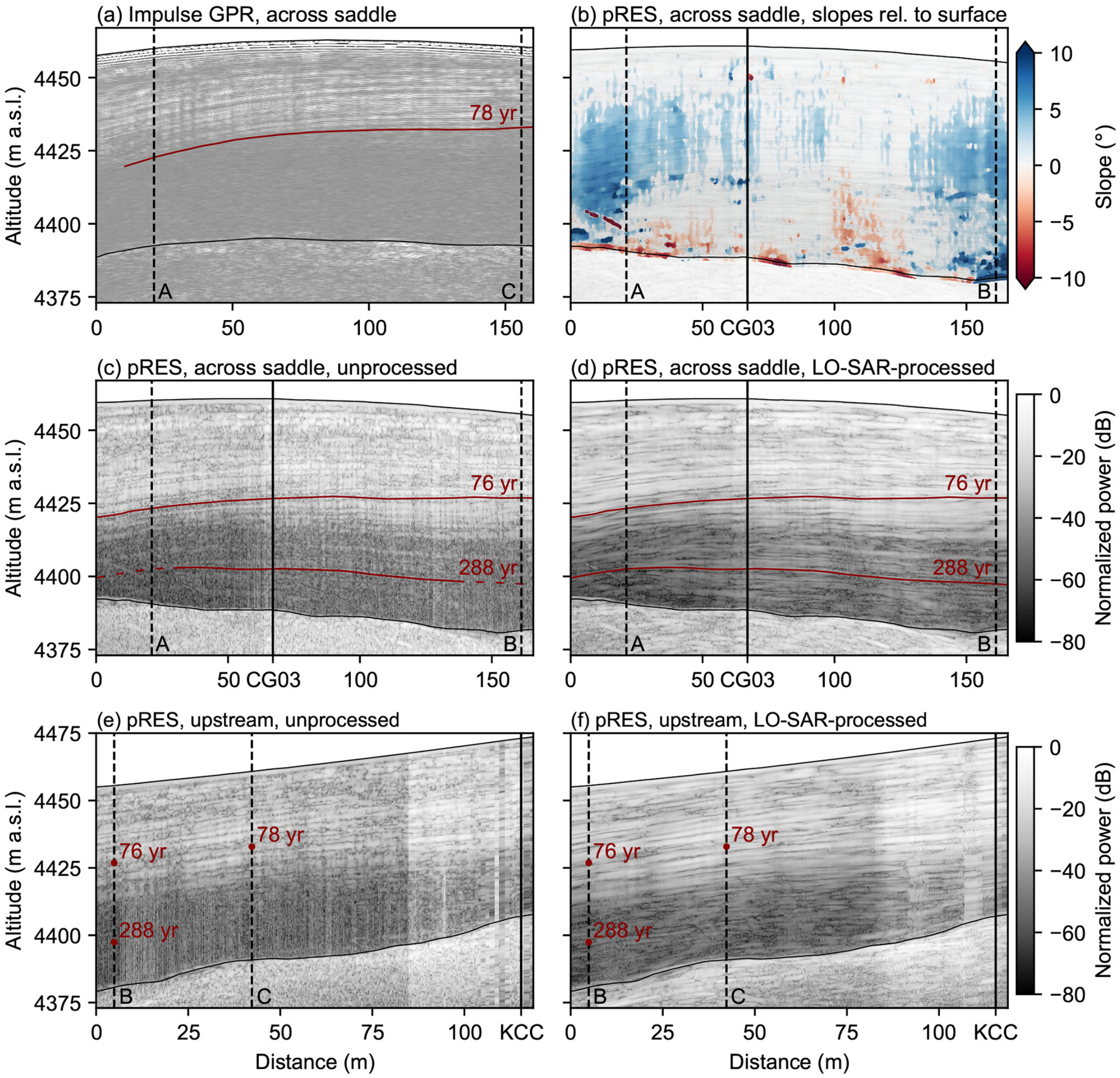

Figure 2.5: Comparison of radargrams **(a–d)** across Colle Gnifetti and **(e–f)** upstream towards KCC. **(a)** Radar data of an impulse GPR (Konrad et al., 2013); **(b)** IRH slopes relative to the surface derived from the corrected phase of the mobile pRES data; **(c, e)** mobile pRES data before and **(d, f)** after LO-SAR processing. The CG03 and KCC ice core locations are marked by vertical black lines, and the intersection points between the three profiles are denoted (A–C) and marked by dashed black lines. Red lines mark traced IRHs. In the upstream profile **(e–f)**, the continuous tracing of deep IRHs is prevented by lower data quality, and red dots only indicate traced IRHs in the intersecting profiles.

the potentially complex deep stratigraphy at KCC and reduces the capability of our data to link the CG03 and KCC ice cores.

For assessing the general potential of the mobile pRES, we therefore focus on the across-saddle profile. In this radargram, we trace two IRHs for comparison with the deepest IRH that was detectable in previous studies (Figure 2.5). The first IRH matches the 78 a horizon in the impulse GPR data with respect to depth at the intersection between both profiles, and the second one marks the deepest reflection that is continuously traceable in the LO-SAR-processed across-saddle radargram.

The two IRHs are dated by converting their range into units of meters water equivalent to link them with the age–depth model of Jenk et al. (2009) for the CG03 ice core that is located on the profile (Figure 2.6). Uncertainties in the IRH dating arise both from the dating of the ice core and from estimating the reflection range. To obtain ice core dating uncertainties, we computed the confidence limits of the age–depth model at both IRHs, giving an uncertainty of 5 a in the upper and 27 a in the lower traced IRH. The range uncertainty is again attributed to two factors: to the inherent uncertainty associated with the width of radar reflections and to the uncertainty in the firn correction applied to the radar data. The latter was estimated as the given range difference between using the KCC or CG03 firn density data for the density correction, as these two ice cores cover the density variability in our study area. In combination, both factors give a range uncertainty on the order of 1 m (Figure 2.6). Full dating uncertainties for both IRHs were computed by propagating all three contributing errors.

In this way, we assigned an age of $76 \pm 7\,\mathrm{a}$ or the year 1945 CE to the upper IRH, which matches the deepest detectable horizon ($78 \pm 12\,\mathrm{a}$) in the survey by Konrad et al. (2013). The lower traced IRH was dated to an age of $288 \pm 35\,\mathrm{a}$ (i.e., the year 1733 CE). As it represents the deepest continuously traceable IRH in our data, it demonstrates that LO-SAR-processed mobile pRES data can be used to inter-compare ice core chronologies at Colle Gnifetti for larger depth and age ranges than what was possible before. The system can in principle illuminate the englacial structure over the whole ice column. Even below the 288 a horizon, IRHs are visible in parts of our data, which implies that older IRHs are potentially also preserved and might be traceable by further improvements in the acquisition and processing.

In summary, the data collected with the mobile pRES reproduce and expand the results of previous surveys. This can be attributed to a combination of accurate data acquisition and system hardware leading to a high SNR and to the enhancement of signal coherence by the applied LO-SAR processing.

A caveat in interpreting deep IRHs and linking them to ice cores lies in their associated depth uncertainty and in potential interference by the bedrock reflector. At the location of the CG03 ice core, the ice–bed interface appears in our radar data at a range of 72 m (Figure 2.6d), whereas the ice core itself has a length of 80.2 m (Jenk et al., 2009). This mismatch can be attributed to a potentially non-vertical orientation of the borehole and steep gradients in the bedrock topography of Colle Gnifetti, which affect the apparent position of the bedrock reflector in the radar data (Eisen et al., 2003; Bohleber, 2011). Following Moran et al. (2000), three-dimensional array processing and correspondingly dense profile grids are needed in steeply sloping topography to accurately measure the bedrock reflector depth. With only two-dimensional profiling, an accuracy on the order of 10 m is to be expected. Moreover, unlike traditional SAR processing methods, the LO-SAR processing does not provide a range migration but merely aims at improving the SNR of specular reflections in the radargram.

Because of the complex basal topography, it is moreover possible that near-basal IRHs are masked by the 15 dB stronger cross-track bedrock reflections if these IRHs are not similarly recorded from cross-track angles. Expanding our setup with a multichannel cross-track antenna array (Castelletti et al., 2017; Holschuh et al., 2020; Scanlan et al., 2020) would allow us to decipher the true origin of the near-basal IRH and bed returns and help in locating, separating and interpreting their signatures.

2.4.3 ORIGIN OF REDUCED RADAR BACKSCATTER

By observing deep IRHs that are undisturbed and nearly flat, it can be excluded that their apparent absence in earlier surveys was caused by buckling or folding of reflectors or a complete degradation of dielectric contrasts. Yet, a distinct transition in radio backscatter between the upper and the lower part of the ice column is also present in the LO-SAR-processed pRES data. The pRES power profile at CG03 (Figure 2.6d) shows a highly reflective regime in the top 36 m, where reflections mostly attain values above -25 dB and a low-reflective regime below 45 m depth, where the returned power rarely exceeds -40 dB. In between these two regimes, the power level drops abruptly over less than 10 m. The bedrock reflections have a normalized power above -25 dB. Variations in density and acidity, together with COF, are reflection mechanisms that can form IRHs and control the reflectivity. Here, we investigate if the dominant reflection mechanisms at Colle Gnifetti and the origin of the drop in backscattered power can be identified by direct comparison of the reflected power of observable IRHs with density and acidity records from ice cores.

At both CG03 and KCC, firn compaction is mostly confined to the upper $\sim$40 m (Figure 2.6a). Strong density variations occur particularly in the top 15 m, where melt layers can be identified in the high-resolution record of the KCC core (Freitag et al., 2018). These variations are likely causing near-surface IRHs. Further down, especially below 35 m depth, density contrasts are significantly weaker and show no correlation with the backscattered power. The reflectivity at depth is therefore not controlled by density.

Accordingly, deep IRHs must be caused by impurities which determine the acidity and perhaps may induce localized gradients in the COF (Drews et al., 2012). By computing the ion balance between the Ca^{2+}, Na^{+}, NH_4^{+}, NO_3^{-} and SO_4^{2-} concentrations measured in the CG03 and CG15 ice cores (Sigl et al., 2018a, 2018b), we obtained an estimate of the acidity with $\sim$3 cm resolution (Figure 2.6b). In addition, for comparison with the pRES signal we smoothed this estimate using a Gaussian filter with a width of 48 cm which corresponds to the mean resolution of the pRES data in firn.

The ion balance is dominated by alkaline peaks that are induced by Ca^{2+} which is a proxy for Saharan dust. An example for a major Saharan dust deposition event is the 1936 CE peak at 36.5 m depth (Sigl et al., 2018a) that appears as a strong IRH in the radar data (Figure 2.6d) and marks the onset of the power drop. Major Saharan dust deposition events occur on decadal timescales, with an increasing frequency only in the last 4 decades attributed to increasing drought conditions in northern Africa (Sigl et al., 2018a). In combination with other natural deposition, for example due to volcanic activity

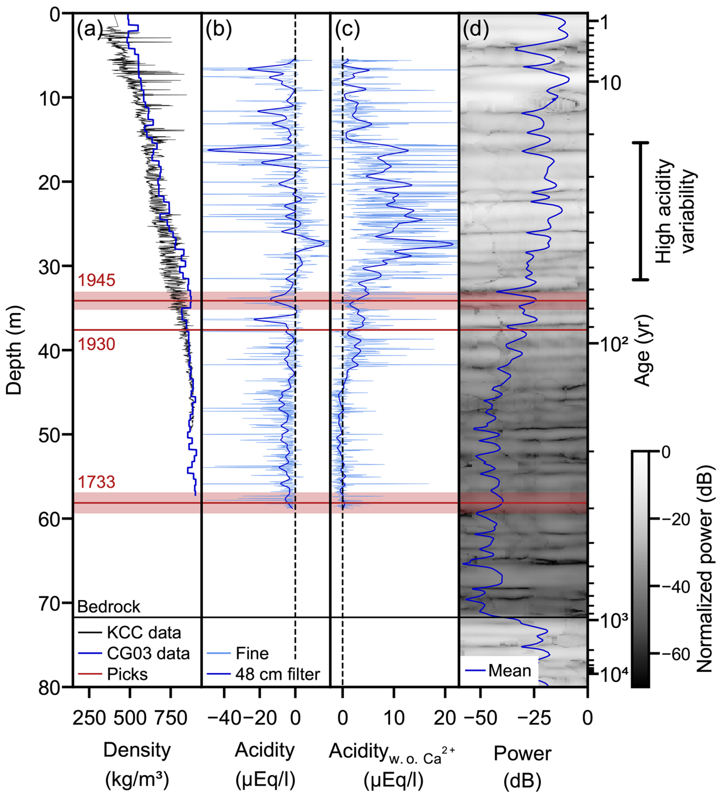

Figure 2.6: Comparison of mobile pRES power with data from the CG03 and CG15 (Sigl et al., 2018b) and KCC (Freitag et al., 2018) ice cores. **(a)** Firn density. **(b)** Acidity estimated by ion balance in fine resolution (2 cm) and after applying a 48 cm Gaussian filter. Panel **(c)** as **(b)** after excluding Ca^{2+} from the ion balance. **(d)** Radar section (2 m) around CG03 and its mean power. Red lines mark traced IRHs, with error bands of the 1945 and 1733 horizons illustrating the uncertainty in the range estimate. Ages are computed using the age–depth model of Jenk et al. (2009).

and forest fires, this sets the natural background for acidity variations at Colle Gnifetti.

By excluding Ca^{2+} from the ion balance, a trend from alkaline conditions in the pre-industrial to more acidic conditions during the 20th century becomes apparent (Figure 2.6c). This trend initiates at a depth of 45 m, which corresponds to the year 1875 CE and the onset of industrialization in western Europe (Sigl et al., 2018a). Accordingly, the transition in acidity can be attributed to an increase in anthropogenic pollution. In particular, the deposition of NH_4^+, NO_3^- and SO_4^{2-} is largely controlled by anthropogenic activity (Preunkert et al., 2003; Schwikowski et al., 1999) and correlates with other industrial emissions (e.g., refractory black carbon; Sigl et al., 2018a). Eisen et al. (2003) suggested that this acidity shift induces the change in reflectivity at Colle Gnifetti. A similar contrast in reflectivity at the glacial–interglacial transition is present across the Greenland Ice Sheet and is also thought to be induced by a transition in the amount of impurity deposition (Karlsson et al., 2013).

The more acidic conditions in the upper ice column are accompanied by a generally higher variability in the acidity, which is most pronounced in the fine resolution record between 15–32 m depth. This high acidity variability strongly correlates with the strength of backscattered power. We conclude that it is not the general acidity level itself which induces the shift from a low- to a high-reflective regime at Colle Gnifetti but that it is caused by the associated higher rate at which deposition of anthropogenic pollution occurs.

In addition to altering the acidity, impurity layers might control the grain size (Kerch, 2016) and thereby induce localized changes in the COF (Drews et al., 2012). Potentially, this mechanism can additionally modulate the reflectivity at Colle Gnifetti. In a seismic profile collected across the KCI ice core, Diez et al. (2013) detected an englacial reflection 5 m above the bedrock, which they attributed to changes in the crystal orientation. In our data, this reflection might correspond to the comparatively strong IRH at 67 m depth.

2.5 DISCUSSION

2.5.1 FEASIBILITY ASSESSMENT

Our proof-of-concept study demonstrates the capability of the pRES to expand the range over which englacial stratigraphy can be detected, which is a clear improvement over previous surveys that used impulse GPRs. However, it comes at the cost of significantly slower data acquisition (Section 2.2.1) that takes several hours as opposed to several tens of minutes with impulse systems. This results from the required high spatial sampling rate and the long chirp time of 1 s of the pRES (which is not a limiting factor for its intended stationary surveys). In combination, these factors make data collection in stop-and-go mode necessary.

This raises the question of whether impulse GPRs can achieve similar detection ranges when being operated in stop-and-go mode and by applying high stacking rates, equivalent to the 1 s chirp time, to suppress incoherent backscatter. Although we cannot answer this question directly, we note that even if these GPRs can achieve an SNR comparable to the unprocessed pRES data (Figure 2.5c), they will not be able to match the SNR potentially achievable by phase-coherent radar processing (Figure 2.5d). We suggest that future research should not focus on improving imaging with impulse GPRs by making data acquisition more painstaking but rather aim at accelerating the profiling capabilities of FMCW radars. The laborious data acquisition is the key limitation for mobile operation of the pRES and restricts the current applicability of the system to targeted small-scale surveys. In the following, we discuss how to accelerate data acquisition in future deployments.

The required spatial sampling rate for LO-SAR processing is set by the fact that reflections need to be traceable (Schroeder et al., 2019). The slope of IRHs can only be derived from the phase when it changes by less than π between neighboring traces; otherwise, spatial aliasing occurs. Thus, following Equation 2.7 the minimal required trace spacing to resolve IRHs with a slope s is given by

$$\Delta d < \frac{\lambda_{\mathrm{c}}}{4\tan(s)}. \tag{2.13}$$

In snow- and firn-covered glacial ice, GPRs can only record IRHs with a maximum slope of approximately 45° (Holschuh et al., 2014). Accordingly, a trace spacing of less than 14 cm is required to record IRHs of such slopes. This also suffices for the threshold of $\Delta d < \lambda_{\mathrm{c}}/2$ to avoid the occurrence of grating lobes when imaging (basal) point reflectors (Kapai et al., 2022). A coarser trace spacing can be used, when only IRHs with a lower inclination are expected at the study site.

Nevertheless, if the requirement for stop-and-go measurements can be relaxed, a high spatial sampling rate is less of a problem. This can be achieved either by reducing the chirp time or by reducing the potential noise due to movement of the pRES during chirp acquisition. Electrical noise by cable motion can be reduced by using phase-stable cables (Hati et al., 2009). However, increased noise by averaging signals of multiple reflections and the occurrence of Doppler blurring and grating lobes (Kapai et al., 2022) can only be avoided with the pRES when moving at very low speeds. Fortunately, these problems are not of a physical but of a technical nature and can again be avoided by reducing the chirp time as discussed in the following.

2.5.2 SYSTEM IMPROVEMENTS

The chirp time T of an FMCW radar is set by its hardware design and operation range. This is because the deramped frequency at a given range is determined by T (Equation 2.1). Thus, the sampling rate of an FMCW radar system's data logger sets a lower limit on T. The pRES, for example, was designed to monitor polar ice up to $2\,\mathrm{km}$ thick, which for a chirp time of $1\,\mathrm{s}$ gives a maximum deramped frequency of $4.7\,\mathrm{kHz}$. The built-in data logger with an effective sampling rate of $40\,\mathrm{kHz}$ was selected accordingly (Brennan et al., 2014). For deploying the pRES on thinner ice, the chirp time can be reduced. For example, for surveying ice less than $200\,\mathrm{m}$ thick, as we do in this study, a $90\,\%$ shorter chirp time could safely be set without exceeding the sampling rate of the data logger. Yet, this reduction would also result in an increased noise level which might need to be compensated for by stacking. To completely avoid the stop-and-go requirement, a redesigned FMCW system is desirable that is similar to many airborne systems whose chirps are much shorter ($\leq 10\,\mu\mathrm{s}$).

A second limitation of the pRES lies in its range resolution, which is 2.5 times coarser compared to the previously used $250\,\mathrm{MHz}$ impulse GPRs. Following Equation 2.2, the vertical resolution of FMCW radars is determined by their bandwidth: $\delta_{R,\mathrm{FMCW}} = c/\big(2\sqrt{\varepsilon_\mathrm{r}}B_\mathrm{FMCW}\big)$. For the pRES with $B = 200\,\mathrm{MHz}$ this results in a vertical resolution of $0.42\,\mathrm{m}$. The resolution of GPRs is often approximated by $\delta_{R,\mathrm{GPR}} = \lambda_\mathrm{GPR}/4 = c/\big(4\sqrt{\varepsilon_\mathrm{r}}f_\mathrm{GPR}\big)$, giving a value of $0.17\,\mathrm{m}$ for $250\,\mathrm{MHz}$ impulse GPRs. These radars are consequently better at detecting shallower IRHs. To achieve a comparable resolution with a redesigned FMCW system, a bandwidth of $500\,\mathrm{MHz}$ would be required.

Besides these potential improvements in the FMCW radar design, certain modifications to our mobile pRES setup should be considered. Here, we used an HH antenna orientation in which the E-plane matches the imaging plane. In this configuration, the radiation pattern of the skeleton slot antennas extends further along the track than across the track, and ground targets are illuminated over more traces; however, the direct wave between the antennas is also stronger, which can promote signal clipping (Vaňková et al., 2020b). To suppress the direct wave, a perpendicular orientation of the E-plane to the profiling direction (VV orientation) might be advantageous. Note that these characteristics are antenna-specific and do not generally apply. In addition, to follow the low-cost approach of the pRES, we suggest to combine it with low-cost GNSS, receivers that can achieve a positioning accuracy that is comparable to commercial instrumentation (Still et al., 2023; Pickell & Hawley, 2024).

2.5.3 SLOPE ESTIMATION

The presented LO-SAR processing is also computationally expensive, primarily because of the slope estimation algorithm. For short profiles, this is less of a problem (in the examples provided here the computation time was $12\,\mathrm{h}$ on a normal-performing desktop computer), but it might be a restriction for more extensive mobile pRES surveys.

Direct computation of englacial slopes from horizontal gradients of the phase, as introduced by MacGregor et al. (2015), is significantly faster. But it also gives a less accurate estimate because it operates on a point-by-point (i.e., zero-dimensional) basis and directly translates noise in the phase into noise in the slopes. For this reason, we derive the slopes of IRHs by matching slope lines to the corrected phase. As this is a one-dimensional approach we combine information from adjacent traces, which entails some horizontal averaging and thereby provides a more accurate slope estimate.

A third method to derive englacial slopes is based on the Radon transform which operates in a two-dimensional window and computes line integrals over a range of possible slopes and intercepts (Holschuh et al., 2017). Similar to our approach, the Radon transform is computed for every grid point, and the correct slope is selected as the one which gives the most coherent stack. Although this is even more computationally expensive, it does not improve the slope estimate further compared to our approach. This can be attributed to the fact that we essentially perform a one-dimensional Radon transform which only considers an intercept of zero. This is possible because we obtain the coherence along the line integrals from the coherence of the phase and not from the coherence of structural patterns, as the two-dimensional Radon transform does.

The computational costs of our slope estimation directly correlate with the length of the slope iteration range. The selection of the iteration range is based on two factors. Its boundaries must cover the range of slopes that are to be expected, and the step size needs to be sufficiently small to ensure that a mismatch does not result in destructive interference along the slope line. The limit for the occurrence of destructive interference can be estimated from the phase offset between range bins of $3\pi/p$ (Equation 2.4). At a phase mismatch of π between the end points of the slope line, these will be completely out of phase, which for $p = 8$ equates to a mismatch of $8/3$ range bins. For an aperture length of $5\,\mathrm{m}$ this corresponds to a slope error of $\sim 2°$. As the computation time was not a limiting factor in our proof of concept, we chose a wide slope range of $-30°$ to $30°$ in steps of $0.2°$ to not a priori prevent the detection of potentially more strongly inclined reflections in the near-basal ice and to sufficiently avoid the destructive interference limit of 2°.

Our final slope estimate shows some noticeable vertical bands (Figure 2.5b). These are most likely not englacial signals but are caused by antenna tilt due to small-scale surface undulations. However, the slopes are only an intermediate product in our LO-SAR processing routine. In the subsequent coherent summation along IRHs, we specifically aim to follow IRHs, also across such undulations. For this reason, these artifacts are of no concern in our study but might be relevant in other applications of the slope estimate.

Finally, it should be noted that our use of the corrected phase during slope estimation contradicts its intended purpose of providing a fine range offset for each range bin, as suggested by Brennan et al. (2014). They introduced it as the phase difference between the raw and the reference phase, which following Equation 2.6 would translate into a fine range offset to measure the absolute range of a reflection in a Vernier-like process (Brennan et al., 2014). However, this approach relies on the assumption that the raw-phase values in each range bin are independent. This would be expressed by a clear inter-bin variability in the raw phase, which cannot be observed (Figure 2.3a). Instead, strong reflections spread out over several range bins, across which the raw phase tends to be stable and distinct jumps of the raw phase only occur at the transition between different reflections. Therefore, the phase of a reflection is only representative of a specific point within its width, potentially its center, which needs to be taken into account for measuring the absolute range of a reflection. The interferometric measurement of the relative change in a reflection range between two measurements is not affected by its inter-bin spread and can be directly computed from phase changes at any range bin.

2.5.4 FUTURE APPLICATIONS

The pRES is used in a broad range of glaciological applications. For example, by performing repeat visits at fixed locations, the pRES can measure ocean-induced melting at the base of ice shelves (Nicholls et al., 2015; Vaňková et al., 2021; Zeising et al., 2022), englacial vertical ice deformation (Gillet-Chaulet et al., 2011; Kingslake et al., 2014) and firn compaction (Case & Kingslake, 2022). With polarimetric techniques that screen the ice with differently polarized electromagnetic waves, the COF can be inferred (Jordan et al., 2020b; Ershadi et al., 2022). Our mobile pRES setup expands this list by the enhanced detection of englacial stratigraphy, but it also offers the potential to perform the above-mentioned survey types with larger spatial coverage.

Polarimetric pRES measurements can efficiently be conducted with multiple-input–multiple-output (MIMO) antenna configurations in which the two transmitting and two receiving polarized radar antennas are orthogonally oriented, respectively. A mobile acquisition of COF data by towing a polarimetric MIMO setup with an autonomous rover was presented by Ershadi et al. (2024). MIMO setups can moreover be used for cross-track signal detection (Castelletti et al., 2017; Holschuh et al., 2020; Scanlan et al., 2020) or for density inversions (Arthern et al., 2013). However, the additional antenna weight restricts the extension of the here-presented mobile pRES setup to MIMO configurations because depending on the surface topography and snow conditions the system would become to heavy for hand-towed operation. For obtaining a lightweight FMCW MIMO system, the use of an FMCW radar that operates in a higher-frequency range and, thus, with smaller and lighter antennas would be required.

For repeat-track surveys, for example to measure the spatiotemporal variability in firn compaction (Medley et al., 2015), no adaptations to our mobile pRES setup are needed. But the correlation of pRES repeat measurements to detect the vertical displacement of englacial reflections or the ice–ocean interface is thought to rely strongly on accurate repositioning of the system. We therefore suggest that future studies investigate which accuracy in the spatial and directional repositioning is required to develop corresponding acquisition and processing techniques.

2.6 CONCLUSIONS

We present a phase-coherent ground-based radar system with low weight and power requirements by mobilizing the pRES. The setup facilitates coherent radar profiling in glaciated areas with low accessibility, as for example on remote mountain glaciers. A centimeter-scale positioning accuracy at decimeter trace spacing is achieved by the integration of an RTK GNSS. In combination, the coherence and positional accuracy enable the application of SAR processing techniques for enhancing the quality of the obtained radargrams. Here, we specifically focus on improving the imaging of the englacial stratigraphy by tailoring the LO-SAR processing technique by Castelletti et al. (2019) to mobile pRES data. In this process, we demonstrate that after the subtraction of the reference phase the corrected phase signal is constant along IRHs. We exploit this characteristic in our implementation of LO-SAR processing by first detecting the slopes of IRHs to filter these before performing the coherent integration of power directly along IRHs.

The capability of the mobile pRES system and LO-SAR implementation is demonstrated in a proof-of-concept study for detecting the deep englacial stratigraphy of Colle Gnifetti. Previous GPR surveys at the site could detect IRHs only in the upper 30–50 % of the ice column, whereas with our approach the presence of a layered stratigraphy can essentially be detected down to the bedrock. Thereby, an IRH with an age of $288 \pm 35\,\mathrm{a}$ could be traced continuously, which is a clear step forward compared to the detection of a $78 \pm 12\,\mathrm{a}$ old IRH achieved by previous surveys. Through a comparison with ice core data, we in addition identified that the presence of a highly reflective regime in the upper part of Colle Gnifetti (detectable in previous surveys) compared to a less-reflective regime in the lower part (which previously appeared echo-free) is caused by acidic impurity layers that have been deposited at a high rate since the onset of industrialization. These improved imaging capabilities of the mobile pRES highlight the possibility to extensively map the deep stratigraphy of Colle Gnifetti and other mountain glaciers in the future. However, our study also demonstrates that the main limitation of the mobile pRES lies in the time intensity of data acquisition due to its 1 s chirp time. We therefore encourage the development of faster ground-based FMCW radar systems suitable for profiling. Repeat-track surveys are a promising application for the mobile pRES as they require no hardware adaptations. In addition to ongoing efforts of expanding the repeat-track capabilities of airborne chirp systems, this opens the avenue to detect englacial deformation, firn compaction and basal melt rates with the pRES with large spatial coverage and fine resolution.

CODE AND DATA AVAILABILITY. The raw and processed mobile pRES data are available at https://doi.org/10.1594/PANGAEA.965199 (Oraschewski et al., 2024b) and https://doi.org/10.1594/PANGAEA.965194 (Oraschewski et al., 2024a). The LO-SAR processing code is available at https://doi.org/10.5281/zenodo.12656458 (Oraschewski, 2024a).

SUPPLEMENTARY. The supplement (Section A) related to this article is available online at: https://doi.org/10.5194/tc-18-1-2024-supplement.

COMPETING INTERESTS. At least one of the (co-)authors is a member of the editorial board of *The Cryosphere*. The peer-review process was guided by

an independent editor, and the authors also have no other competing interests to declare.

ACKNOWLEDGEMENTS. We thank Timm-Emanuel Riesen from the Center for Space and Habitability (CSH), University of Bern, for granting us access to Stellarium Gornergrat for acclimatization. We further thank the editor and the two reviewers for their constructive comments that improved the paper.

FINANCIAL SUPPORT. This research has been supported by the Studienstiftung des Deutschen Volkes (doctoral scholarship awarded to Falk M. Oraschewski), the Deutsche Forschungsgemeinschaft (grant no. DR 822/3-1) and the Royal Society (grant no. RGF\EA\180173, awarded to Lai Bun Lok).
This open-access publication was funded by the Open Access Publication Fund of the University of Tübingen.

REVIEW STATEMENT This paper was edited by Joseph MacGregor and reviewed by Benjamin Hills and one anonymous referee.

3

POLARIMETRIC WIDE-ANGLE RADAR DETECTS COMPETING SIGNATURES OF ICE FABRIC AND STRUCTURAL FIRN ANISOTROPY

PUBLICATION DETAILS

This chapter has been published in *Geophysical Research Letters*:

Oraschewski, F. M., Ershadi, M. R., & Drews, R. (2025c). Polarimetric wide-angle radar detects competing signatures of ice fabric and structural firn anisotropy. *Geophysical Research Letters*, *52*(14), e2024GL113096. https://doi.org/10.1029/2024GL113096

AUTHOR CONTRIBUTIONS

FMO led the data acquisition, analysis and writing of the paper. MRE was involved in the data acquisition and performed the ice fabric nadir-inversion. RD acquired the funding for the field campaign and contributed to the writing of the paper.

Falk M. Oraschewski[1], M. Reza Ershadi[1], Reinhard Drews[1]

[1]Department of Geosciences, University of Tübingen, Tübingen, Germany

KEY POINTS

- Phase-sensitive polarimetric wide-angle radar surveys detect horizontal and vertical ice fabric and structural firn anisotropy
- Structural firn anisotropy dominates vertical dielectric anisotropy signatures and must be determined before inverting for ice fabric
- These observations highlight the investigation of firn anisotropy as a new application for ground-based radar polarimetry

ABSTRACT

Ice is mechanically and dielectrically anisotropic. The degree of anisotropy evolves dynamically as ice crystals align during deformation into macroscopic patterns termed ice fabric. Radar polarimetry is an emerging tool to detect such patterns, particularly using nadir-looking antenna geometries sensitive to horizontal anisotropy. Although theoretical studies discussed oblique incidence of radio waves to detect vertical anisotropy and relax the assumption of vertical fabric alignment, so far no data were available to test this. Here, we analyze a polarimetric common midpoint survey from Ekström Ice Shelf and develop a framework to invert all relevant ice fabric components. We find that our data not only detect the expected deep ice fabric, but are also significantly impacted by structural anisotropy of near-surface firn. This has been neglected in previous studies and introduces tradeoffs between both effects in the inversion. It also opens up new possibilities for investigating firn with radar polarimetry.

PLAIN LANGUAGE SUMMARY

In glaciers and ice sheets, the orientations of individual ice crystals can align during deformation and make the ice flow direction-dependent. Radar can detect these crystal orientation patterns by observing changes in the radio wave speed between different antenna orientations. Previous studies use radar configurations in which the radio waves are propagating vertically. In this study, we present a radar survey with wide antenna spacings that provide oblique wave propagation directions and are more sensitive to vertically oriented ice crystal patterns, which are important for better understanding the ice dynamics of fast flowing ice. We find that our observations not only detect the crystal orientations, but are strongly influenced by structural patterns in the near-surface firn. Firn describes accumulated snow that is in the process of compacting to ice and is composed of ice grains and air pores. These can be vertically elongated and thereby cause radar signatures that can obscure the signatures by the crystal orientations. By demonstrating that these structures can be observed with radar, which has not been considered in previous studies, our observations open up new possibilities for studying these structures.

3.1 INTRODUCTION

Glacial ice is a viscous fluid and the ice rheology (i.e., the relationship between stress and strain rate) depends among other factors on the bulk orientation of individual ice crystals. These orientation patterns, termed ice fabrics, evolve with ice flow (Richards et al., 2021; Llorens et al., 2022; Lilien et al., 2023) and develop a mechanical anisotropy (Duval et al., 1983; Rathmann et al., 2021) contributing to primary ice dynamic processes such as the evolution of ice streams (Minchew et al., 2018; Gerber et al., 2023) or macro-scale folding at depth (Bons et al., 2016). Constraining mechanical anisotropy parametrizations for inclusion into ice flow models requires geophysical observations of ice fabric away from ice cores (Graham et al., 2018).

Radar polarimetry is an emerging tool to map ice fabrics as the mechanical anisotropy is accompanied by dielectric anisotropy, making ice a birefringent medium (Hargreaves, 1978). Techniques to invert ice fabric from polarimetric radar observations have significantly advanced over the past decade (Dall, 2010; Brisbourne et al., 2019; Jordan et al., 2019; Young et al., 2021a; Ershadi et al., 2022; Zeising et al., 2023). All of these studies use some metric of traveltime or phase delay between different polarization directions to infer ice fabric with depth and show promising agreement with ice core data. Polarimetric techniques are starting to get widely applied for investigating present and past ice dynamics on regional scales (Jordan et al., 2022; Ershadi et al., 2025; Hills et al., 2025a). This development will be further accelerated by the emerging feasibility of continuous ice fabric profiling (Ershadi et al., 2024; Gerber et al., 2025). However, previous observations were restricted to vertical radio wave propagation, which underconstrains ice fabric orientation and is only indirectly sensitive to vertical anisotropy via reflection-power ratios (Ershadi et al., 2022). Consequently, the limited constraint on vertical ice fabric anisotropy leads to significant uncertainties in inverting anisotropic ice viscosity (Jordan et al., 2022). Wide-angle radar surveys have been proposed as an alternative approach for inferring vertical ice fabric anisotropy (Rathmann et al., 2022). However, oiblique propagation of polarized radio waves has only been considered in theory (K. Matsuoka et al., 2009; Rathmann et al., 2022) and for the specific application of neutrino detection at the South Pole (Jordan et al., 2022). The inversion of unknown ice fabrics through targeted polarimetric wide-angle experiments has not been addressed.

In firn, the transition stage from snow to glacial ice, ice grains and pore spaces exhibit a predominantly vertical elongation (Lytle & Jezek, 1994; Pfeffer & Mrugala, 2002; Fujita et al., 2009). This structural firn anisotropy (hereafter termed firn anisotropy) represents an additional source of dielectric anisotropy (Sihvola & Kong, 1988) that can be more than twice as strong as the maximum dielectric anisotropy due to ice fabric (Lytle & Jezek, 1994). Firn anisotropy forms in the uppermost 3 m (Hörhold et al., 2009; Lomonaco et al., 2011; Inoue et al., 2024) by insolation-driven temperature gradient metamorphism (hence, its vertical elongation, Hutterli et al., 2009; Fujita et al., 2009), where the strength of firn anisotropy correlates with the initial density of the firn, determined by the local wind conditions, and its residence time in the near-surface, controlled by the accumulation rate (Hörhold et al., 2009; Inoue et al., 2024). In combination, these factors favor a high spatiotemporal variability of firn anisotropy (Fujita et al., 2016). While firn anisotropy decreases with depth, it influences the microstructure and permeability of firn until pore close-off, thereby potentially affecting important properties for analyzing ice core records such as the age difference between ice and enclosed air bubbles (Keegan et al., 2019), the total air content and gas fractionations (Fujita et al., 2014). Previous polarimetry studies neglected the effect of firn anisotropy, most likely due to their lack of sensitivity to vertical dielectric anisotropy.

Here, we present results of a phase-sensitive, polarimetric common midpoint survey (CMP, Figure 3.1a) and develop a forward-modeling framework able to capture ice fabrics of variable strength and orientation (Figure 3.1b) together with a parametrization for dielectrically anisotropic firn. The latter dominates the signal response at oblique incidence in our data. Although this limits the ice fabric anisotropy inversion, we demonstrate that disentangling both effects is possible.

3.2 FORWARD MODEL FOR WAVE PROPAGATION IN POLARIMETRIC CMPS

In a CMP, the distance d between transmitter (Tx) and receiver (Rx) is increased around a common midpoint at consistent increments (Figure 3.1a). This geometry illuminates horizontal interfaces in the subsurface at the same reflection point but with variable incidence angles θ, providing information about changes in the radio-wave velocity with depth (Eisen et al., 2002). By rotating the antennas at each incremental offset, the polarization-dependency of the wave velocity can be inferred. We consider measurements with three antenna orientations: HH, HV, VV, indicating parallel (H) and perpendicular (V) polarization of Tx and Rx relative to the CMP profile direction. In the following, we develop a model for traveltime differences between the co-polarized measurements HH and VV.

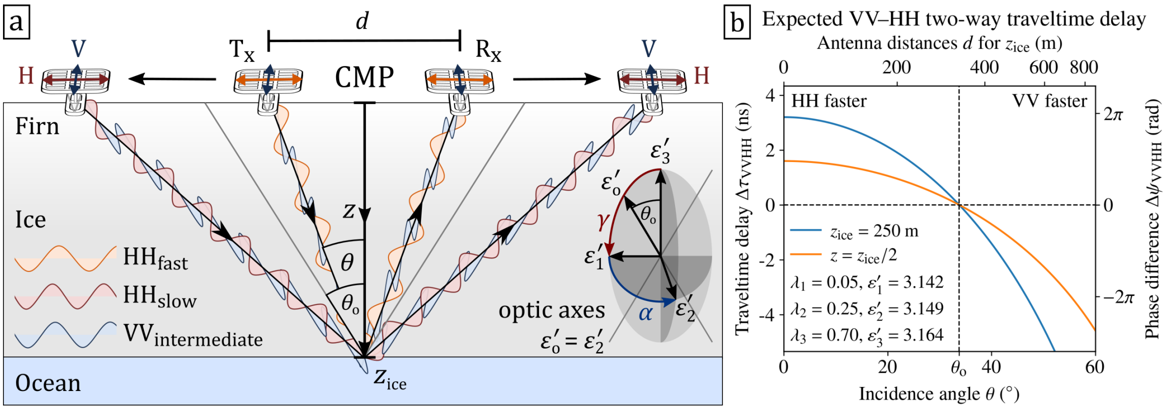

Figure 3.1: (a) Schematic of common midpoint radar configuration for wave propagation in the optic plane. The propagation velocity of radio waves with plane-parallel polarization (HH) is incidence angle-dependent, whereas it is independent for perpendicular-polarized VV waves. Along the optic axes (gray lines, $\theta = \theta_o$), the propagation velocity is independent of polarization. The displayed HH-oriented antennas are turned by 90° for VV measurements. Ray path curvature due to density gradients in firn is taken into account but not shown here. (b) Forward-modeled (VV–HH) two-way traveltime and phase difference.

3.2.1 POLARIZATION-DEPENDENT TRAVELTIME DELAYS DUE TO ICE FABRIC

The propagation velocity of electromagnetic waves is determined by the real part of the dielectric permittivity (Fujita et al., 2006). Single ice crystals are dielectrically uniaxial with permittivities of $\varepsilon'_{\parallel} = 3.17$ and $\varepsilon'_{\perp} = 3.14$ parallel and perpendicular to their c-axis, respectively (Fujita et al., 2000; Bohleber et al., 2012), and a dielectric anisotropy of $\Delta\varepsilon' = \left(\varepsilon'_{\parallel} - \varepsilon'_{\perp}\right) = 0.034$ (T. Matsuoka et al., 1997). For polycrystalline ice, the second-order dielectric permittivity tensor

$$\boldsymbol{\varepsilon}' = \begin{pmatrix} \varepsilon'_1 & 0 & 0 \\ 0 & \varepsilon'_2 & 0 \\ 0 & 0 & \varepsilon'_3 \end{pmatrix} = \begin{pmatrix} \varepsilon'_{\perp} + \lambda_1\Delta\varepsilon' & 0 & 0 \\ 0 & \varepsilon'_{\perp} + \lambda_2\Delta\varepsilon' & 0 \\ 0 & 0 & \varepsilon'_{\perp} + \lambda_3\Delta\varepsilon' \end{pmatrix}, \quad (3.1)$$

that defines an ellipsoid (Figure 3.1a), locally describes the biaxial birefringence caused by ice fabric (Hargreaves, 1978). $\boldsymbol{\varepsilon}'$ depends linearly on the second-order ice fabric tensor, where $\lambda_1 \leq \lambda_2 \leq \lambda_3$ are the normalized eigenvalues ($\lambda_1 + \lambda_2 + \lambda_3 = 1$) that describe the distribution of the c-axes orientations along the associated eigenvectors $\boldsymbol{v}_1$, $\boldsymbol{v}_2$ and $\boldsymbol{v}_3$. Radar is not sensitive to higher-order moments of the ice fabric. For isotropic ice, the c-axes are equally distributed ($\lambda_1 \approx \lambda_2 \approx \lambda_3 \approx 1/3$). Characteristic ice-dynamically induced fabric types include single-maximum fabrics ($\lambda_1 \approx \lambda_2 \ll \lambda_3$) and vertical-girdle fabrics ($\lambda_1 \ll \lambda_2 \approx \lambda_3$). $\boldsymbol{\varepsilon}'$ can vary with depth z both in strength (represented by differences in the eigenvalues) and orientation (represented by colatitude γ and azimuth α, inset Figure 3.1a).

For wave propagation along an arbitrary direction, a plane oriented perpendicular to the ray path and cutting the ellipsoid center defines an ellipse. The two principal axes of this ellipse mark the two possible polarizations, meaning that an incident radio wave that is polarized parallel to one of these principal axes maintains its polarization. Otherwise, it is depolarized and split into two waves with polarizations parallel to the principal components. The propagation velocities are then determined by the principal radii of the permittivity ellipse (cf. the closely related concepts of ordinary and extraordinary waves in uniaxial crystals).

Following the model setup of Jordan et al. (2020a), we assume a depth-variable, layered ice fabric that at all depths is vertically oriented ($\gamma = 0°$) and has a $\boldsymbol{v}_1\boldsymbol{v}_3$-eigenplane that equals the CMP plane ($\alpha = 0°$), meaning the plane in which radar waves propagate. Each layer has a thicknesses of $\Delta z = 1\,\mathrm{m}$. This setup is appropriate for our observations. Supporting Information B.2 presents an extension of the model for arbitrary ice fabric orientations.

In the forward model, the permittivies for the VV and HH polarizations in the nth layer are:

$$\varepsilon'_{\mathrm{VV},n} = \varepsilon'_{2,n}, \tag{3.2}$$

$$\varepsilon'_{\mathrm{HH},n}(\theta_n) = \frac{\varepsilon'_{1,n}\varepsilon'_{3,n}}{\sqrt{\varepsilon'^2_{1,n}\sin^2(\theta_n) + \varepsilon'^2_{3,n}\cos^2(\theta_n)}}, \tag{3.3}$$

so that only the HH wave is sensitive to vertical anisotropy and dependent on the local incidence angle θ_n. For two incidence angles $\pm\theta_\mathrm{o}$ that are axis-symmetric around $\boldsymbol{v}_3$, the trigonometrically weighted combination of the major and minor eigenvalues matches the intermediate eigenvalue ε'_2. Along these directions, the dielectric permittivity is independent of the wave polarization, defining the two optic axes of the biaxial medium. Hence, the $\boldsymbol{v}_1\boldsymbol{v}_3$-eigenplane is also referred to as the optic plane.

A radar wave that is transmitted at the surface with an incidence angle θ_1 is deflected at permittivity changes along its ray path according to Snell's law:

$$\theta_n = \sin^{-1}\left(\sqrt{\frac{\varepsilon'_{\mathrm{VV},1}}{\varepsilon'_{\mathrm{VV},n}}}\sin(\theta_1)\right). \tag{3.4}$$

The curvature is dominated by the dependency of permittivity on density, which is depth-dependent in the firn (Section 3.2.2). These density-induced permittivity changes are an order of magnitude stronger than potential permittivity variations from dielectric anisotropy. Therefore, the HH and VV waves travel approximately along the same trajectories. As commonly done in ray-tracing schemes, for each depth horizon Z (in integers of meters) and offset d, the incidence angle at the surface $\theta_1(Z, d)$ is determined in the forward model based on the density profile by trial and error.

The expected polarization-dependent traveltime delay due to birefringence is:

$$\Delta\tau_{\mathrm{VVHH}}(Z, d) = \sum_{n=1}^{Z} \frac{2\Delta z}{\cos(\theta_n(Z, d))} \cdot \frac{\sqrt{\varepsilon'_{\mathrm{VV},n}} - \sqrt{\varepsilon'_{\mathrm{HH},n}(\theta_n(Z, d))}}{c}, \tag{3.5}$$

where the first fraction describes the two-way path length in each layer and the second fraction the difference of the reciprocals of the polarization-dependent wave velocities (i.e., the slowness), with the speed of light in vacuum c. Following this model, variations of $\Delta\tau_{\mathrm{VVHH}}$ with Z originate from horizontal anisotropy in the ice, whereas variations with d are a signature of vertical anisotropy (Figure 3.1b). In the data, reflection horizons are observed at sub-grid depth values z and the corresponding modeled traveltime delays $\Delta\tau_{\mathrm{VVHH}}(z, d)$ are obtained by linearly interpolating $\Delta\tau_{\mathrm{VVHH}}(Z, d)$ along Z.

3.2.2 POLARIZATION-DEPENDENT TRAVELTIME DELAYS IN FIRN

In porous firn with density ρ, the dielectric permittivity is reduced as described by the Looyenga (1965) mixture model:

$$\varepsilon'_{\text{eff}} = \left(\nu\varepsilon'^{1/3} + (1-\nu)\right)^3, \tag{3.6}$$

with the ice-air volume fraction $\nu = \rho/\rho_{\text{ice}}$ and density of glacial ice ρ_{ice}. This effect determines the ray path of obliquely propagating radio waves in firn and is inherently included in the forward model by applying Equation 3.6 after Equation 3.1. The corresponding effective permittivities are then inserted in Equations 3.2–3.3.

Critical for polarimetric CMPs is that firn anisotropy due to vertically elongated ice grains and pore spaces can induce vertical dielectric anisotropy $\Delta\varepsilon'_{\text{firn}}$ that can be as large as 0.08 (Lytle & Jezek, 1994; Fujita et al., 2009). This is more than twice the dielectric anisotropy of the most anisotropic ice fabric (i.e., the single maximum ice fabric with $\Delta\varepsilon' = 0.034$). The functional description of depth-variable firn anisotropy is not well established but may follow an exponential or sigmoidal decay (Figure 6 in Fujita et al., 2016). We implement this using a logistic decay function:

$$\Delta\varepsilon'_{\text{firn}}(\rho) = \frac{\Delta\varepsilon'_0}{1 + \exp\left(-(\phi_{\text{norm}}(\rho) - \phi_{\text{mid}})/\phi_{\text{decay}}\right)}, \tag{3.7}$$

formulated in terms of the porosity that is normalized for surface density ρ_{sur}:

$$\phi_{\text{norm}}(\rho) = \frac{\rho_{\text{ice}} - \rho}{\rho_{\text{ice}} - \rho_{\text{sur}}}. \tag{3.8}$$

Depending on the tuning variables ϕ_{mid} and ϕ_{decay}, Equation 3.7 describes an exponential or sigmodial form. The strength of firn anisotropy is modulated by $\Delta\varepsilon'_0$. Firn anisotropy can be included in the forward model by replacing $\varepsilon_{3,\text{eff}}$ with $\varepsilon_{3,\text{eff}} + \Delta\varepsilon'_{\text{firn}}$, as firn anisotropy is assumed to only affect the vertical permittivity component.

3.3 POLARIMETRIC CMP OBSERVATIONS AT EKSTRÖM ICE SHELF

3.3.1 DATA AND STUDY SITE

We have acquired a polarimetric CMP using the phase-sensitive Radio Echo Sounder (pRES), a frequency-modulated continuous-wave radar with a center frequency of $f_c = 300\,\text{MHz}$ and $200\,\text{MHz}$ bandwidth (Brennan et al., 2014). The pRES can measure relative traveltime delays $\Delta\tau_{\text{VVHH}}$ via phase-shifts between VV and HH acquisitions:

$$\Delta\psi_{\text{VVHH}} = 2\pi f_c \Delta\tau_{\text{VVHH}}. \tag{3.9}$$

The study site (70.703127°S, 8.603937°W) is centrally located on Ekström Ice Shelf, Droning Maud Land, Antarctica. The CMP profile is oriented parallel to flow. Transmitter and receiver were connected with four $25\,\text{m}$ coaxial cables, each. Their distance d was increased from $10\,\text{m}$ to $200\,\text{m}$ in $2\,\text{m}$ increments, giving a maximum incidence angle of $20.1°$ at the locally $260\,\text{m}$ deep ice base. Data acquisition took approximately four hours.

We follow standard pRES signal processing (Brennan et al., 2014; Oraschewski et al., 2024c). Power, traveltime and phase along observed reflection hyperbolas are semi-automatically extracted. The phase is ambiguous to integer-multiples of 2π (Arthern et al., 2013), which is resolved by unwrapping the phase and phase differences (Supporting Information B.1.4). Firn densities are obtained by traveltime inversion (Drews et al., 2016) of the VV signal for which the permittivity is independent of the incidence angle.

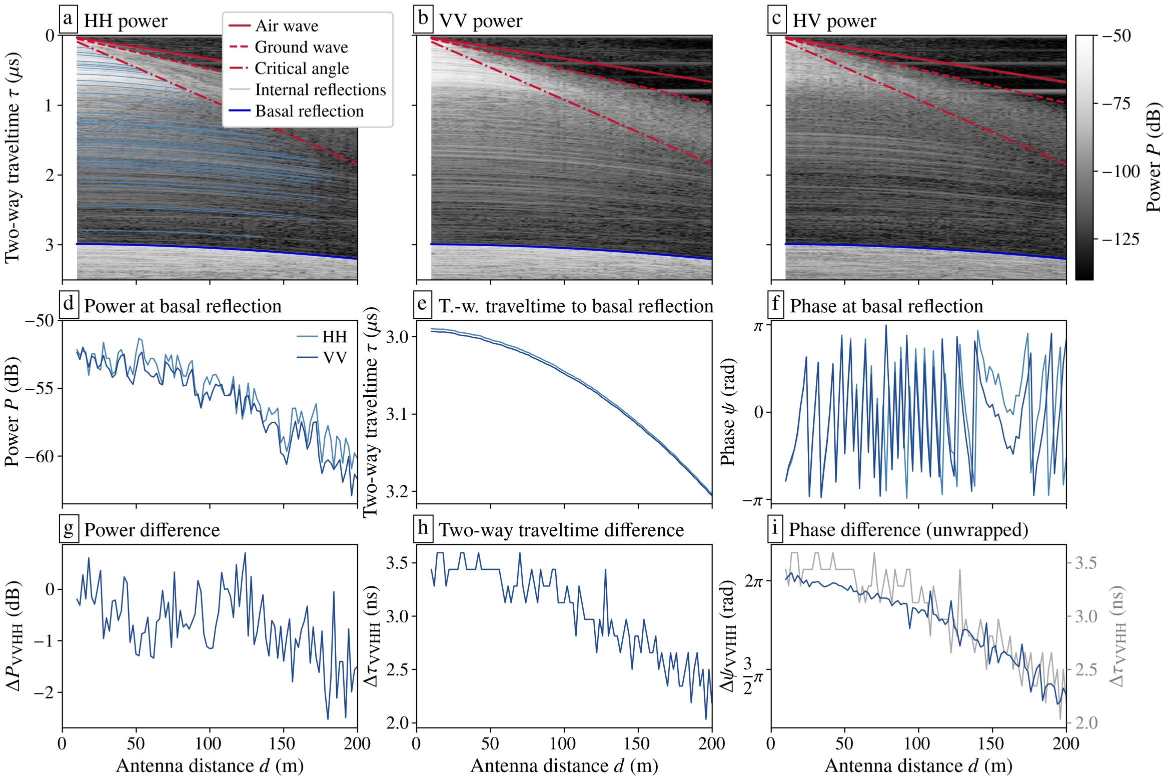

Figure 3.2: Polarimetric CMP data. (a–c) Recorded power for different antenna polarizations with (a) semi-automatically traced internal reflection hyperbolas. (d–f) Total power, two-way traveltime and phase of basal reflection for HH and VV measurements. (g–i) Their differences (VV–HH) show moveout-dependent signatures of vertical anisotropy that are most accurately detected in the phase difference signal.

3.3.2 ANISOTROPY INVERSION

The model-data misfit for the VV–HH phase difference is evaluated at 36 englacial reflection hyperbolas originating from distinct depth intervals. Hence, the forward model is applied in the distance-depth domain. Inversion of $\Delta\psi_{\mathrm{VVHH}}(z,d)$ is executed with four successive approaches.

First, we only consider the nadir-looking data (at $d = 10\,\mathrm{m}$) and replicate the previously developed mono-static inversion (Ershadi et al., 2022). This method is particularly sensitive to the horizontal ice fabric anisotropy $\Delta\lambda_{21} = \lambda_2 - \lambda_1$, but reconstructs all three ice fabric eigenvalues top-to-bottom via changes in the polarization-dependent reflection-power ratio, assuming isotropic ice at the surface.

Second, we consider data from all incidence angles and invert for ice fabric using the oblique incidence forward model (Equations 3.1–3.6), neglecting effects of firn anisotropy. We parameterize eigenvalues to change linearly with depth so that four model parameters are optimized including the eigenvalue differences at the surface ($\Delta\lambda_{21,\mathrm{sur}}$, $\Delta\lambda_{31,\mathrm{sur}}$) and their slopes ($\mathrm{d}\Delta\lambda_{21}/\mathrm{d}z$, $\mathrm{d}\Delta\lambda_{31}/\mathrm{d}z$). The inversion uses a gradient descent scheme with parameter bounds of the eigenvalue differences between 0 and 1 and of the slopes between $\pm 1/z_{\mathrm{ice}}$. The initial guesses are 0 for the former and $0.01/z_{\mathrm{ice}}$ for the latter. During the inversion, eigenvalues are computed by

$$\begin{aligned} \lambda_1(z) &= (1 - \Delta\lambda_{21}(z) - \Delta\lambda_{31}(z))/3, \\ \lambda_2(z) &= \lambda_1(z) + \Delta\lambda_{21}(z), \\ \lambda_3(z) &= \lambda_1(z) + \Delta\lambda_{31}(z), \end{aligned} \tag{3.10}$$

and are individually bound between 0 and 1.

Third, we fix the ice fabric to the nadir results and invert for firn anisotropy (Equations 3.8–3.7). The three inversion parameters are now $\Delta\varepsilon'_0$, ϕ_{mid} and ϕ_{decay}. The former is bound between 0.01 and 0.1 with an initial guess of 0.05 and the later two are bound between 0.05 and 1 with an initial guess of 0.5.

Fourth, we perform a combined inversion for ice fabric and firn anisotropy. The inversion is performed in two steps to avoid tradeoffs between both mechanisms. In step 1, firn anisotropy is assumed to be dominant over the upper 75 m. Reflections within this range are inverted for firn anisotropy for five fixed $\Delta\varepsilon'_0$ values between 0.02 and 0.1 to represent different functional dependencies. Horizontal anisotropy still needs to be taken into account in step 1 and is fixed based on the nadir-results. In step 2, the firn anisotropy obtained in step 1 is fixed and now ice fabric is inverted analogous to the ice-fabric-only inversion.

3.4 RESULTS

3.4.1 POLARIZATION DEPENDENCY IN CMP DATA

The acquired polarimetric CMP data (Figure 3.2) can be analyzed in terms of power, traveltime and phase. We first focus on the co-polarized HH and VV returns of the basal reflection (Figure 3.2d–f). All three radar metrics are mainly determined by the CMP geometry and only the differences between the two polarizations (VV–HH) provide information about dielectric anisotropy. While the HH and VV power are equal (Figure 3.2g) for small antenna distances, their difference increases to 2 dB at larger offsets. This trend can be a signature of vertical dielectric anisotropy (K. Matsuoka et al., 2009), but it is accompanied by a large relative uncertainty. Both, the traveltime differences (Figure 3.2h) and the proportional phase differences $\Delta\psi_{\mathrm{HHVV}}$ (Figure 3.2i) show the expected angular hyperbolic dependency as predicted by our forward model (Figure 3.1b). However, the relative uncertainty of $\Delta\psi_{\mathrm{HHVV}}$ is remarkably low, making it the best quality metric for analyzing the CMP data.

3.4.2 INVERSION OF ICE FABRIC AND FIRN ANISOTROPY

For all internal reflection hyperbolas, phase differences decrease with moveout (Figure 3.3a). This is most pronounced in the shallower reflections, where incidence angles are large for moderate antenna distances. In particular, phase differences change sign at $\theta \approx 30^\circ$, indicating the angle of the optic axes.

Our first (nadir-looking) ice fabric inversion predicts progressive development of a horizontal girdle fabric with depth (Figure 3.3c). The model–data misfit is small for small incidence angles but phase differences for larger

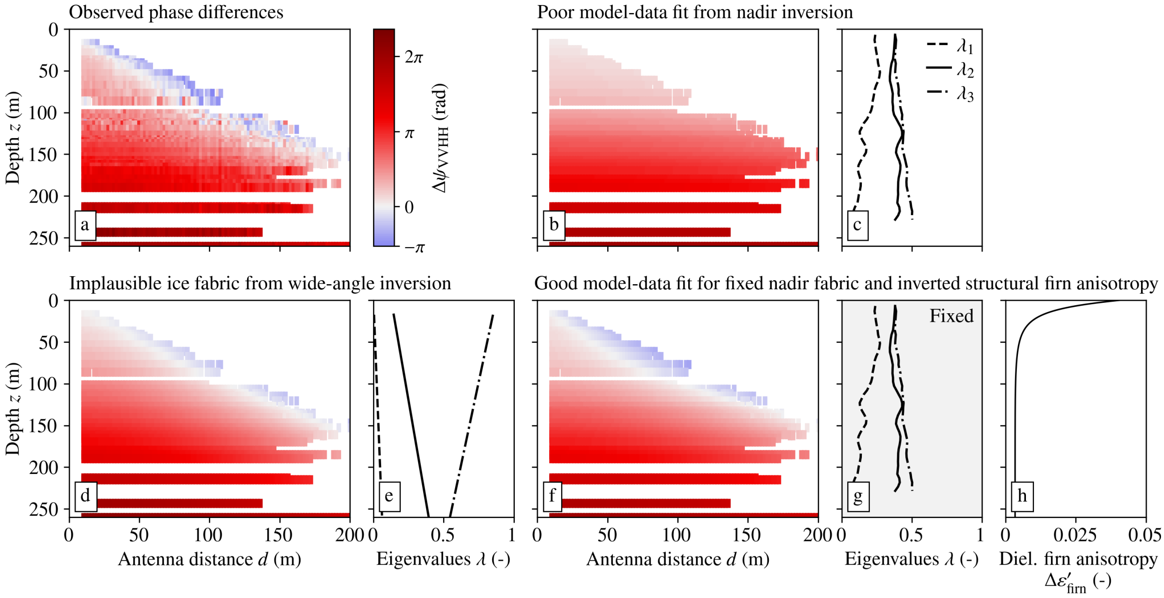

Figure 3.3: (a) Observed VV–HH phase differences from wide-angle CMP. (b, d, f) Forward modeled phase-differences for three inversion experiments. (c, e, g–h) Inversion results. (b–c) The nadir ice fabric inversion captures horizontal anisotropy, but is insensitive to moveout effects from vertical dielectric anisotropy. (d–e) The wide-angle inversion achieves the best-matching forward model but suggests implausible single-maximum fabric at the ice surface. (f–h) Inverting for firn anisotropy while keeping the nadir inversion ice fabric fixed provides a comparable model–data fit.

moveouts are significantly underestimated (Figure 3.3b), demonstrating that the nadir inversion does not capture the vertical dielectric anisotropy correctly. The second (wide-angle) ice fabric inversion predicts a similar horizontal anisotropy as for the nadir case, but provides a much stronger vertical anisotropy with $\lambda_3 = 0.85$ at the surface that is decreasing with depth (Figure 3.3e). The model–data misfit is small for all incidence angles, but, as we will discuss later, the strong ice fabric anisotropy at the surface is unlikely. The third inversion for firn anisotropy (with fixed ice fabric from nadir inversion) provides an equally good model–data fit as the wide-angle ice fabric inversion (Figure 3.3f). Therefore, firn anisotropy can fully describe the observed vertical dielectric anisotropy signatures in the VV–HH phase differences, even for reflections beneath the firn. Lastly, the two-step inversion shows a varying functional form for the depth dependency of vertically anisotropic firn dependent on the fixed $\Delta\varepsilon'_0$ value (Figure 3.4a). Yet, the ice fabric inverted in step 2 is effectively identical for all firn anisotropy parametrizations (Figure 3.4b) and a good model-data fit is achieved (Figure 3.4c).

3.5 DISCUSSION

Our first inversion shows that polarimetric CMPs are sensitive to vertical anisotropy, not resolved by nadir measurements. The second and third inversion provide competing scenarios which can both explain the observations. However, the second (fabric only) inversion predicts a strong single-maximum fabric in the upper 20 m. This is inconsistent with current theory of fabric evolution (Llorens et al., 2022; Lilien et al., 2023), where single-maximum fabrics evolve under vertical compression and typically occur at the ice base.

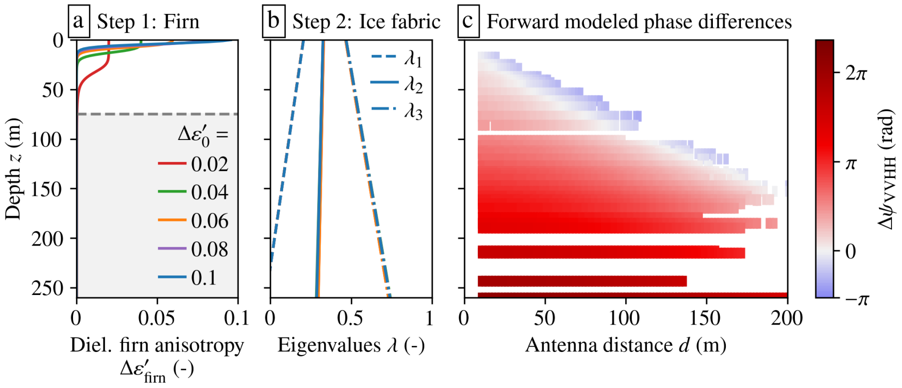

Figure 3.4: Two-step ice fabric and firn anisotropy inversion. (a) Firn anisotropy inverted over upper 75 m for five different $\Delta\varepsilon'_0$ values. (b) Subsequently inverted ice fabric with strong agreement between all firn anisotropy parameterizations (The eigenvalue profiles are overlapping for all $\Delta\varepsilon'_0$ values). (c) Forward modeled phase differences.

In contrast, firn anisotropy is a known cause of vertical dielectric anisotropy (Fujita et al., 2009), although it has been neglected in the context of radar polarimetry, most likely because nadir measurements are insensitive to that effect. We therefore conclude that firn anisotropy is the predominant cause for the observed signatures of vertical dielectric anisotropy.

3.5.1 SHIELDING OF VERTICAL ICE FABRIC ANISOTROPY BY FIRN

As vertical ice fabric anisotropy and firn anisotropy can compensate for each other in polarimetric CMP data, strongly anisotropic firn can obscure signatures of ice fabric. This complicates the ice fabric inversion, particularly because dielectric firn anisotropy can be more than twice as strong as the maximum possible dielectric anisotropy of ice fabric, while imprinting on reflections beneath the firn and having a poorly constrained depth variability. However, the consistency between the combined inversions (Figure 3.4) shows significant tradeoffs between the strength of firn anisotropy and the thickness of the anisotropic firn layer. This indicates that the depth-integrated firn anisotropy is the relevant property imprinting on deeper reflections. Therefore, all ice fabric eigenvalues and presumably vertically tilted ice fabric patterns can still be reconstructed in spite of the dominant contribution from the firn. Future research should validate this by conducting polarimetric CMPs near ice core sites with known and preferably tilted ice fabrics.

3.5.2 CMP-EIGENPLANE ALIGNMENT

During our analysis, we assumed that the CMP is aligned with the optic plane of the underlying ice fabric ($\alpha = 0°$). Since the CMP profile aligns with ice flow, which for the central Ekström Ice Shelf is characterized by pure shear with dominant along-flow stretching, this assumption is reasonable (Richards et al., 2021, 2023). However, antenna and profile directions are only constrained to approximately $\pm 10°$ in the field and at intermediate depths, where HH and VV are in anti-phase ($\Delta\psi_{\mathrm{VVHH}} = \pi$), the HV power shows reflection hyperbolas of comparable strength (Figure 3.2c), suggesting a CMP-eigenplane misalignment of up to $\alpha = 22.5°$ (Figure 5 in Fujita et al., 2006). Fortunately, this does not limit our phase-based analysis, because for small misalignments between radar polarization and an ice fabric eigenplane, the HH and VV signals are each dominated by distinct principal wave components that determine their respective phases (Supporting Information B.2). This explains the low phase difference uncertainty and confirms that phase is the most suitable radar metric for analyzing polarimetric CMPs.

3.5.3 IMPLICATIONS AND NEW AVENUES FOR FIRN STUDIES

The vertical dielectric anisotropy of firn can bias density inversions from non-polarimetric CMPs on the order of a few percent (Supporting Information B.1.3). Therefore, we suggest that radar-based firn density measurements should employ a VV antenna configuration to minimize the impact of firn anisotropy. Yet, our observations also highlight possibilities for spatially measuring firn anisotropy with ground-based radar surveys to investigate its potentially important impact on firn air processes. This may be extended further with satellite remote sensing of firn anisotropy, exploiting the many upcoming quad-polarimetric radar systems with different frequencies. This can provide corrections for the penetration bias in satellite altimetry studies (Dall, 2007), and aid the classification of glacier zones (Parrella et al., 2021) as well as the detection of refrozen melt layers (Fischer et al., 2019). Ground-truth data, in the form of polarimetric wide-angle surveys, can drive this forward and the development of higher frequency phase-sensitive radar systems would be particularly beneficial in this regard.

3.6 CONCLUSION

We analyzed a phase-sensitive polarimetric common midpoint radar survey conducted at Ekström Ice Shelf. We find that polarization-dependent phase differences between the HH and VV orientations are the best metric to interpret traveltime delays caused by birefringence. Our data exhibit strong vertical dielectric anisotropy that can either be caused by the occurrence of a single-maximum ice fabric within the firn or by structural firn anisotropy. Formation of the former cannot be explained with current fabric evolution theory and we conclude that our observations are dominated by firn anisotropy. This effect has not been considered in previous polarimetric radar studies. We show that ambiguities exist for disentangling the competing contributions of ice fabric and firn, but can be resolved by assuming that each effect dominates at different depths within the ice column. By demonstrating the sensitivity of polarimetric wide-angle surveys to firn anisotropy, this study highlights that near-surface radar polarimetry may open new avenues for investigating firn processes.

OPEN RESEARCH SECTION

The forward modeling and inversion codes are available at Oraschewski et al. (2025a) and the polarimetric CMP data at Oraschewski et al. (2025b).

ACKNOWLEDGMENTS

The authors thank editor Mathieu Morlighem, reviewer Alex Brisbourne and one anonymous reviewer for their constructive feedback that significantly improved this article. We acknowledge Kora Heidrich-Meisner for assisting the data acquisition. Field observations were supported by the Alfred-Wegener-Institut Helmholtz-Zentrum für Polar- und Meeresforschung (2016) through logistic grant AWI_ANT_18 (Drews). This study has been supported by the Studienstiftung des Deutschen Volkes (doctoral scholarship to FMO), the Deutsche Forschungsgemeinschaft (Grant DR 822/3-1), and the Open Access Publication Fund of the University of Tübingen. Open Access funding enabled and organized by Projekt DEAL.

4

CONCLUSIONS

This thesis presents two phase-sensitive radar acquisition methods specifically designed to detect deep englacial structures in mountain glaciers and vertical ice fabric anisotropy. Both features are shaped and deformed by ice dynamics. Therefore, the developed methods enhance our ability to investigate past ice deformation and ice-dynamical processes, such as englacial folding caused by a variable ice rheology. In addition, this thesis contributes to an improved understanding of radar signatures in phase-sensitive radar data and expands the fields of application of phase-sensitive and polarimetric RES, particularly by demonstrating the capability of radar to detect structural firn anisotropy. In the following, I assess whether the research objectives set in Section 1.4 have been achieved and discuss limitations and implications. Finally, I synthesize the general findings of the two presented studies.

4.1 EVALUATION OF RESEARCH OBJECTIVES

O1: DEVELOP A METHOD FOR DETECTING THE DEEP ENGLACIAL STRATIGRAPHY OF MOUNTAIN GLACIERS

Mobilizing the pRES results in a lightweight, power-efficient, phase-sensitive radar system. The system has been successfully deployed on Colle Gnifetti, where it extends the range over which englacial reflection horizons can be detected from the uppermost 30–50 % of the ice column to essentially the entire depth range. The improved detection capabilities, are on the one hand, attributed to the higher sensitivity of the pRES provided by the 1 s integration time of each chirp. On the other hand, the phase-sensitivity of the pRES enables SAR processing, which enhances the SNR by coherent integration of power along the radar profile. Although the long chirp duration limits the applicability of the system in its current form, the study demonstrates that technical advancements facilitate the detection of deep englacial structures in mountain glaciers and encourage the development of radar instruments specifically designed for this purpose.

O2: INVESTIGATE THE DEEP STRATIGRAPHY AND ORIGIN OF THE APPARENT ECHO-FREE ZONE AT COLLE GNIFETTI

In the second objective, I hypothesized that the drop in backscattered power observed by radar in the deep ice of Colle Gnifetti is caused by englacial folding. This was motivated by a discontinuity that has been observed in a Colle Gnifetti ice core (Hoffmann et al., 2018) and because complex ice deformation structures, such as englacial folding, have been imaged at many locations in the previously apparent echo-free zone of polar ice sheets. However, in the obtained data, the across-saddle profile shows an undisturbed and nearly flat englacial stratigraphy down to the bedrock. Therefore, the hypothesis could not be confirmed, and layer disturbances are not the primary cause of the reduced reflectivity. Instead, by comparing the radar profile with density and acidity data from local ice cores, a strong correlation between backscattered power and the acidity variability has been observed. The acidic impurity layers represent strong reflection interfaces and are attributed to increased anthropogenic pollution that is deposited on the glacier. In contrast, the drop in reflectivity in older ice is caused by the scarcity of acidic impurity layers prior to industrialization, when the natural background of acidity variations was primarily driven by major Saharan dust deposition events that occurred on decadal timescales.

Nevertheless, a contribution of layer disturbances to the formation of the low-reflective zone cannot be ruled out in general. The detection of the deep englacial layering in the upstream profile was limited due to technical issues during data acquisition. However, englacial structures originating from complex deformation would also most likely occur along this upstream profile, in particular, because the age-depth discontinuity has been observed at its upper end. Consequently, the reduced coherence might also be attributed to nonuniform englacial layering. As the implemented LO-SAR processing method was particularly designed to improve the imaging of specular reflection horizons in the across-saddle profile, it cannot resolve fold structures. I therefore suggest to repeat the upstream profile in a future study after the technical limitations have been solved and to implement a conventional SAR processing method that is better at resolving point scatterers. Together, this might allow to resolve the origin of the age-depth discontinuity and to study complex ice deformation processes at Colle Gnifetti.

O3: DEVELOP A PHASE-BASED RADAR TECHNIQUE FOR INFERRING VERTICAL ICE FABRIC ANISOTROPY

In chapter 3, a polarimetric CMP pRES survey was described. The obtained data demonstrate that phase-based wide-angle radar methods can detect both vertical and horizontal dielectric anisotropy with high accuracy. The dielectric anisotropy directly affects the propagation velocity of radar waves with different polarizations. As long as the radar antenna polarizations are not rotated by about 45° relative to the principal axis of the dielectric permittivity ellipse for a given propagation direction, different wave components are dominant in the HH and VV signals, respectively. The phase of an englacial reflection in a specific polarization is therefore determined by the dominant component. Because of this, polarimetric radar can essentially detect the propagation velocities of the fast and the slow wave polarizations independently of each other via the phase. Consequently, the observed phase difference signals are only weakly affected by errors in the antenna orientation, and the dielectric anisotropy can be inferred with significantly lower uncertainty than it would be possible with observation methods that are based on the reflection power.

However, polarimetric CMPs have two significant limitations: First, data acquisition is more laborious than for conventional quad-polarimetric radar measurements, which can efficiently be acquired along profiles (Ershadi et al., 2024). I therefore suggest using both methods complementarily by conducting polarimetric CMPs at selected ice-dynamically interesting study sites within more extensive grids of nadir-looking quad-polarimetric data. Moreover, it is noted that inferring the vertical anisotropy does not generally require a full polarimetric CMP. Fewer antenna postings are sufficient as long as individual reflections can be traced between the different postings.

The second limitation is given by the maximum antenna offset. Particularly in the interior of polar ice sheets, where the ice thickness exceeds one kilometer, significantly wider antenna separations than the $200\,\mathrm{m}$ used in the presented survey are required to achieve sufficiently oblique incidence angles at depth. FMCW radars require synchronization between the transmitter and receiver, and the use of long cables is restricted by cable losses. More extended wide-angle surveys therefore need to utilize post-processing synchronization techniques that achieve synchronization via the air wave (Bienert et al., 2022). Nevertheless, for the proposed polarimetric firn anisotropy studies, substantially smaller antenna separations of up to $50\,\mathrm{m}$ are sufficient, as firn anisotropy is primarily confined to the uppermost tens of meters.

O4: IMPLEMENT AN INVERSION METHOD FOR FULL ICE FABRIC ANISOTROPY TENSOR

Two phase-difference forward models for wave propagation in dielectrically anisotropic ice were developed. The ice fabric inversion framework is implemented using an eigenplane forward model based on Jordan et al. (2020a). In general, the inversion of the ice fabric anisotropy is restricted by the observed superimposed effect of firn anisotropy. Because of this, the implemented inversion assumes an ice fabric that evolves constantly with depth to highlight the predominant dielectric signatures. However, a more refined inversion would be possible and is particularly feasible below the anisotropic firn layer after disentangling the competing contributions of both effects.

Although one aim of the wide-angle radar survey was to infer tilted ice fabrics, the inversion assumes vertical fabric alignment. This is set because it matches the observed data and the ice fabric pattern expected for the flow conditions at the study site. Nonetheless, the inversion framework is easily adaptable to a configuration with a tilted vertical ice fabric eigenvector.

A single-layer forward model for wave propagation in arbitrary directions is implemented to assess the effects of misalignments between the CMP plane and an eigenplane of the ice fabric tensor. This forward model, moreover, depicts the phase-difference signatures of non-vertical ice fabric eigenvectors that can be observed in polarimetric CMPs. These synthetic experiments show that the optimal configuration for inferring the full ice fabric tensor is given by a CMP plane that matches the optic plane. In this case, tilted ice fabrics can be inferred from non-uniform phase-difference patterns at incidence angles greater than the optic angle.

O5: ANALYZE THE DIELECTRIC SIGNATURES OF STRUCTURAL FIRN ANISOTROPY.

In the polarimetric CMP, dielectric anisotropy due to structural firn anisotropy affects the observed phase differences at all depths. This is because radio waves that are transmitted and received at the surface always need to propagate through the firn before being reflected at deep reflection horizons. However, the implemented firn anisotropy inversion demonstrated a low sensitivity to the applied functional firn anisotropy relation. Therefore, the impact of firn anisotropy on deep reflections is determined by its depth-average, suggesting that it is possible to disentangle the effects of firn and ice fabric anisotropy below the firn.

To specifically study firn anisotropy with polarimetric radar, the effect on near-surface reflections needs to be analyzed. However, because of the vertical resolution of the pRES of approximately half a meter, its sensitivity in the uppermost $\sim 15\,\mathrm{m}$ is limited, preventing a more detailed firn anisotropy analysis with the presented data. For the suggested targeted polarimetric wide-angle studies of structural firn anisotropy and acquisition of ground-truth data for the remote sensing of firn, this study encourages the development of a dedicated phase-sensitive firn radar system that operates at UHF frequencies, which in addition, are better comparable to the frequency bands commonly used by satellite radar instruments.

4.2 SYNTHESIS AND IMPLICATIONS

4.2.1 IMPROVED UNDERSTANDING OF PHASE-SENSITIVE RADAR DATA FROM SPATIAL SURVEYING

In the mobile pRES survey as well as the polarimetric CMP survey, the spatial variation of phase-sensitive radar data has been analyzed. This stands in contrast to most previous pRES studies, which are typically conducted with quasi-monostatic antenna configurations at fixed locations to analyze temporal variations in reflector ranges or polarization-dependent traveltime variations along nadir propagation. Although spatial pRES surveys are more laborious, they offer a new perspective on interpreting phase-sensitive radar data.

Along-profile reflection range changes in the mobile pRES data clearly originate from the geometry of the englacial stratigraphy. Because of this, it was possible to demonstrate that the reference-corrected phase is constant along reflection horizons. Here, this characteristic of the corrected phase is utilized to improve and adapt the LO-SAR processing scheme introduced by Castelletti et al. (2019) to mobile pRES data. However, this observation also has consequences beyond mobile surveying. It implies that inferring absolute fine range offsets from the corrected phase, as suggested in previous studies, is not possible. Moreover, this finding endorses the development of new analysis techniques for pRES time-series data that are based on the reflection-constant corrected phase.

The polarimetric CMP data show low variability in polarization-dependent phase differences of individual reflections both with depth and with antenna separation. Again, this finding is relevant in the larger context because it highlights the accuracy of phase differences observed at single locations. More specifically, this observation suggests the development of new reflection-focused ice fabric inversion techniques for polarimetric nadir measurements. Typically employed phase-coherence methods require vertical smoothing, which results in a significantly reduced vertical resolution, the introduction of processing artifacts, and a drop in signal coherence at depth ranges with few reflections. By focusing the analysis on strong englacial reflections, these issues can be avoided, potentially facilitating to infer ice fabric anisotropy more reliably and at greater depth.

4.2.2 DETECTION OF UNINTENDED ENGLACIAL PROPERTIES

Both radar surveys could detect an englacial property that was not initially considered during survey planning. These properties are the englacial layer slopes, obtained as a byproduct during the LO-SAR processing of the mobile pRES data, and the structural firn anisotropy, revealed in the polarimetric wide-angle data. These observations may prove valuable for future research, underscoring the importance of developing new acquisition techniques for established geophysical instruments, which can promote scientific progress in unexpected ways.

4.2.3 DEMAND FOR APPLICATION-SPECIFIC RADAR SYSTEMS

The pRES was specifically designed to measure basal melt rates and to investigate ice–ocean coupling at ice shelves. Its success in doing so is reflected in a multitude of basal melt rate studies that have been published over the past two decades by various research groups, covering a range of ice shelves and ice streams. In this thesis, I applied the pRES in two substantially different survey types that analyze spatial phase signatures. In both studies, the applicability of the new acquisition methods has been demonstrated. However, these methods were also limited by specific characteristics of the pRES that are not ideal for the respective surveys, such as the long chirp duration or the low sensitivity in the near-surface. Consequently, this thesis demonstrates that advancements in radar hardware, data acquisition methods, and processing techniques can open up new applications for radar in glaciology, even after 60 years of radioglaciological research. However, to leverage this potential, new radar systems are required that are specifically designed for these new applications and radar targets. These systems can turn the proof-of-concept surveys presented in this thesis into standard acquisition methods, as the pRES did for observations of basal melt.

4.3 INSIGHTS INTO ICE DYNAMICS

Although the motivation for this thesis is to investigate ice-dynamical processes, the direct insights into ice dynamics provided by the presented studies are limited. In the first study, the hypothesized complex flow structures in the deep englacial stratigraphy of Colle Gnifetti could not be observed. The polarimetric CMP in the second study was deliberately conducted at a study site with a simple flow configuration to focus on validating the acquisition method. Consequently, both studies represent only first proof-of-concepts, and it is left to future research, ideally supported by newly designed application-specific radar systems, to apply these techniques on a broader scale and contribute to an improved understanding of ice dynamics.

A

SUPPLEMENT TO "LAYER-OPTIMIZED SYNTHETIC APERTURE RADAR PROCESSING WITH A MOBILE PHASE-SENSITIVE RADAR: A PROOF OF CONCEPT FOR DETECTING THE DEEP ENGLACIAL STRATIGRAPHY OF COLLE GNIFETTI, SWITZERLAND AND ITALY"

A.1 COMPARISON OF PROCESSING METHODS

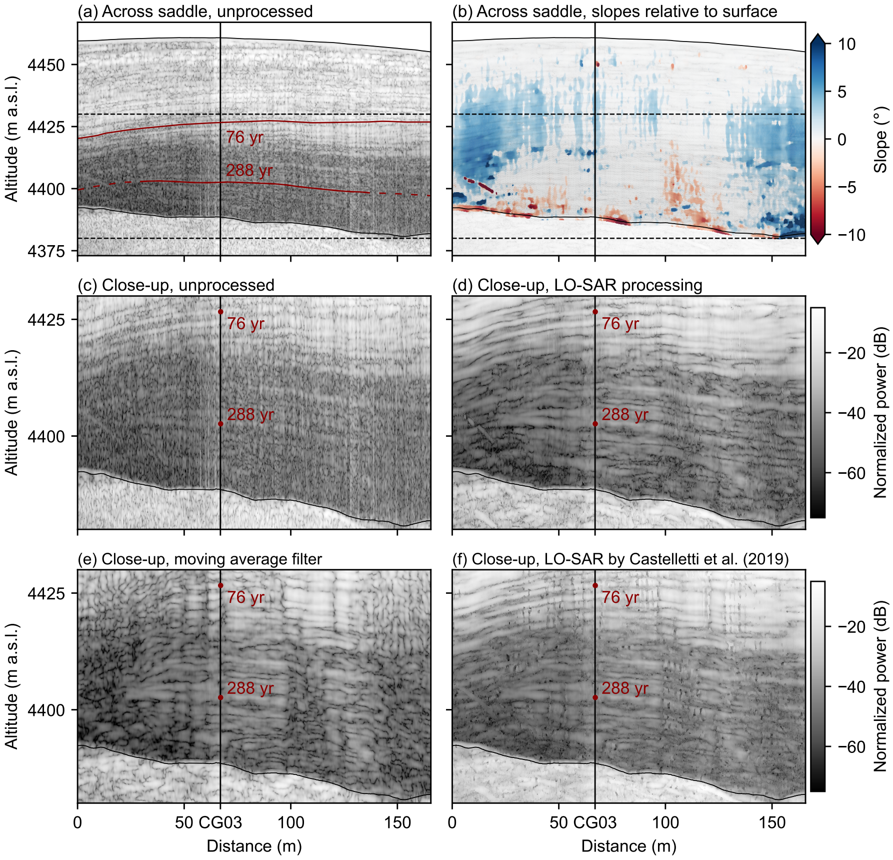

Figure A.1: Comparison of processing methods for across saddle radargram. (a) Unprocessed mobile pRES data and (b) englacial slopes relative to surface. (c–f) Close-up view of deep stratigraphy. (c) Without processing, (d) with LO-SAR processing as implemented in this study, (e) with moving average filtering and (f) with LO-SAR processing as implemented by Castelletti et al. (2019). The location of the CG03 ice core and traced IRHs are marked. Coherent averaging results in destructive interference where IRHs are sloped. Both LO-SAR processing approaches provide improved imaging of the deep stratigraphy. Closely spaced IRHs are better resolved by integrating the power along IRH slopes during LO-SAR processing (d), because destructive interference at the boundary between IRHs is amplified.

Phase-coherent radar processing techniques can either enhance or diminish radar imaging capabilities. Figure A.1 compares layer-optimized SAR (LO-SAR) processing, as implemented in this study, to moving average filtering and LO-SAR processing as implemented by Castelletti et al. (2019). In our LO-SAR processing implementation, the backscattered power is coherently integrated along internal reflection horizons (IRHs) after estimating their slopes (Figure A.1b). The other two methods integrate power along range bins, with (LO-SAR processing by Castelletti et al. (2019), Figure A.1f) and without (moving average filtering, Figure A.1e) correcting for along track phase gradients. Castelletti et al. (2019) compute the required phase shift by pointwise optimization of the signal-to-noise ratio. Here, we approximate their implementation by using the unfiltered slope estimates from our approach to correct for phase gradients in the raw signal before applying coherent integration along range bins. For all three processing methods, a synthetic aperture length or filtering window of $L_{\mathrm{SAR}} = 5\ \mathrm{m}$ is used.

Moving average filtering results in signal extinction due to destructive interference where IRHs are sloped. This is avoided during LO-SAR processing by correcting for the horizontal phase gradient associated with the IRH slopes, resulting in improved imaging of the deep englacial stratigraphy compared to the unprocessed data. In our LO-SAR implementation, the slopes of IRHs are initially estimated. This facilitates filtering these slopes prior to the coherent integration of power to remove outliers that for example occur at the boundary between two IRHs. Moreover, coherent summation can be performed directly along the englacial slopes. In this way, closely spaced IRHs are better resolved as the constructive interference at IRH centers and destructive interference at the IRH boundaries are enhanced.

B

SUPPORTING INFORMATION FOR "POLARIMETRIC WIDE-ANGLE RADAR DETECTS COMPETING SIGNATURES OF ICE FABRIC AND STRUCTURAL FIRN ANISOTROPY"

Falk M. Oraschewski[1], M. Reza Ershadi[1], Reinhard Drews[1]

[1]Department of Geosciences, University of Tübingen, Tübingen, Germany

Contents

1. Text B.1: Data aquisition and processing
    - B.1.1: Data acquisition
    - B.1.2: FMCW signal processing
    - B.1.3: Semi-automatic tracing of reflection hyperbolas
    - B.1.4: Phase unwrapping
2. Text B.2: VV–HH phase difference forward model for wave propagation in CMPs with arbitrary orientation
3. Text B.3: Estimation of firn anisotropy bias in the inversion of density and firn air content
4. Figures B.1 to B.7

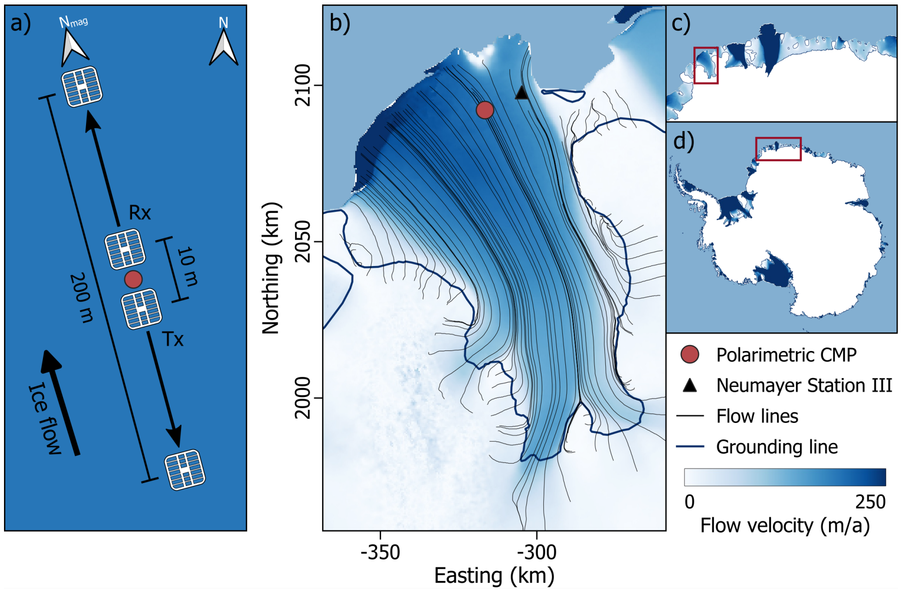

Figure B.1: CMP configuration and study site. (a) Orientation of CMP profile relative to magnetic North and ice flow direction. (b) Study site on Ekström ice shelf, (c) western Droning Maud Land, (d) Antarctica.

B.1 DATA AND PROCESSING

B.1.1 DATA ACQUISITION

Polarimetric common midpoint (CMP) data were acquired centrally on Ekström ice shelf, Droning Maud Land, Antarctica (Figure B.1; 70.703127°S, 8.603937°W) on February 24, 2023. The CMP profile was oriented toward magnetic North (15°W) which aligns with the ice flow direction (~ 18°W) at the site. We used the phase-sensitive Radio Echo Sounder (pRES) (Brennan et al., 2014) with skeleton slot antennas. The transmitter (Tx) and receiver (Rx) were connected with four $25\,\mathrm{m}$ low-loss coaxial cables, each, and separated from $10\,\mathrm{m}$ to $200\,\mathrm{m}$ in $2\,\mathrm{m}$ increments. At each position, three measurements were conducted: HH, HV and VV, representing CMP-parallel (H) and -perpendicular (V) orientations of the Tx (first letter) and Rx (second letter) antennas. For each increment and polarization, data were acquired with up to three different attenuator settings and five to ten subbursts. A constant setting of $(\mathrm{Attenuator1} = 30,\ \mathrm{AFGain} = -14)$ was used for all measurements and at large offsets additional data were collected with lower attenuation (not used in the analysis).

B.1.2 FMCW SIGNAL PROCESSING

The pRES data is processed following Brennan et al. (2014). The pRES transmits frequency-modulated continuous-wave (FMCW) signals with a center-frequency of $300\,\mathrm{MHz}$ and a bandwidth of $200\,\mathrm{MHz}$. During signal acquisition, the pRES mixes the received signal with the transmitted signal, resulting in a deramped waveform stored by the pRES. This waveform is a time-domain representation of the deramped frequency spectrum. The deramped frequency components correspond to a reflection range or, more specifically, a two-way traveltime (TWTT). They are obtained by a fast Fourier transform (FFT) of the deramped wave form and, therefore, are complex with the magnitude and argument representing the power and phase of the deramped frequency components. Prior to the FFT processing, the deramped waveform can be zero-padded by a padding factor p, which corresponds to a sync-interpolation of the deramped frequency signal (Oraschewski et al., 2024c).

We only consider the data acquired with the constant attenuator setting, as their signal strength are sufficient at all antenna offsets. Multiple subbursts are stacked. We use a padding factor of $p = 32$ to represent the position of peaks in the power spectrum as accurately as possible, improving the depiction of the TWTT signal (Figure 3.2h). A high padding factor is moreover beneficial for using power maxima as seed points during the semi-automatic reflection tracing (Supplements B.1.3).

After FFT processing, we crop the cable delay in the obtained frequency spectra. Finally, the complex frequency spectra for the HH configuration are multiplied by -1 to correct for a π-shift in the HH phase arising from a relative $180°$-rotation between Tx and Rx in this configuration.

B.1.3 SEMI-AUTOMATIC TRACING OF REFLECTION HYPERBOLAS

BASAL REFLECTION The ice–ocean interface is the strongest reflector in our data and we determine its TWTT as the traveltime bin with maximum power in each radar trace. Observed TWTT differences between HH and VV

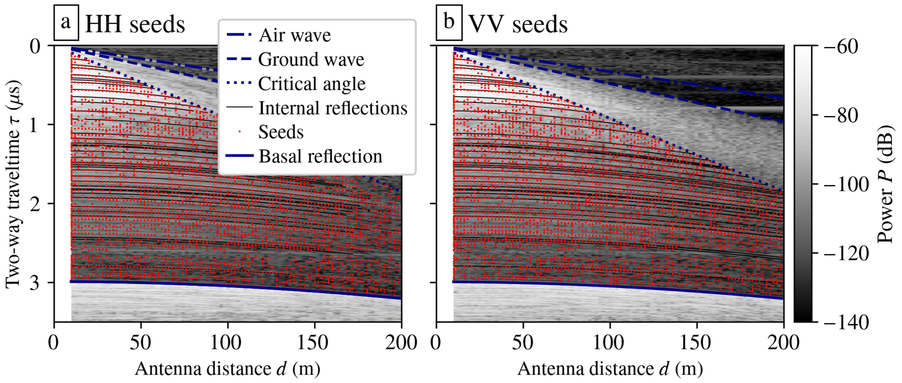

Figure B.2: (a) HH and (b) VV CMP profile with seed points and semi-automatically traced reflection hyperbolas.

are small compared to the width of the reflections. Therefore, we compute an average bed reflection hyperbola by fitting a hyperbola curve to the TWTT values of the HH and VV data, respectively, and take their range-average. As the fitting function, we use

$$\tau_{\text{hyper}}(z, d) = 2\frac{\sqrt{z^2 + (d/2)^2}}{v}, \tag{B.1}$$

with reflection range z, antenna distance d and mean wave velocity v. Power and phase of the basal reflection for both configurations are extracted along the average hyperbola.

ENGLACIAL REFLECTIONS Peaks in the power return serve as seed points (Figure B.2) to identify reflection hyperbolas that are detectable in both the HH and VV data, following a top-to-bottom approach. In all traces except the most central one, seed points are selected as power maxima with a minimum prominence of $15\,\mathrm{dB}$ and a minimum separation of $3 \times p$ bins. Seeds are masked at TWTTs before the critical angle, after the basal reflection and at TWTTs of 2.6 to $2.65\,\mu\mathrm{s}$, where an TWTT-independent artifact is apparent in the power. In the first trace, we search for peaks with a minimum prominence of $1\,\mathrm{dB}$ and average HH and VV seeds that are within $1 \times p$ bins, assuming that they originate from the same reflection. This provides for all potential reflection hyperbolas n' a list of the TWTTs $\tau_{n',1}$ at an antenna distance of $d_1 = 10\,\mathrm{m}$.

Now, we iterate over this list and compute for each element the TWTT of an expected reflection hyperbola $\tau_{n',\text{est}}$ with an estimated mean wave velocity $v_{n',\text{est}}$ by

$$\tau_{n',\text{est}}(\tau_{n',1}, d) = \frac{\sqrt{(\tau_{n',1} v_{n',\text{est}})^2 - d_1^2 + d^2}}{v_{n',\text{est}}}. \tag{B.2}$$

Using this estimated hyperbola, we extract and count the number of seeds in the HH and VV data that are within a distance of $1 \times p$ bins. If the count exceeds a certain number for both antenna configurations, we consider the estimated hyperbola to correspond to a true reflection horizon n. However, our initial velocity estimate is only an approximation and, as for the basal reflection, we determine a best matching average reflection hyperbola with a velocity v_{n} for the nth reflection by separately fitting Equation B.1 to all seed points in range for the HH and VV data and averaging both fits. Power and phase for HH and VV are extracted along the average reflection, but masked at all points where the power in the HH or VV data falls below $-120\,\mathrm{dB}$ or where a clear loss of phase coherence along the reflection occurs.

This approach is semi-automatic because both the count criterion and the definition of v_{est} need to be adjusted to the data. Here, we allow both variables to successively adapt to the reflections. For one antenna polarization, we require a minimum number of 5 seed points in range, which is increased by 1 after each successfully traced reflection. For the second polarization, at least half as many seed points are required. For v_{est}, we assume that the first reflection is described by a wave velocity of $v_{1,\mathrm{est}} = 2.07 \times 10^8\,\mathrm{m\,s^{-1}}$, matching the velocity of the ground wave. Subsequently, the optimized velocity for the nth reflection v_{n} is used as the velocity estimate for reflection $n+1$. To stabilize the velocity estimation below the firn, we assume an average velocity of $\overline{v_{\mathrm{firn}}} = 1.88 \times 10^8\,\mathrm{m\,s^{-1}}$ before $\tau_{\mathrm{firn}} = 0.9\,\mathrm{\mu s}$, and a wave velocity of ice $v_{\mathrm{ice}} = 1.68 \times 10^8\,\mathrm{m\,s^{-1}}$ thereafter. For reflection hyperbolas with $\tau_{n,1} > \tau_{\mathrm{firn}}$, the velocity estimate is computed by weighting both contributions:

$$v_{n,\mathrm{est}} = (v_{\mathrm{firn}}\tau_{\mathrm{firn}} + v_{\mathrm{ice}}(\tau_{n,1} - \tau_{\mathrm{firn}})/\tau_{n,1}). \tag{B.3}$$

B.1.4 PHASE UNWRAPPING

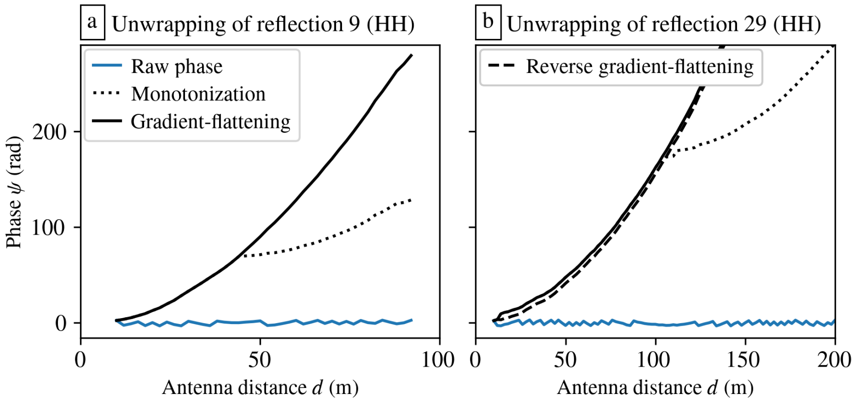

Figure B.3: Phase unwrapping along reflection hyperbolas. (a) Main unwrapping steps and (b) reverse gradient-flattening to address for overcorrections.

PHASE ALONG REFLECTION HYPERBOLAS The obtained phase signals can take values in the range $[0, 2\pi)$ and are ambiguous to integer-multiples of 2π (Arthern et al., 2013). However, when the antenna spacing of the CMP is sufficiently dense and regular, the differences between individual phase values along a reflection hyperbola are determined by the CMP geometry and can be unwrapped through a multi-stage process (Figure B.3). The ray path length increases monotonically with antenna distance, meaning that the phase must increase monotonically, as well. Therefore, the first unwrapping step is monotonization. For the nth reflection with M traces, this is achieved by iteratively applying:

$$\begin{aligned} &\text{For} && m = 2 \text{ to } M, \\ &\text{if} && \partial_m \psi_{n,m} = \psi_{n,m} - \psi_{n,m-1} < 0, \\ &\text{then} && \forall k \geq m: \quad \psi_{n,k} \leftarrow \psi_{n,k} + 2\pi. \end{aligned} \tag{B.4}$$

For antenna postings of $2\,\mathrm{m}$ and at large distances, the phase can increase by more than 2π between consecutive traces. These additional phase cycles can be recovered by flattening the phase gradient along the reflection:

$$\begin{aligned} &\text{For} && m = 3 \text{ to } M, \\ &\text{if} && \partial^2_m \psi_{n,m} - \text{mean}(\partial^2_{m'} \psi_{n,m'})^{m-1}_{\max(1,m-5)} < \pi, \\ &\text{then} && \forall k \geq m: \quad \psi_{n,k} \leftarrow \psi_{n,k} + 2\pi, \end{aligned} \tag{B.5}$$

where $\partial^2_m \psi_{n,m} = \partial_m \psi_{n,m} - \partial_m \psi_{n,m-1}$. Both the monotonization and the gradient-flattening algorithms can lead to overcorrection when phase uncertainties exceed $\partial_m \psi_{n,m}$. This can be addressed by applying the gradient-flattening process in reverse (Figure B.3b).

POLARIZATION-DEPENDENT PHASE DIFFERENCES Phase differences between the VV and HH polarizations $\Delta\psi_{\mathrm{VVHH}}$ inherit the 2π-ambiguity. However, birefringence can only cause gradual changes of these relative phase differences between adjacent reflections and traces. Therefore, the phase differences can be unwrapped by flattening in vertical and horizontal direction

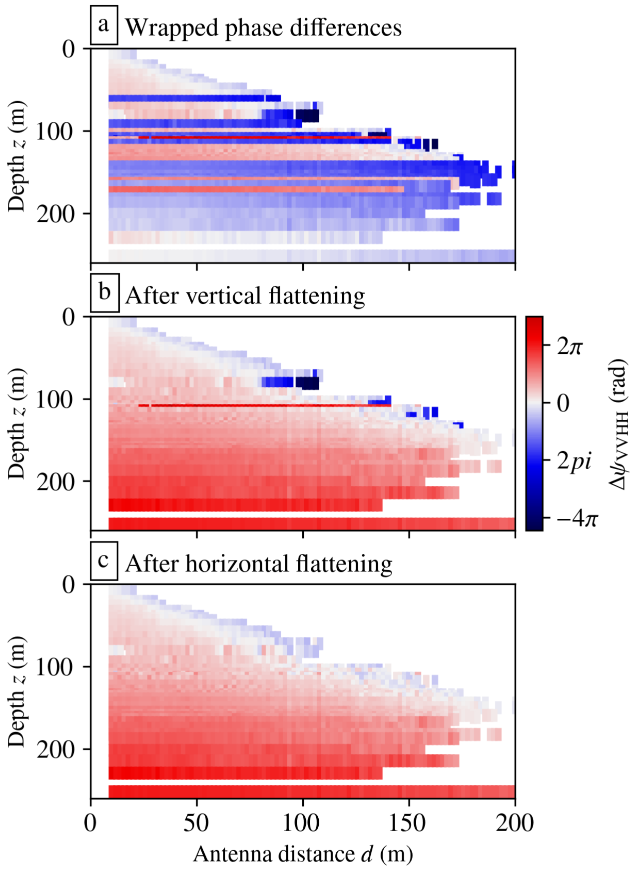

Figure B.4: Phase difference unwrapping. (a) Phase differences of a reflection are positive or negative, depending on whether the wrapped HH or VV phase attains a higher value in the $[0, 2\pi)$ range in the first trace. (b) Vertical flattening according to the first trace recovers the gradual phase difference evolution with depth. (c) Horizontal flattening unwraps equivalent phase jumps along individual reflection horizons. Phase shifts at $\sim 85\,\mathrm{m}$ depth that are smaller than 2π cannot be unwrapped.

(Figure B.4). Vertical flattening is executed according to changes in the phase difference of the first trace $\partial_n \Delta\psi_{n,1} = \Delta\psi_{n,1} - \Delta\psi_{n-1,1}$:

$$\begin{aligned} &\text{For} \quad n = 2 \text{ to } N, \\ &\text{if} \quad |\partial_n \Delta\psi_{n,1}| > \pi, \\ &\text{then} \quad \forall k \geq n: \;\; \psi_{k,m} \leftarrow \psi_{k,m} - \operatorname{sgn}(\partial_n \Delta\psi_{n,1}) 2\pi. \end{aligned} \tag{B.6}$$

Subsequently, horizontal flattening can be applied along each reflection hyperbola to recover the total phase difference evolution:

$$\begin{aligned} &\text{For} \quad m = 2 \text{ to } M, \\ &\text{if} \quad |\partial_m \Delta\psi_{n,m}| > \pi, \\ &\text{then} \quad \forall k \geq m: \;\; \psi_{n,k} \leftarrow \psi_{n,k} - \operatorname{sgn}(\partial_n \Delta\psi_{n,m}) 2\pi. \end{aligned} \tag{B.7}$$

B.2 VV–HH PHASE DIFFERENCE FORWARD MODEL FOR WAVE PROPAGATION IN CMPS WITH ARBITRARY ORIENTATION

To model radio wave propagation through ice in arbitrary direction wave depolarization effects need to be taken into account. These occur along propagation directions in which the polarization of a transmitted radio wave does not align with a principal axis of the permittivity ellipse for that direction. For a CMP survey with HH and VV antenna polarizations being parallel and perpendicular to the CMP incidence plane, depolarization occurs when the CMP profile is not parallel to an ice fabric eigenplane ($0° \neq \alpha \neq 90°$). In the following, we describe our implementation of the single-layer forward model from K. Matsuoka et al. (2009) for wave propagation in arbitrary direction.

The CMP geometry is defined by the single-layer thickness z, the azimuth α, describing the orientation of the CMP plane relative to the optic plane, and by the range of incidence angles θ, that can be defined relative to the antenna distances d. The one-way path length is given by $l = z/\cos(\theta)$. In the case of a non-vertical ice fabric, the permittivities encountered by the downward and upward propagating radio waves differ and need to be modeled separately. Therefore we define the incidence angle of the transmitted wave θ_d and the angle of reflection $\theta_\mathrm{u} = -\theta_\mathrm{d}$.

To describe the ice fabric, we use specfab (Rathmann et al., 2022) which includes functionality for fabric rotation. As described in the main text, the ice fabric strength is characterized by the three eigenvalues λ_1, λ_2 and λ_3 with their corresponding eigenvectors $\boldsymbol{v}_1$, $\boldsymbol{v}_2$ and $\boldsymbol{v}_3$. We now define the spatially fixed coordinate system $\boldsymbol{x}$, $\boldsymbol{y}$, $\boldsymbol{z}$, that in absence of fabric rotation corresponds to the eigenbasis. With this, arbitrary fabric orientations can be described by first rotating the ice fabric eigenbasis horizontally in the $\boldsymbol{xy}$-plane by φ, before tilting it in the $\boldsymbol{xz}$-plane by the tilt angle γ.

To compute the VV–HH phase differences for the defined CMP geometry and ice fabric, we iterate over all propagation directions of the transmitted radio wave defined by combinations of α and θ_d and separately compute the two possible polarizations for the downward and the corresponding upward ray paths. The computations for both directions are analog and we focus on describing the downward path. Instead of defining a specific coordinate system for each ray path, we associate $\boldsymbol{x}$ and $\boldsymbol{y}$ with the H and V polarization directions, respectively, and rotate the ice fabric such that $-\boldsymbol{z}$ aligns with the propagation direction. In practice, this is accomplished by rotating the ice fabric horizontally by $-\alpha$ and tilting it by $-\theta_\mathrm{d}$. In this configuration, the 'horizontal' components of the dielectric permittivity tensor

$$\boldsymbol{\varepsilon}'_\mathrm{h} = \begin{pmatrix} \varepsilon'_{x,x} & \varepsilon'_{x,y} \\ \varepsilon'_{y,x} & \varepsilon'_{y,y} \end{pmatrix}, \tag{B.8}$$

that correspond to the horizontal components of the ice fabric tensor, define the permittivity ellipse for propagation along the α-θ_d-direction. The eigenvectors ($\boldsymbol{v}_{1'}$, $\boldsymbol{v}_{2'}$) of $\boldsymbol{\varepsilon}'_\mathrm{h}$ and the associated eigenvalues ($\varepsilon'_{1'}$, $\varepsilon'_{2'}$) determine the possible polarizations and their permittivities, respectively. The $\varepsilon'_{1'}\varepsilon'_{2'}$-eigenbasis is rotated clockwise by Θ_d relative to the $\boldsymbol{xy}$-coordinate subspace.

The radio wave propagation model follows K. Matsuoka et al. (2009). Transmitted radio waves in $\boldsymbol{xy}$-coordinates are given by $\boldsymbol{W}_\mathrm{Tx,H} = (1, 0)$ and $\boldsymbol{W}_\mathrm{Tx,V} = (0, 1)$ for the H and V polarizations, respectively. They are split into the principle components by the rotation matrix

$$\boldsymbol{R}(\Theta_\mathrm{d}) = \begin{pmatrix} \cos\Theta_\mathrm{d} & \sin\Theta_\mathrm{d} \\ -\sin\Theta_\mathrm{d} & \cos\Theta_\mathrm{d} \end{pmatrix}. \tag{B.9}$$

Transmission of the radar wave along the downward path is described by the transmission matrix:

$$\boldsymbol{T}_\mathrm{d} = \begin{pmatrix} T_{1'} & 0 \\ 0 & T_{2'} \end{pmatrix}, \tag{B.10}$$

with the components

$$T_{1'} = \exp(ik_{1'}l), \tag{B.11a}$$
$$T_{2'} = \exp(ik_{2'}l), \tag{B.11b}$$

and the propagation constants

$$k_{1'} = 2\pi f_\mathrm{c}\sqrt{\varepsilon'_{1'}}/c, \tag{B.12a}$$
$$k_{2'} = 2\pi f_\mathrm{c}\sqrt{\varepsilon'_{2'}}/c. \tag{B.12b}$$

Here, $f_\mathrm{c} = 300\,\mathrm{MHz}$ is the center-frequency of the pRES and c the speed of light in vacuum. Conductivity is assumed to be horizontally isotropic and not included in Equation B.12a, because it cancels out when determining the relative phase differences. Scattering at the ice base is assumed to be isotropic with

$$\boldsymbol{S} = \begin{pmatrix} 1 & 0 \\ 0 & 1 \end{pmatrix}, \tag{B.13}$$

defined in $\boldsymbol{xy}$-coordinates. Upward propagation and the polarization of the receivers are described analogously.

Combining all steps results in the following expression for the received signal after two-way propagation:

$$s_{ij} = \boldsymbol{W}_{\mathrm{Rx,j}} \boldsymbol{R}(-\Theta_{\mathrm{u}}) \boldsymbol{T}_{\mathrm{u}} \boldsymbol{R}(\Theta_{\mathrm{u}}) \boldsymbol{S} \boldsymbol{R}(-\Theta_{\mathrm{d}}) \boldsymbol{T}_{\mathrm{d}} \boldsymbol{R}(\Theta_{\mathrm{d}}) \boldsymbol{W}^{\mathrm{T}}_{\mathrm{Tx,i}}. \tag{B.14}$$

with $i, j \in \{\mathrm{H}, \mathrm{V}\}$. Finally, the VV–HH phase difference is obtained by

$$\Delta\psi_{\mathrm{VVHH}} = \arg(s_{\mathrm{VV}}) - \arg(s_{\mathrm{HH}}), \tag{B.15}$$

and then wrapped into the range $[-\pi, \pi)$.

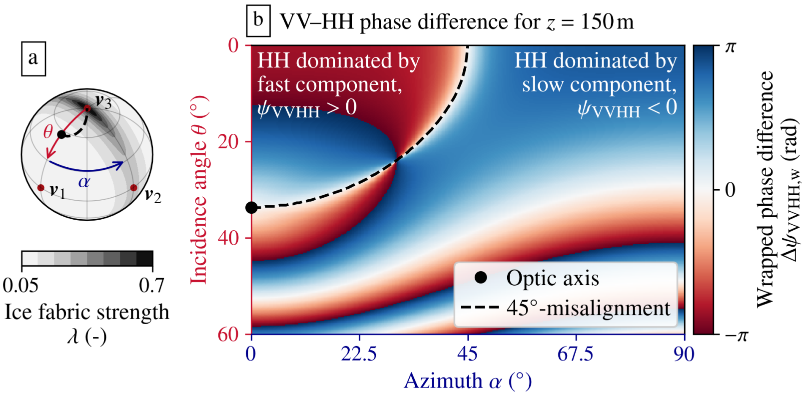

Figure B.5: (a) c-axis distribution for a vertical girdle ice fabric. Arrows indicate the range of downward incidence angles and azimuths along which phase differences are modeled. (b) Modeled VV–HH phase differences for wave propagation in arbitrary direction. Phase differences are generally decreasing for large θ. At nadir incidence ($\theta = 0°$) and for $\alpha \leq 45°$ phase difference are positive. A sign change occurs, when radar polarization and principal wave components are misaligned by $45°$, corresponding to a switch of the dominant wave components between the HH and VV polarizations.

FORWARD MODEL RESULTS The phase difference model capabilities are demonstrated for four characteristic ice fabric configurations (Figures B.5 and B.6): (i) A vertical girdle fabric with enhanced vertical c-axes alignment ($\boldsymbol{\lambda} = [0.05, 0.25, 0.7]$), (ii) the same ice fabric tilted along the optic plane by $\gamma = 15°$, (iii) a single-maximum fabric ($\boldsymbol{\lambda} = [0.15, 0.15, 0.7]$), and (iv) the same ice fabric tilted by $\gamma = 15°$.

The model results for the non-tilted vertical girdle fabric (Figures B.5) illustrate how depolarization occurs and the VV–HH phase differences are determined by the superposition of the principal wave components when radio waves do not propagate within an ice fabric eigenplane (at $0° < \alpha < 90°$). This is particularly highlighted by a line of propagation directions along which both antenna polarizations are rotated by $45°$ relative to the principal wave components. Along these directions, both HH and VV waves are equally split into the principal components so that $\Delta\psi_{\mathrm{VVHH}} = 0$. Accordingly, the traveltime–phase proportionality given by Equation 3.9 is not valid when depolarization occurs. However, we note that the phase difference switches abruptly across the $45°$-line, which in turns means that along most propagation directions one dominant wave component determines the phase of the HH and VV signals, respectively. This suggests that the phase is only weakly sensitive to small misalignments between radar polarization and principal wave directions, which explains the low moveout-variability observed in the phase differences and demonstrates that the forward model assumption of $\alpha = 0°$ holds for small misalignments of the CMP profile.

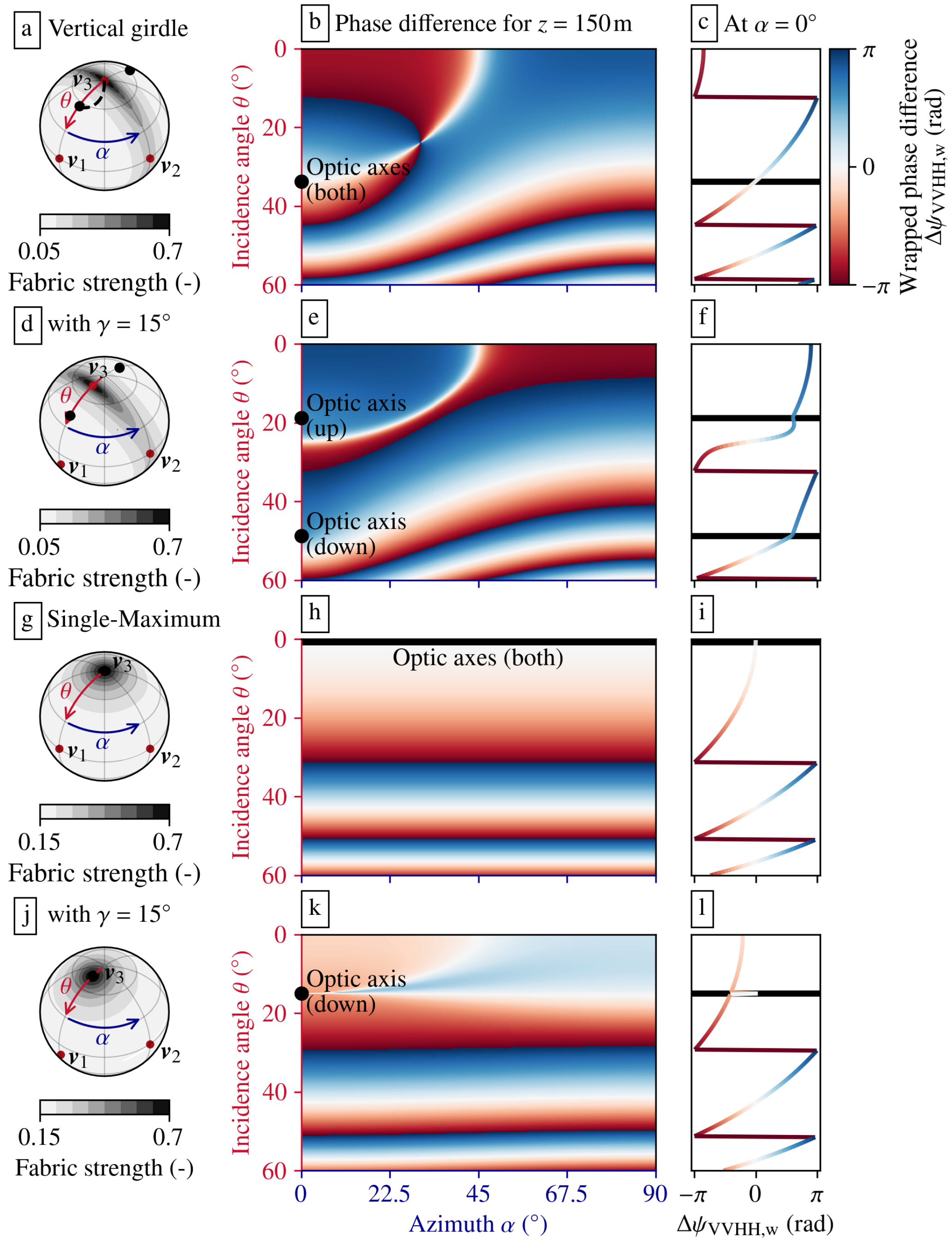

Figure B.6: VV–HH phase difference simulations for arbitrary propagation directions and tilted ice fabrics. (a, d, g, j) c-axes distributions. Model results for (b, e, h, k) all directions and (c, f, i, l) $\alpha = 0°$. Black dots and lines mark the optic axes for downward and/or upward propagation directions.

The tilted girdle fabric (Figure B.6d–f) exhibits a similar line where $\Delta\psi_{\mathrm{VVHH}} = 0$, which however is additionally altered by compensation effects between phase shifts arising during upward and downward propagation. These effects are highlighted in the phase-difference profile for $\alpha = 0$ (Figure B.6f), where non-uniform phase difference variations occur at incidence angles lying between the optic angles for upward and downward propagation. This suggests that it is possible to infer non-vertical ice fabrics via these non-uniform signatures in the phase differences, but also that it is not possible to identify a tilted ice fabric for incidence angles that are smaller than any of the optic angles.

Single-maximum ice fabrics (Figure B.6g–i) are uniaxial. Accordingly, for $\gamma = 0$, the phase differences are zero for wave propagation along nadir and independent of the azimuth. The tilted single-maximum fabric (Figure B.6j–l) features non-uniform effects around the optic axis that occur at smaller incidence angles and may be more easily detectable compared to the non-uniform signatures of the biaxial girdle fabric.

B.3 ESTIMATION OF FIRN ANISOTROPY BIAS IN THE INVERSION OF DENSITY AND FIRN AIR CONTENT

CMP surveying is a common technique for measuring firn density and firn air content with ground-penetrating radar (Eisen et al., 2002; Drews et al., 2016). These properties are inferred from the curvature of reflection hyperbolas which depends on the firn permittivity that for this application is assumed to solely be determined by the density of the firn. Vertical dielectric firn anisotropy can introduce a bias in these observations when carried out with an HH antenna orientation. Here, we aim to estimate the magnitude of this potential density bias.

For a single layer with a mean permittivity $\overline{\varepsilon'}$, the TWTT at an antenna distance d is given by

$$\tau_d = \sqrt{\tau_0^2 + \frac{d^2\overline{\varepsilon'}}{c^2}}, \tag{B.16}$$

where τ_0 is the TWTT for vertical propagation and c is the speed of light in vacuum (Eisen et al., 2002). The permittivity can therefore be inferred by the increase of the TWTT:

$$\overline{\varepsilon'} = \frac{c^2}{d^2}\left(\tau_d^2 - t_0^2\right). \tag{B.17}$$

For isotropic firn, the dependence of the permittivity on density ρ is expressed by the Looyenga mixture model (Equation 3.6, Looyenga, 1965):

$$\varepsilon' = \left(\frac{\rho}{\rho_{\mathrm{ice}}}\varepsilon_{\mathrm{ice}}'^{\,1/3} + (1 - \frac{\rho}{\rho_{\mathrm{ice}}})\right)^3, \tag{B.18}$$

where $\rho_{\mathrm{ice}} = 917\,\mathrm{kg\,m^{-3}}$ is the density and $\varepsilon'_{\mathrm{ice}} = 3.15$ is the permittivity of isotropic glacial ice. After inferring the mean permittivity above a reflection hyperbola according to Equation B.17 the density is therefore given by

$$\rho = \rho_{\mathrm{ice}}\frac{\varepsilon'^{1/3} - 1}{\varepsilon_{\mathrm{ice}}'^{\,1/3} - 1}. \tag{B.19}$$

For a single layer, τ_d can alternatively be expressed in terms of the incidence angle θ_d:

$$\tau_d = \frac{\tau_0}{\cos(\theta_d)} \tag{B.20}$$

and Equation B.17 can be rewritten as

$$\overline{\varepsilon'} = \frac{c^2\tau_0^2}{d^2}\left(\frac{1}{\cos^2(\theta_d)} - 1\right). \tag{B.21}$$

However, Equation B.20 is only valid for a single layer with dielectrically isotropic firn. To account for an incidence angle-dependent change of the permittivity due to dielectric anisotropy, a scaling factor can be introduced:

$$\begin{aligned}\tau_{d,\text{biased}} &= \frac{\tau_0}{\cos(\theta_d)} \cdot \frac{\sqrt{\varepsilon'_{\text{HH}}(\theta_d)}}{\sqrt{\overline{\varepsilon'}}} &\text{(B.22)}\\ &= \frac{\tau_0}{\cos(\theta_d)} \cdot \sqrt{\frac{\overline{\varepsilon'} + \Delta\varepsilon'_{\text{firn}}}{\sqrt{\overline{\varepsilon'}^2 \sin^2(\theta_d) + (\overline{\varepsilon'} + \Delta\varepsilon'_{\text{firn}})^2 \cos^2(\theta_d)}}}, &\text{(B.23)}\end{aligned}$$

where in the second step the permittivity of the HH polarization (Equation 3.3) has been applied, assuming that the vertical dielectric anisotropy of the firn $\Delta\varepsilon'_{\text{firn}}$ is constant across the single layer.

Inserting the biased TWTT into Equation B.17 and resolving it for the permittivity gives:

$$\overline{\varepsilon'_{\text{biased}}} = \frac{c^2\tau_0^2}{d^2}\left(\frac{\sqrt{\frac{\overline{\varepsilon'}+\Delta\varepsilon'_{\text{firn}}}{\sqrt{\overline{\varepsilon'}^2 \sin^2(\theta_d)+(\overline{\varepsilon'}+\Delta\varepsilon'_{\text{firn}})^2 \cos^2(\theta_d)}}}}{\cos^2(\theta_d)} - 1\right). \tag{B.24}$$

The relative bias of the inferred permittivity for a single layer with vertical firn anisotropy can therefore be approximated by:

$$R_{\text{bias}} = \frac{\frac{1}{\cos(\theta_d)} \cdot \sqrt{\frac{\overline{\varepsilon'}+\Delta\varepsilon'_{\text{firn}}}{\sqrt{\overline{\varepsilon'}^2 \sin^2(\theta_d)+(\overline{\varepsilon'}+\Delta\varepsilon'_{\text{firn}})^2 \cos^2(\theta_d)}}} - 1}{\frac{1}{\cos(\theta_d)} - 1}. \tag{B.25}$$

To obtain an intuition for the magnitude of the density bias, we now assume that the density is inferred for a single layer with a true mean density of $\rho = 500\,\text{kg}\,\text{m}^{-3}$ and a mean dielectric anisotropy of $\Delta\varepsilon'_{\text{firn}} = 0.04$. We further assume that the increase of the two-way traveltime is evaluated at an incidence angle of $\theta_d = 45°$ which corresponds to an antenna distance that equals twice the layer thickness. For this setup, we obtain a bias factor of $R_{\text{bias}} = 1.01$ that corresponds to an overestimation of the permittivity by $1\,\%$. Inserting the biased permittivity into the Looyenga mixture model (Equation B.18) provides an inferred density of $\rho = 508.2\,\text{kg}\,\text{m}^{-3}$, meaning that in this example the density would be overestimated by $1.6\,\%$. The porosity $\phi = 1 - \rho/\rho_{\text{ice}}$, and, therefore, the firn air content of the layer would on the other hand be underestimated by $2\,\%$.

Consequently, firn anisotropy can lead to a potential overestimation of the firn density and an underestimation of the firn air content on the order of a few percent when inverted with an HH-polarized CMP. This bias is of similar magnitude to other common sources of uncertainty in CMP-based density inversions, such as the radar resolution and inherent ambiguities of multi-layer inversions. Therefore, the overall validity of this approach is not significantly affected by the presence of firn anisotropy. Nonetheless, to reduce the potential bias in the inferred density and firn air content, we recommend to conduct future CMP surveys using a VV-antenna polarization, for which the permittivity is generally less dependent on the incidence angle.

B.4 FULL NADIR ICE FABRIC INVERSION

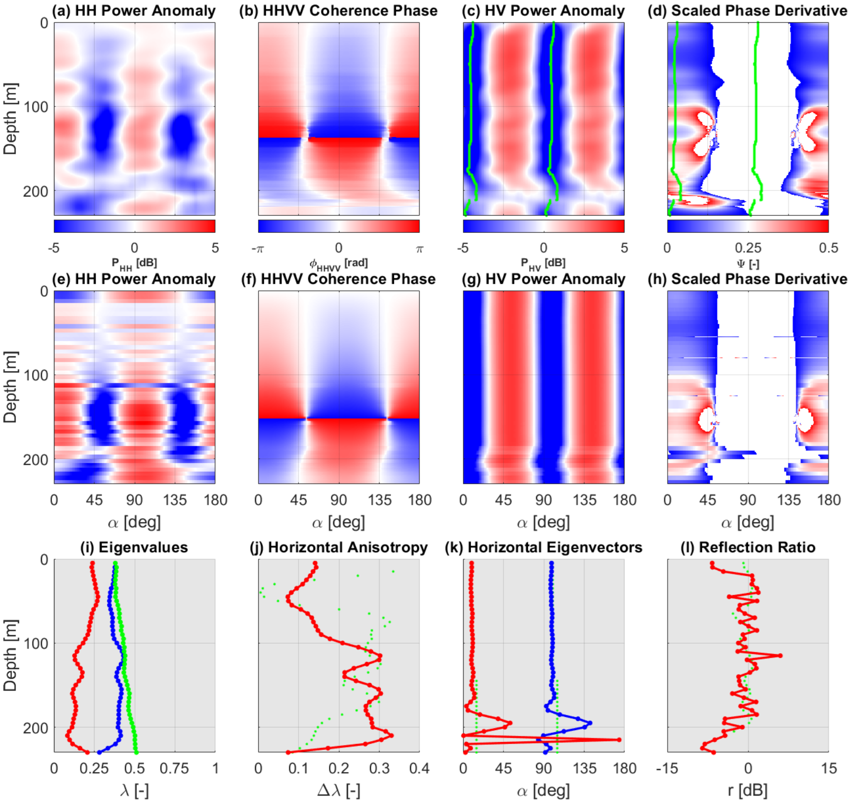

Figure B.7: Full results of nadir ice fabric inversion following Ershadi et al. (2022). (a–d) Radar metrics synthesized from quad-polarimetric (HH, HV, VV) observations for arbitrary azimuth angles α. (e-h) Inversion results for these metrics. (i) Inverted eigenvalues, given by the inferred (j) horizontal anisotropy and (l) reflection ratios. (k) Orientation of horizontal eigenvectors, indicating a rotation of the ice fabric eigenplanes by about 10° relative to the HH and VV orientations.

BIBLIOGRAPHY

Ackley, S. F., & Keliher, T. E. (1979). Ice sheet internal radio-echo reflections and associated physical property changes with depth. *Journal of Geophysical Research: Solid Earth*, *84*(B10), 5675–5680. https://doi.org/10.1029/JB084iB10p05675

Alean, J., Haeberli, W., & Schädler, B. (1983). Snow accumulation, firn temperature and solar radiation in the area of the Colle Gnifetti core drilling site (Monte Rosa, Swiss Alps): Distribution patterns and interrelationships. *Zeitschrift für Gletscherkunde und Glazialgeologie*, *19*(2), 131–147. http://hdl.handle.net/10013/epic.40215.d001

Alfred-Wegener-Institut Helmholtz-Zentrum für Polar- und Meeresforschung. (2016). Neumayer III and Kohnen Station in Antarctica operated by the Alfred Wegener Institute. *Journal of large-scale research facilities*, *2*, A85. https://doi.org/10.17815/jlsrf-2-152

Alley, R. B. (1987a). Firn densification by grain-boundary sliding: A first model. *Journal de Physique Colloques*, *48*(C1), C1-249–C1-256. https://doi.org/10.1051/jphyscol:1987135

Alley, R. B. (1987b). Texture of polar firn for remote sensing. *Annals of Glaciology*, *9*, 1–4. https://doi.org/10.3189/S0260305500200670

Alley, R. B., Cuffey, K. M., Bassis, J. N., Alley, K. E., Wang, S., Parizek, B. R., Anandakrishnan, S., Christianson, K., & DeConto, R. M. (2023). Iceberg calving: Regimes and transitions. *Annual Review of Earth and Planetary Sciences*, *51*, 189–215. https://doi.org/10.1146/annurev-earth-032320-110916

Alley, R. B., Anandakrishnan, S., Christianson, K., Horgan, H. J., Muto, A., Parizek, B. R., Pollard, D., & Walker, R. T. (2015). Oceanic forcing of ice-sheet retreat: West Antarctica and more. *Annual Review of Earth and Planetary Sciences*, *43*, 207–231. https://doi.org/10.1146/annurev-earth-060614-105344

An, S.-I., Moon, J.-Y., Dijkstra, H. A., Yang, Y.-M., & Song, H. (2024). Antarctic meltwater reduces the Atlantic meridional overturning circulation through oceanic freshwater transport and atmospheric teleconnections. *Communications Earth & Environment*, *5*(1), 1–9. https://doi.org/10.1038/s43247-024-01670-7

Arcone, S. A., Jacobel, R., & Hamilton, G. (2012). Unconformable stratigraphy in East Antarctica: Part I. Large firn cosets, recrystallized growth, and model evidence for intensified accumulation. *Journal of Glaciology*, *58*(208), 240–252. https://doi.org/10.3189/2012JoJ11J044

Arcone, S. A., Spikes, V. B., & Hamilton, G. S. (2005). Stratigraphic variation within polar firn caused by differential accumulation and ice flow: Interpretation of a 400 MHz short-pulse radar profile from West Antarctica. *Journal of Glaciology*, *51*(174), 407–422. https://doi.org/10.3189/172756505781829151

Arthern, R. J., J. Corr, H. F., Gillet-Chaulet, F., Hawley, R. L., & Morris, E. M. (2013). Inversion for the density-depth profile of polar firn using a stepped-frequency radar. *Journal of Geophysical Research: Earth Surface*, *118*(3), 1257–1263. https://doi.org/10.1002/jgrf.20089

Azuma, N. (1994). A flow law for anisotropic ice and its application to ice sheets. *Earth and Planetary Science Letters*, *128*(3–4), 601–614. https://doi.org/10.1016/0012-821X(94)90173-2

Bamber, J. L., Vaughan, D. G., & Joughin, I. (2000). Widespread complex flow in the interior of the Antarctic Ice Sheet. *Science*, *287*(5456), 1248–1250. https://doi.org/10.1126/science.287.5456.1248

Bamber, J. L., Westaway, R. M., Marzeion, B., & Wouters, B. (2018). The land ice contribution to sea level during the satellite era. *Environmental Research Letters*, *13*(6), 063008. https://doi.org/10.1088/1748-9326/aac2f0

Bell, R. E., Ferraccioli, F., Creyts, T. T., Braaten, D., Corr, H., Das, I., Damaske, D., Frearson, N., Jordan, T., Rose, K., Studinger, M., & Wolovick, M. (2011). Widespread persistent thickening of the East Antarctic Ice Sheet by freezing from the base. *Science*, *331*(6024), 1592–1595. https://doi.org/10.1126/science.1200109

Bell, R. E., Tinto, K., Das, I., Wolovick, M., Chu, W., Creyts, T. T., Frearson, N., Abdi, A., & Paden, J. D. (2014). Deformation, warming and softening of Greenland's ice by refreezing meltwater. *Nature Geoscience*, *7*(7), 497–502. https://doi.org/10.1038/ngeo2179

Bender, M. L. (2002). Orbital tuning chronology for the Vostok climate record supported by trapped gas composition. *Earth and Planetary Science Letters*, *204*(1), 275–289. https://doi.org/10.1016/S0012-821X(02)00980-9

Berends, C. J., Goelzer, H., Reerink, T. J., Stap, L. B., & van de Wal, R. S. W. (2022). Benchmarking the vertically integrated ice-sheet model IMAU-ICE (version 2.0). *Geoscientific Model Development*, *15*(14), 5667–5688. https://doi.org/10.5194/gmd-15-5667-2022

Bienert, N. L., Schroeder, D. M., Peters, S. T., MacKie, E. J., Dawson, E. J., Siegfried, M. R., Sanda, R., & Christoffersen, P. (2022). Post-processing synchronized bistatic radar for long offset glacier sounding. *IEEE Transactions on Geoscience and Remote Sensing*, *60*, 1–17. https://doi.org/10.1109/TGRS.2022.3147172

Bingham, R. G., Bodart, J. A., Cavitte, M. G. P., Chung, A., Sanderson, R. J., Sutter, J. C. R., Eisen, O., Karlsson, N. B., MacGregor, J. A., Ross, N., Young, D. A., Ashmore, D. W., Born, A., Chu, W., . . . Zuhr, A. (2025). Review article: AntArchitecture – building an age–depth model from Antarctica's radiostratigraphy to explore ice-sheet evolution. *The Cryosphere*, *19*(10), 4611–4655. https://doi.org/10.5194/tc-19-4611-2025

Bodart, J. A., Bingham, R. G., Ashmore, D. W., Karlsson, N. B., Hein, A. S., & Vaughan, D. G. (2021). Age-depth stratigraphy of Pine Island Glacier inferred from airborne radar and ice-core chronology. *Journal of Geophysical Research: Earth Surface*, *126*(4), e2020JF005927. https://doi.org/10.1029/2020JF005927

Bohleber, P. (2011). *Ground-penetrating radar assisted ice core research: The challenge of Alpine glaciers and dielectric ice properties* [Doctoral dissertation, Heidelberg University]. https://doi.org/10.11588/heidok.00012800

Bohleber, P., Erhardt, T., Spaulding, N., Hoffmann, H., Fischer, H., & Mayewski, P. (2018). Temperature and mineral dust variability recorded in two low-accumulation Alpine ice cores over the last millennium.

Climate of the Past, *14*(1), 21–37. https://doi.org/10.5194/cp-14-21-2018

Bohleber, P., Wagner, N., & Eisen, O. (2012). Permittivity of ice at radio frequencies: Part II. Artificial and natural polycrystalline ice. *Cold Regions Science and Technology*, *83–84*, 13–19. https://doi.org/10.1016/j.coldregions.2012.05.010

Bons, P. D., Jansen, D., Mundel, F., Bauer, C. C., Binder, T., Eisen, O., Jessell, M. W., Llorens, M.-G., Steinbach, F., Steinhage, D., & Weikusat, I. (2016). Converging flow and anisotropy cause large-scale folding in Greenland's ice sheet. *Nature Communications*, *7*(1), 11427. https://doi.org/10.1038/ncomms11427

Bons, P. D., Kleiner, T., Llorens, M.-G., Prior, D. J., Sachau, T., Weikusat, I., & Jansen, D. (2018). Greenland Ice Sheet: Higher nonlinearity of ice flow significantly reduces estimated basal motion. *Geophysical Research Letters*, *45*(13), 6542–6548. https://doi.org/10.1029/2018GL078356

Born, A., & Robinson, A. (2021). Modeling the Greenland englacial stratigraphy. *The Cryosphere*, *15*(9), 4539–4556. https://doi.org/10.5194/tc-15-4539-2021

Brennan, P. V., Lok, L. B., Nicholls, K., & Corr, H. (2014). Phase-sensitive FMCW radar system for high-precision Antarctic ice shelf profile monitoring. *IET Radar, Sonar & Navigation*, *8*(7), 776–786. https://doi.org/10.1049/iet-rsn.2013.0053

Brisbourne, A. M., Martín, C., Smith, A. M., Baird, A. F., Kendall, J. M., & Kingslake, J. (2019). Constraining recent ice flow history at Korff Ice Rise, West Antarctica, using radar and seismic measurements of ice fabric. *Journal of Geophysical Research: Earth Surface*, *124*(1), 175–194. https://doi.org/10.1029/2018JF004776

Buizert, C., Cuffey, K. M., Severinghaus, J. P., Baggenstos, D., Fudge, T. J., Steig, E. J., Markle, B. R., Winstrup, M., Rhodes, R. H., Brook, E. J., Sowers, T. A., Clow, G. D., Cheng, H., Edwards, R. L., ... Taylor, K. C. (2015). The WAIS Divide deep ice core WD2014 chronology – Part 1: Methane synchronization (68–31 ka BP) and the gas age–ice age difference. *Climate of the Past*, *11*(2), 153–173. https://doi.org/10.5194/cp-11-153-2015

Case, E., & Kingslake, J. (2022). Phase-sensitive radar as a tool for measuring firn compaction. *Journal of Glaciology*, *68*(267), 139–152. https://doi.org/10.1017/jog.2021.83

Castelletti, D., Schroeder, D. M., Hensley, S., Grima, C., Ng, G., Young, D., Gim, Y., Bruzzone, L., Moussessian, A., & Blankenship, D. D. (2017). An interferometric approach to cross-track clutter detection in two-channel VHF radar sounders. *IEEE Transactions on Geoscience and Remote Sensing*, *55*(11), 6128–6140. https://doi.org/10.1109/TGRS.2017.2721433

Castelletti, D., Schroeder, D. M., Mantelli, E., & Hilger, A. (2019). Layer optimized SAR processing and slope estimation in radar sounder data. *Journal of Glaciology*, *65*(254), 983–988. https://doi.org/10.1017/jog.2019.72

Cauvy-Fraunié, S., & Dangles, O. (2019). A global synthesis of biodiversity responses to glacier retreat. *Nature Ecology & Evolution*, *3*(12), 1675–1685. https://doi.org/10.1038/s41559-019-1042-8

Cavitte, M. G. P., Blankenship, D. D., Young, D. A., Schroeder, D. M., Parrenin, F., Lemeur, E., Macgregor, J. A., & Siegert, M. J. (2016). Deep radiostratigraphy of the East Antarctic plateau: Connecting the Dome C and Vostok ice core sites. *Journal of Glaciology*, *62*(232), 323–334. https://doi.org/10.1017/jog.2016.11

Cavitte, M. G. P., Parrenin, F., Ritz, C., Young, D. A., Van Liefferinge, B., Blankenship, D. D., Frezzotti, M., & Roberts, J. L. (2018). Accumulation patterns around Dome C, East Antarctica, in the last 73 kyr. *The Cryosphere*, *12*(4), 1401–1414. https://doi.org/10.5194/tc-12-1401-2018

Clifford, H. M., Spaulding, N. E., Kurbatov, A. V., More, A., Korotkikh, E. V., Sneed, S. B., Handley, M., Maasch, K. A., Loveluck, C. P., Chaplin, J., McCormick, M., & Mayewski, P. A. (2019). A 2000 year Saharan dust event proxy record from an ice core in the European Alps. *Journal of Geophysical Research: Atmospheres*, *124*(23), 12882–12900. https://doi.org/10.1029/2019JD030725

Corr, H. F. J., Jenkins, A., Nicholls, K. W., & Doake, C. S. M. (2002). Precise measurement of changes in ice-shelf thickness by phase-sensitive radar to determine basal melt rates. *Geophysical Research Letters*, *29*(8). https://doi.org/10.1029/2001GL014618

Cuffey, K. M., & Paterson, W. S. B. (2010). *The physics of glaciers* (4th ed). Butterworth-Heinemann/Elsevier.

Dall, J. (2007). InSAR elevation bias caused by penetration into uniform volumes. *IEEE Transactions on Geoscience and Remote Sensing*, *45*(7), 2319–2324. https://doi.org/10.1109/TGRS.2007.896613

Dall, J. (2010). Ice sheet anisotropy measured with polarimetric ice sounding radar. *2010 IEEE International Geoscience and Remote Sensing Symposium (IGARSS)*, 2507–2510. https://doi.org/10.1109/IGARSS.2010.5653528

Davison, B. J., Hogg, A. E., Gourmelen, N., Jakob, L., Wuite, J., Nagler, T., Greene, C. A., Andreasen, J., & Engdahl, M. E. (2023). Annual mass budget of Antarctic ice shelves from 1997 to 2021. *Science Advances*, *9*(41), eadi0186. https://doi.org/10.1126/sciadv.adi0186

Delcourt, C., Van Liefferinge, B., Nolan, M., & Pattyn, F. (2013). The climate memory of an Arctic polythermal glacier. *Journal of Glaciology*, *59*(218), 1084–1092. https://doi.org/10.3189/2013JoG12J109

Diez, A., Eisen, O., Hofstede, C., Bohleber, P., & Polom, U. (2013). Joint interpretation of explosive and vibroseismic surveys on cold firn for the investigation of ice properties. *Annals of Glaciology*, *54*(64), 201–210. https://doi.org/10.3189/2013AoG64A200

Diez, A., Eisen, O., Weikusat, I., Eichler, J., Hofstede, C., Bohleber, P., Bohlen, T., & Polom, U. (2014). Influence of ice crystal anisotropy on seismic velocity analysis. *Annals of Glaciology*, *55*(67), 97–106. https://doi.org/10.3189/2014AoG67A002

Doake, C. S. M., Corr, H. F. J., & Jenkins, A. (2002). Polarization of radio waves transmitted through Antarctic ice shelves. *Annals of Glaciology*, *34*, 165–170. https://doi.org/10.3189/172756402781817572

Drews, R. (2015). Evolution of ice-shelf channels in Antarctic ice shelves. *The Cryosphere*, *9*(3), 1169–1181. https://doi.org/10.5194/tc-9-1169-2015

Drews, R., Brown, J., Matsuoka, K., Witrant, E., Philippe, M., Hubbard, B., & Pattyn, F. (2016). Constraining variable density of ice shelves using wide-angle radar measurements. *The Cryosphere*, *10*(2), 811–823. https://doi.org/10.5194/tc-10-811-2016

Drews, R., Eisen, O., Steinhage, D., Weikusat, I., Kipfstuhl, S., & Wilhelms, F. (2012). Potential mechanisms for anisotropy in ice-penetrating radar data. *Journal of Glaciology*, *58*(209), 613–624. https://doi.org/10.3189/2012JoG11J114

Drews, R., Eisen, O., Weikusat, I., Kipfstuhl, S., Lambrecht, A., Steinhage, D., Wilhelms, F., & Miller, H. (2009). Layer disturbances and the radio-echo free zone in ice sheets. *The Cryosphere*, *3*(2), 195–203. https://doi.org/10.5194/tc-3-195-2009

Duval, P., Ashby, M. F., & Anderman, I. (1983). Rate-controlling processes in the creep of polycrystalline ice. *The Journal of Physical Chemistry*, *87*(21), 4066–4074. https://doi.org/10.1021/j100244a014

Eisen, O., Bauder, A., Lüthi, M., Riesen, P., & Funk, M. (2009). Deducing the thermal structure in the tongue of Gornergletscher, Switzerland, from radar surveys and borehole measurements. *Annals of Glaciology*, *50*(51), 63–70. https://doi.org/10.3189/172756409789097612

Eisen, O., Hamann, I., Kipfstuhl, S., Steinhage, D., & Wilhelms, F. (2007). Direct evidence for continuous radar reflector originating from changes in crystal-orientation fabric. *The Cryosphere*, *1*(1), 1–10. https://doi.org/10.5194/tc-1-1-2007

Eisen, O., Nixdorf, U., Wilhelms, F., & Miller, H. (2002). Electromagnetic wave speed in polar ice: Validation of the common-midpoint technique with high-resolution dielectric-profiling and γ-density measurements. *Annals of Glaciology*, *34*, 150–156. https://doi.org/10.3189/172756402781817509

Eisen, O., Nixdorf, U., Keck, L., & Wagenbach, D. (2003). Alpine ice cores and ground penetrating radar: Combined investigations for glaciological and climatic interpretations of a cold Alpine ice body. *Tellus B*, *55*(5), 1007–1017. https://doi.org/10.1034/j.1600-0889.2003.00080.x

Eisen, O., Nixdorf, U., Wilhelms, F., & Miller, H. (2004). Age estimates of isochronous reflection horizons by combining ice core, survey, and synthetic radar data. *Journal of Geophysical Research: Solid Earth*, *109*(B4), 2003JB002858. https://doi.org/10.1029/2003JB002858

Elsworth, C. W., Schroeder, D. M., & Siegfried, M. R. (2020). Interpreting englacial layer deformation in the presence of complex ice flow history with synthetic radargrams. *Annals of Glaciology*, *61*(81), 206–213. https://doi.org/10.1017/aog.2019.41

EPICA community members. (2004). Eight glacial cycles from an Antarctic ice core. *Nature*, *429*(6992), 623–628. https://doi.org/10.1038/nature02599

Ershadi, M. R., Drews, R., Hawkins, J. D., Elliott, J., Lines, A. P., Koch, I., & Eisen, O. (2024). Autonomous rover enables radar profiling of ice-fabric properties in Antarctica. *IEEE Transactions on Geoscience and Remote Sensing*, 1–1. https://doi.org/10.1109/TGRS.2024.3394594

Ershadi, M. R., Drews, R., Martín, C., Eisen, O., Ritz, C., Corr, H., Christmann, J., Zeising, O., Humbert, A., & Mulvaney, R. (2022). Polarimetric radar reveals the spatial distribution of ice fabric at domes and divides in East Antarctica. *The Cryosphere*, *16*(5), 1719–1739. https://doi.org/10.5194/tc-16-1719-2022

Ershadi, M. R., Drews, R., Tison, J.-L., Martín, C., Henry, A. C. J., Oraschewski, F. M., Tsibulskaya, V., Sun, S., Wauthy, S., Koch, I., Bons, P. D., Eisen, O., & Pattyn, F. (2025). Investigating the dynamic history of a promontory ice rise using radar data. *Journal of Glaciology*, *71*, e1. https://doi.org/10.1017/jog.2024.70

Evans, S., & Smith, B. M. E. (1969). A radio echo equipment for depth sounding in polar ice sheets. *Journal of Physics E: Scientific Instruments*, *2*(2), 131. https://doi.org/10.1088/0022-3735/2/2/302

Fan, S., Hager, T. F., Prior, D. J., Cross, A. J., Goldsby, D. L., Qi, C., Negrini, M., & Wheeler, J. (2020). Temperature and strain controls on ice deformation mechanisms: Insights from the microstructures of samples deformed to progressively higher strains at −10, −20 and −30°C. *The Cryosphere*, *14*(11), 3875–3905. https://doi.org/10.5194/tc-14-3875-2020

Faria, S. H., Weikusat, I., & Azuma, N. (2014). The microstructure of polar ice. Part I: Highlights from ice core research. *Journal of Structural Geology*, *61*, 2–20. https://doi.org/10.1016/j.jsg.2013.09.010

Fischer, G., Papathanassiou, K., & Hajnsek, I. (2019). Modeling multifrequency pol-InSAR data from the percolation zone of the Greenland Ice Sheet. *IEEE Transactions on Geoscience and Remote Sensing*, *57*(4), 1963–1976. https://doi.org/10.1109/TGRS.2018.2870301

Franke, S., Bons, P. D., Westhoff, J., Weikusat, I., Binder, T., Streng, K., Steinhage, D., Helm, V., Eisen, O., Paden, J. D., Eagles, G., & Jansen, D. (2022). Holocene ice-stream shutdown and drainage basin reconfiguration in northeast Greenland. *Nature Geoscience*, *15*(12), 995–1001. https://doi.org/10.1038/s41561-022-01082-2

Franke, S., Wolovick, M., Drews, R., Jansen, D., Matsuoka, K., & Bons, P. D. (2024). Sediment freeze-on and transport near the onset of a fast-flowing glacier in East Antarctica. *Geophysical Research Letters*, *51*(6), e2023GL107164. https://doi.org/10.1029/2023GL107164

Freitag, J., Kerch, J., Hoffmann, H., Spaulding, N., & Bohleber, P. (2018). *XCT density from the Alpine ice core KCC (2013)*. [dataset]. PANGAEA. https://doi.org/10.1594/PANGAEA.887691

Freitag, J., Kipfstuhl, S., Laepple, T., & Wilhelms, F. (2013). Impurity-controlled densification: A new model for stratified polar firn. *Journal of Glaciology*, *59*(218), 1163–1169. https://doi.org/10.3189/2013JoG13J042

Freitag, J., Wilhelms, F., & Kipfstuhl, S. (2004). Microstructure-dependent densification of polar firn derived from X-ray microtomography. *Journal of Glaciology*, *50*(169), 243–250. https://doi.org/10.3189/172756504781830123

Fujita, S., Goto-Azuma, K., Hirabayashi, M., Hori, A., Iizuka, Y., Motizuki, Y., Motoyama, H., & Takahashi, K. (2016). Densification of layered firn in the ice sheet at Dome Fuji, Antarctica. *Journal of Glaciology*, *62*(231), 103–123. https://doi.org/10.1017/jog.2016.16

Fujita, S., Hirabayashi, M., Goto-Azuma, K., Dallmayr, R., Satow, K., Zheng, J., & Dahl-Jensen, D. (2014). Densification of layered firn of the ice sheet at NEEM, Greenland. *Journal of Glaciology*, *60*(223), 905–921. https://doi.org/10.3189/2014JoG14J006

Fujita, S., Maeno, H., & Matsuoka, K. (2006). Radio-wave depolarization and scattering within ice sheets: A matrix-based model to link radar and ice-core measurements and its application. *Journal of Glaciology*, *52*(178), 407–424. https://doi.org/10.3189/172756506781828548

Fujita, S., Maeno, H., Uratsuka, S., Furukawa, T., Mae, S., Fujii, Y., & Watanabe, O. (1999). Nature of radio echo layering in the Antarctic Ice Sheet detected by a two-frequency experiment. *Journal of Geophysical Research: Solid Earth*, *104*(B6), 13013–13024. https://doi.org/10.1029/1999JB900034

Fujita, S., Matsuoka, T., Ishida, T., Matsuoka, K., & Mae, S. (2000). A summary of the complex dielectric permittivity of ice in the megahertz range and its applications for radar sounding of polar ice sheets. *International Symposium on Physics of Ice Core Records, September 14-17, 1998.*, 185–212. http://hdl.handle.net/2115/32469

Fujita, S., Okuyama, J., Hori, A., & Hondoh, T. (2009). Metamorphism of stratified firn at Dome Fuji, Antarctica: A mechanism for local insolation modulation of gas transport conditions during bubble close off. *Journal of Geophysical Research: Earth Surface*, *114*(F3). https://doi.org/10.1029/2008JF001143

Fürst, J. J., Durand, G., Gillet-Chaulet, F., Tavard, L., Rankl, M., Braun, M., & Gagliardini, O. (2016). The safety band of Antarctic ice shelves. *Nature Climate Change*, *6*(5), 479–482. https://doi.org/10.1038/nclimate2912

Gabrieli, J., & Barbante, C. (2014). The Alps in the age of the Anthropocene: The impact of human activities on the cryosphere recorded in the Colle Gnifetti glacier. *Rendiconti Lincei*, *25*(1), 71–83. https://doi.org/10.1007/s12210-014-0292-2

Gagliardini, O., Zwinger, T., Gillet-Chaulet, F., Durand, G., Favier, L., De Fleurian, B., Greve, R., Malinen, M., Martín, C., Råback, P., Ruokolainen, J., Sacchettini, M., Schäfer, M., Seddik, H., & Thies, J. (2013). Capabilities and performance of Elmer/Ice, a new-generation ice sheet model. *Geoscientific Model Development*, *6*(4), 1299–1318. https://doi.org/10.5194/gmd-6-1299-2013

Gerber, T. A., Lilien, D. A., Nymand, N. F., Steinhage, D., Eisen, O., & Dahl-Jensen, D. (2025). Anisotropic scattering in radio-echo sounding: Insights from Northeast Greenland. *The Cryosphere*, *19*(5), 1955–1971. https://doi.org/10.5194/tc-19-1955-2025

Gerber, T. A., Lilien, D. A., Rathmann, N. M., Franke, S., Young, T. J., Valero-Delgado, F., Ershadi, M. R., Drews, R., Zeising, O., Humbert, A., Stoll, N., Weikusat, I., Grinsted, A., Hvidberg, C. S., . . . Eisen, O. (2023). Crystal orientation fabric anisotropy causes directional hardening of the Northeast Greenland Ice Stream. *Nature Communications*, *14*(1), 2653. https://doi.org/10.1038/s41467-023-38139-8

Gillet-Chaulet, F., Gagliardini, O., Meyssonnier, J., Zwinger, T., & Ruokolainen, J. (2006). Flow-induced anisotropy in polar ice and related ice-sheet flow modelling. *Journal of Non-Newtonian Fluid Mechanics*, *134*(1), 33–43. https://doi.org/10.1016/j.jnnfm.2005.11.005

Gillet-Chaulet, F., Hindmarsh, R. C. A., Corr, H. F. J., King, E. C., & Jenkins, A. (2011). *In-Situ* quantification of ice rheology and direct measurement of the Raymond effect at Summit, Greenland using a phase-sensitive radar. *Geophysical Research Letters*, *38*(24), L24503. https://doi.org/10.1029/2011GL049843

Glen, J. W. (1955). The creep of polycrystalline ice. *Proceedings of the Royal Society of London. Series A. Mathematical and Physical Sciences*, *228*(1175), 519–538. https://doi.org/10.1098/rspa.1955.0066

Gogineni, S., Chuah, T., Allen, C., Jezek, K., & Moore, R. K. (1998). An improved coherent radar depth sounder. *Journal of Glaciology*, *44*(148), 659–669. https://doi.org/10.3189/S0022143000002161

Gogineni, S., Tammana, D., Braaten, D., Leuschen, C., Akins, T., Legarsky, J., Kanagaratnam, P., Stiles, J., Allen, C., & Jezek, K. (2001). Coherent radar ice thickness measurements over the Greenland Ice Sheet. *Journal of Geophysical Research: Atmospheres*, *106*(D24), 33761–33772. https://doi.org/10.1029/2001JD900183

Gow, A. J. (1965). On the accumulation and seasonal stratification of snow at the South pole. *Journal of Glaciology*, *5*(40), 467–477. https://doi.org/10.3189/S002214300001844X

Graham, F. S., Morlighem, M., Warner, R. C., & Treverrow, A. (2018). Implementing an empirical scalar constitutive relation for ice with flow-induced polycrystalline anisotropy in large-scale ice sheet models. *The Cryosphere*, *12*(3), 1047–1067. https://doi.org/10.5194/tc-12-1047-2018

Gudmandsen, P. (1969). Airborne radio echo sounding of the Greenland Ice Sheet. *The Geographical Journal*, *135*(4), 548–551. https://doi.org/10.2307/1795099

Gudmandsen, P. (1975). Layer echoes in polar ice sheets. *Journal of Glaciology*, *15*(73), 95–101. https://doi.org/10.3189/S0022143000034304

Hamran, S.-E., & Aarholt, E. (1993). Glacier study using wavenumber domain synthetic aperture radar. *Radio Science*, *28*(4), 559–570. https://doi.org/10.1029/92RS03022

Hansen, T. C. (2021). The everlasting hunt for new ice phases. *Nature Communications*, *12*(1), 3161. https://doi.org/10.1038/s41467-021-23403-6

Hargreaves, N. D. (1978). The radio-frequency birefringence of polar ice. *Journal of Glaciology*, *21*(85), 301–313. https://doi.org/10.3189/S0022143000033499

Hati, A., Nelson, C. W., & Howe, D. A. (2009). Vibration-induced PM and AM noise in microwave components. *IEEE Transactions on Ultrasonics, Ferroelectrics, and Frequency Control*, *56*(10), 2050–2059. https://doi.org/10.1109/TUFFC.2009.1288

Hawkins, J. D. (2023). *Novel techniques for quantifying spatio-temporal changes in polar ice sheets* [Doctoral dissertation, University College London (UCL)]. https://discovery.ucl.ac.uk/id/eprint/10174660/

He, F., & Clark, P. U. (2022). Freshwater forcing of the Atlantic Meridional Overturning Circulation revisited. *Nature Climate Change*, *12*(5), 449–454. https://doi.org/10.1038/s41558-022-01328-2

Heister, A., & Scheiber, R. (2018). Coherent large beamwidth processing of radio-echo sounding data. *The Cryosphere*, *12*(9), 2969–2979. https://doi.org/10.5194/tc-12-2969-2018

Hélière, F., Lin, C.-C., Corr, H., & Vaughan, D. (2007). Radio echo sounding of Pine Island Glacier, West Antarctica: Aperture synthesis processing and analysis of feasibility from space. *IEEE Transactions on Geoscience and Remote Sensing*, *45*(8), 2573–2582. https://doi.org/10.1109/TGRS.2007.897433

Henry, A. C. J. (2024). *Modelling the evolution, rheology, and buttressing of Antarctic pinning points* [Doctoral dissertation, University of Tübingen]. https://doi.org/10.15496/PUBLIKATION-95530

Hills, B. H., Holschuh, N., Hoffman, A. O., Horlings, A. N., Erwin, E., Kirkpatrick, L. R., Fudge, T. J., Steig, E. J., & Christianson, K. (2025a).

Radar-derived crystal orientation fabric suggests dynamic stability at the summit of Hercules Dome. *Journal of Geophysical Research: Earth Surface*, *130*(3), e2023JF007588. https://doi.org/10.1029/2023JF007588

Hills, B. H., Young, T. J., Lilien, D. A., Babcock, E., Bienert, N., Blankenship, D., Bradford, J., Brighi, G., Brisbourne, A., Dall, J., Drews, R., Eisen, O., Ershadi, M. R., Gerber, T. A., . . . Zeising, O. (2025b). Radar polarimetry in glaciology: Theory, measurement techniques, and scientific applications for investigating the anisotropy of ice masses. *Reviews of Geophysics*, *63*(4), e2024RG000842. https://doi.org/10.1029/2024RG000842

Hoelzle, M., Darms, G., Lüthi, M. P., & Suter, S. (2011). Evidence of accelerated englacial warming in the Monte Rosa area, Switzerland/Italy. *The Cryosphere*, *5*(1), 231–243. https://doi.org/10.5194/tc-5-231-2011

Hoffmann, H., Preunkert, S., Legrand, M., Leinfelder, D., Bohleber, P., Friedrich, R., & Wagenbach, D. (2018). A new sample preparation system for micro-^{14}C dating of glacier ice with a first application to a high Alpine ice core from Colle Gnifetti (Switzerland). *Radiocarbon*, *60*(2), 517–533. https://doi.org/10.1017/RDC.2017.99

Holschuh, N., Christianson, K., Paden, J., Alley, R. B., & Anandakrishnan, S. (2020). Linking postglacial landscapes to glacier dynamics using swath radar at Thwaites Glacier, Antarctica. *Geology*, *48*(3), 268–272. https://doi.org/10.1130/G46772.1

Holschuh, N., Christianson, K., & Anandakrishnan, S. (2014). Power loss in dipping internal reflectors, imaged using ice-penetrating radar. *Annals of Glaciology*, *55*(67), 49–56. https://doi.org/10.3189/2014AoG67A005

Holschuh, N., Christianson, K., Conway, H., Jacobel, R. W., & Welch, B. C. (2018). Persistent tracers of historic ice flow in glacial stratigraphy near Kamb Ice Stream, West Antarctica. *The Cryosphere*, *12*(9), 2821–2829. https://doi.org/10.5194/tc-12-2821-2018

Holschuh, N., Parizek, B. R., Alley, R. B., & Anandakrishnan, S. (2017). Decoding ice sheet behavior using englacial layer slopes. *Geophysical Research Letters*, *44*(11), 5561–5570. https://doi.org/10.1002/2017GL073417

Hopwood, M. J., Carroll, D., Dunse, T., Hodson, A., Holding, J. M., Iriarte, J. L., Ribeiro, S., Achterberg, E. P., Cantoni, C., Carlson, D. F., Chierici, M., Clarke, J. S., Cozzi, S., Fransson, A., . . . Meire, L. (2020). Review article: How does glacier discharge affect marine biogeochemistry and primary production in the Arctic? *The Cryosphere*, *14*(4), 1347–1383. https://doi.org/10.5194/tc-14-1347-2020

Hörhold, M. W., Albert, M. R., & Freitag, J. (2009). The impact of accumulation rate on anisotropy and air permeability of polar firn at a high-accumulation site. *Journal of Glaciology*, *55*(192), 625–630. https://doi.org/10.3189/002214309789471021

Hörhold, M. W., Laepple, T., Freitag, J., Bigler, M., Fischer, H., & Kipfstuhl, S. (2012). On the impact of impurities on the densification of polar firn. *Earth and Planetary Science Letters*, *325–326*, 93–99. https://doi.org/10.1016/j.epsl.2011.12.022

Hudleston, P. J. (2015). Structures and fabrics in glacial ice: A review. *Journal of Structural Geology*, *81*, 1–27. https://doi.org/10.1016/j.jsg.2015.09.003

Hugonnet, R., McNabb, R., Berthier, E., Menounos, B., Nuth, C., Girod, L., Farinotti, D., Huss, M., Dussaillant, I., Brun, F., & Kääb, A. (2021). Accelerated global glacier mass loss in the early twenty-first century. *Nature*, *592*(7856), 726–731. https://doi.org/10.1038/s41586-021-03436-z

Humbert, A., Greve, R., & Hutter, K. (2005). Parameter sensitivity studies for the ice flow of the Ross Ice Shelf, Antarctica. *Journal of Geophysical Research: Earth Surface*, *110*(F4). https://doi.org/10.1029/2004JF000170

Huss, M., & Hock, R. (2015). A new model for global glacier change and sea-level rise. *Frontiers in Earth Science*, *3*. https://doi.org/10.3389/feart.2015.00054

Hutterli, M. A., Schneebeli, M., Freitag, J., Kipfstuhl, J., & Röthlisberger, R. (2009). Impact of local insolation on snow metamorphism and ice core records. *Low Temperature Science*, *68*, 223–232. http://hdl.handle.net/2115/45450

Immerzeel, W. W., Lutz, A. F., Andrade, M., Bahl, A., Biemans, H., Bolch, T., Hyde, S., Brumby, S., Davies, B. J., Elmore, A. C., Emmer, A., Feng, M., Fernández, A., Haritashya, U., … Baillie, J. E. M. (2020). Importance and vulnerability of the world's water towers. *Nature*, *577*(7790), 364–369. https://doi.org/10.1038/s41586-019-1822-y

Inoue, R., Fujita, S., Kawamura, K., Oyabu, I., Nakazawa, F., Motoyama, H., & Aoki, T. (2024). Spatial distribution of vertical density and microstructure profiles in near-surface firn around Dome Fuji, Antarctica. *The Cryosphere*, *18*(1), 425–449. https://doi.org/10.5194/tc-18-425-2024

IPCC. (2022). *The ocean and cryosphere in a changing climate: Special report of the Intergovernmental Panel on Climate Change* (1st ed.). Cambridge University Press. https://doi.org/10.1017/9781009157964

Jacobel, R. W., & Welch, B. C. (2005). A time marker at 17.5 kyr BP detected throughout West Antarctica. *Annals of Glaciology*, *41*, 47–51. https://doi.org/10.3189/172756405781813348

Jansen, D., Franke, S., Bauer, C. C., Binder, T., Dahl-Jensen, D., Eichler, J., Eisen, O., Hu, Y., Kerch, J., Llorens, M.-G., Miller, H., Neckel, N., Paden, J., de Riese, T., … Bons, P. D. (2024). Shear margins in upper half of Northeast Greenland Ice Stream were established two millennia ago. *Nature Communications*, *15*(1), 1193. https://doi.org/10.1038/s41467-024-45021-8

Jenk, T. M., Szidat, S., Bolius, D., Sigl, M., Gäggeler, H. W., Wacker, L., Ruff, M., Barbante, C., Boutron, C. F., & Schwikowski, M. (2009). A novel radiocarbon dating technique applied to an ice core from the Alps indicating late Pleistocene ages. *Journal of Geophysical Research: Atmospheres*, *114*(D14), 2009JD011860. https://doi.org/10.1029/2009JD011860

Jenkins, A., Corr, H. F. J., Nicholls, K. W., Stewart, C. L., & Doake, C. S. M. (2006). Interactions between ice and ocean observed with phase-sensitive radar near an Antarctic ice-shelf grounding line. *Journal of Glaciology*, *52*(178), 325–346. https://doi.org/10.3189/172756506781828502

Jennings, S. J. A., & Hambrey, M. J. (2021). Structures and deformation in glaciers and ice sheets. *Reviews of Geophysics*, *59*(3), e2021RG000743. https://doi.org/10.1029/2021RG000743

Jordan, T. M., Besson, D. Z., Kravchenko, I., Latif, U., Madison, B., Nokikov, A., & Shultz, A. (2020a). Modeling ice birefringence and oblique radio wave propagation for neutrino detection at the South Pole. *Annals of Glaciology*, *61*(81), 84–91. https://doi.org/10.1017/aog.2020.18

Jordan, T. M., Martín, C., Brisbourne, A. M., Schroeder, D. M., & Smith, A. M. (2022). Radar characterization of ice crystal orientation fabric and anisotropic viscosity within an Antarctic ice stream. *Journal of Geophysical Research: Earth Surface*, *127*(6), e2022JF006673. https://doi.org/10.1029/2022JF006673

Jordan, T. M., Schroeder, D. M., Castelletti, D., Li, J., & Dall, J. (2019). A polarimetric coherence method to determine ice crystal orientation fabric from radar sounding: Application to the NEEM ice core region. *IEEE Transactions on Geoscience and Remote Sensing*, *57*(11), 8641–8657. https://doi.org/10.1109/TGRS.2019.2921980

Jordan, T. M., Schroeder, D. M., Elsworth, C. W., & Siegfried, M. R. (2020b). Estimation of ice fabric within Whillans Ice Stream using polarimetric phase-sensitive radar sounding. *Annals of Glaciology*, *61*(81), 74–83. https://doi.org/10.1017/aog.2020.6

Kapai, S., Schroeder, D., Broome, A., Young, T. J., & Stewart, C. (2022). SAR focusing of mobile ApRES surveys. *2022 IEEE International Geoscience and Remote Sensing Symposium (IGARSS)*, 1688–1691. https://doi.org/10.1109/IGARSS46834.2022.9883784

Karlsson, N. B., Dahl-Jensen, D., Gogineni, S. P., & Paden, J. D. (2013). Tracing the depth of the Holocene ice in North Greenland from radio-echo sounding data. *Annals of Glaciology*, *54*(64), 44–50. https://doi.org/10.3189/2013AoG64A057

Karlsson, N. B., Razik, S., Hörhold, M., Winter, A., Steinhage, D., Binder, T., & Eisen, O. (2020). Surface accumulation in Northern Central Greenland during the last 300 years. *Annals of Glaciology*, *61*(81), 214–224. https://doi.org/10.1017/aog.2020.30

Keegan, K. M., Albert, M. R., McConnell, J. R., & Baker, I. (2019). Climate effects on firn permeability are preserved within a firn column. *Journal of Geophysical Research: Earth Surface*, *124*(3), 830–837. https://doi.org/10.1029/2018JF004798

Kerch, J. K. (2016). *Crystal-orientation fabric variations on the cm-scale in cold Alpine ice: Interaction with paleo-climate proxies under deformation and implications for the interpretation of seismic velocities* [Doctoral dissertation, Heidelberg University]. https://doi.org/10.11588/heidok.00022326

Kingslake, J., Hindmarsh, R. C. A., Aðalgeirsdóttir, G., Conway, H., Corr, H. F. J., Gillet-Chaulet, F., Martín, C., King, E. C., Mulvaney, R., & Pritchard, H. D. (2014). Full-depth englacial vertical ice sheet velocities measured using phase-sensitive radar: Measuring englacial ice velocities. *Journal of Geophysical Research: Earth Surface*, *119*(12), 2604–2618. https://doi.org/10.1002/2014JF003275

Kingslake, J., Martín, C., Arthern, R. J., Corr, H. F. J., & King, E. C. (2016). Ice-flow reorganization in West Antarctica 2.5 kyr ago dated using radar-derived englacial flow velocities. *Geophysical Research Letters*, *43*(17), 9103–9112. https://doi.org/10.1002/2016GL070278

Koch, I., Drews, R., Franke, S., Jansen, D., Oraschewski, F. M., Muhle, L. S., Višnjević, V., Matsuoka, K., Pattyn, F., & Eisen, O. (2023). Radar internal reflection horizons from multisystem data reflect ice dynamic and surface accumulation history along the Princess Ragnhild Coast, Dronning Maud Land, East Antarctica. *Journal of Glaciology*, 1–19. https://doi.org/10.1017/jog.2023.93

Konrad, H., Bohleber, P., Wagenbach, D., Vincent, C., & Eisen, O. (2013). Determining the age distribution of Colle Gnifetti, Monte Rosa, Swiss Alps, by combining ice cores, ground-penetrating radar and a simple flow model. *Journal of Glaciology*, *59*(213), 179–189. https://doi.org/10.3189/2013JoG12J072

Koutnik, M. R., Fudge, T. J., Conway, H., Waddington, E. D., Neumann, T. A., Cuffey, K. M., Buizert, C., & Taylor, K. C. (2016). Holocene accumulation and ice flow near the West Antarctic Ice Sheet Divide ice core site. *Journal of Geophysical Research: Earth Surface*, *121*(5), 907–924. https://doi.org/10.1002/2015JF003668

Kovacs, A., Gow, A. J., & Morey, R. M. (1995). The in-situ dielectric constant of polar firn revisited. *Cold Regions Science and Technology*, *23*(3), 245–256. https://doi.org/10.1016/0165-232X(94)00016-Q

Kufner, S.-K., Wookey, J., Brisbourne, A. M., Martín, C., Hudson, T. S., Kendall, J. M., & Smith, A. M. (2023). Strongly depth-dependent ice fabric in a fast-flowing Antarctic ice stream revealed with icequake observations. *Journal of Geophysical Research: Earth Surface*, *128*(3), e2022JF006853. https://doi.org/10.1029/2022JF006853

Kusk, A., & Dall, J. (2010). SAR focusing of P-band ice sounding data using back-projection. *2010 IEEE International Geoscience and Remote Sensing Symposium (IGARSS)*, 4071–4074. https://doi.org/10.1109/IGARSS.2010.5651038

Larour, E., Seroussi, H., Morlighem, M., & Rignot, E. (2012). Continental scale, high order, high spatial resolution, ice sheet modeling using the Ice Sheet System Model (ISSM). *Journal of Geophysical Research: Earth Surface*, *117*(F1), 2011JF002140. https://doi.org/10.1029/2011JF002140

Legarsky, J. J., Gogineni, S. P., & Akins, T. L. (2001). Focused synthetic aperture radar processing of ice-sounder data collected over the Greenland Ice Sheet. *IEEE Transactions on Geoscience and Remote Sensing*, *39*(10), 2109–2117. https://doi.org/10.1109/36.957274

Leuschen, C., Gogineni, S., & Tammana, D. (2000). SAR processing of radar echo sounder data. *2000 IEEE International Geoscience and Remote Sensing Symposium (IGARSS)*, *6*, 2570–2572. https://doi.org/10.1109/IGARSS.2000.859643

Leuschen, C., & Plumb, R. (2000). A matched-filter approach to wave migration. *Journal of Applied Geophysics*, *43*(2–4), 271–280. https://doi.org/10.1016/S0926-9851(99)00064-6

Leysinger Vieli, G. J.-M. C., Martín, C., Hindmarsh, R. C. A., & Lüthi, M. P. (2018). Basal freeze-on generates complex ice-sheet stratigraphy. *Nature Communications*, *9*(1), 4669. https://doi.org/10.1038/s41467-018-07083-3

Li, J., Vélez González, J. A., Leuschen, C., Harish, A., Gogineni, P., Montagnat, M., Weikusat, I., Rodriguez-Morales, F., & Paden, J. (2018). Multi-channel and multi-polarization radar measurements around the NEEM site. *The Cryosphere*, *12*(8), 2689–2705. https://doi.org/10.5194/tc-12-2689-2018

Licciulli, C., Bohleber, P., Lier, J., Gagliardini, O., Hoelzle, M., & Eisen, O. (2020). A full Stokes ice-flow model to assist the interpretation of millennial-scale ice cores at the high-Alpine drilling site Colle Gnifetti, Swiss/Italian Alps. *Journal of Glaciology*, *66*(255), 35–48. https://doi.org/10.1017/jog.2019.82

Lilien, D. A., Rathmann, N. M., Hvidberg, C. S., & Dahl-Jensen, D. (2021a). Modeling ice-crystal fabric as a proxy for ice-stream stability. *Journal of Geophysical Research: Earth Surface*, *126*(9), e2021JF006306. https://doi.org/10.1029/2021JF006306

Lilien, D. A., Rathmann, N. M., Hvidberg, C. S., Grinsted, A., Ershadi, M. R., Drews, R., & Dahl-Jensen, D. (2023). Simulating higher-order fabric structure in a coupled, anisotropic ice-flow model: Application to Dome C. *Journal of Glaciology*, 1–20. https://doi.org/10.1017/jog.2023.78

Lilien, D. A., Steinhage, D., Taylor, D., Parrenin, F., Ritz, C., Mulvaney, R., Martín, C., Yan, J.-B., O'Neill, C., Frezzotti, M., Miller, H., Gogineni, P., Dahl-Jensen, D., & Eisen, O. (2021b). Brief communication: New radar constraints support presence of ice older than 1.5 Myr at Little Dome C. *The Cryosphere*, *15*(4), 1881–1888. https://doi.org/10.5194/tc-15-1881-2021

Lindbäck, K., Moholdt, G., Nicholls, K. W., Hattermann, T., Pratap, B., Thamban, M., & Matsuoka, K. (2019). Spatial and temporal variations in basal melting at Nivlisen ice shelf, East Antarctica, derived from phase-sensitive radars. *The Cryosphere*, *13*(10), 2579–2595. https://doi.org/10.5194/tc-13-2579-2019

Llorens, M.-G., Griera, A., Bons, P. D., Weikusat, I., Prior, D. J., Gomez-Rivas, E., De Riese, T., Jimenez-Munt, I., García-Castellanos, D., & Lebensohn, R. A. (2022). Can changes in deformation regimes be inferred from crystallographic preferred orientations in polar ice? *The Cryosphere*, *16*(5), 2009–2024. https://doi.org/10.5194/tc-16-2009-2022

Lomonaco, R., Albert, M., & Baker, I. (2011). Microstructural evolution of fine-grained layers through the firn column at Summit, Greenland. *Journal of Glaciology*, *57*(204), 755–762. https://doi.org/10.3189/002214311797409730

Looyenga, H. (1965). Dielectric constants of heterogeneous mixtures. *Physica*, *31*(3), 401–406. https://doi.org/10.1016/0031-8914(65)90045-5

Lüthi, M., & Funk, M. (2000). Dating ice cores from a high Alpine glacier with a flow model for cold firn. *Annals of Glaciology*, *31*, 69–79. https://doi.org/10.3189/172756400781820381

Lutz, F., Eccles, J., Prior, D. J., Craw, L., Fan, S., Hulbe, C., Forbes, M., Still, H., Pyne, A., & Mandeno, D. (2020). Constraining ice shelf anisotropy using shear wave splitting measurements from active-source borehole seismics. *Journal of Geophysical Research: Earth Surface*, *125*(9), e2020JF005707. https://doi.org/10.1029/2020JF005707

Lytle, V. I., & Jezek, K. C. (1994). Dielectric permittivity and scattering measurements of Greenland firn at 26.5-40 GHz. *IEEE Transactions on Geoscience and Remote Sensing*, *32*(2), 290–295. https://doi.org/10.1109/36.295044

Ma, Y., Gagliardini, O., Ritz, C., Gillet-Chaulet, F., Durand, G., & Montagnat, M. (2010). Enhancement factors for grounded ice and ice shelves inferred from an anisotropic ice-flow model. *Journal of Glaciology*, *56*(199), 805–812. https://doi.org/10.3189/002214310794457209

MacGregor, J. A., Fahnestock, M. A., Catania, G. A., Paden, J. D., Prasad Gogineni, S., Young, S. K., Rybarski, S. C., Mabrey, A. N., Wagman, B. M., & Morlighem, M. (2015). Radiostratigraphy and age structure of the Greenland Ice Sheet. *Journal of Geophysical Research: Earth Surface*, *120*(2), 212–241. https://doi.org/10.1002/2014JF003215

Maeno, N., & Ebinuma, T. (1983). Pressure sintering of ice and its implication to the densification of snow at polar glaciers and ice sheets. *The Journal of Physical Chemistry*, *87*(21), 4103–4110. https://doi.org/10.1021/j100244a023

Marsh, O. J., Fricker, H. A., Siegfried, M. R., Christianson, K., Nicholls, K. W., Corr, H. F. J., & Catania, G. (2016). High basal melting forming a channel at the grounding line of Ross Ice Shelf, Antarctica. *Geophysical Research Letters*, *43*(1), 250–255. https://doi.org/10.1002/2015GL066612

Martín, C., & Gudmundsson, G. H. (2012). Effects of nonlinear rheology, temperature and anisotropy on the relationship between age and depth at ice divides. *The Cryosphere*, *6*(5), 1221–1229. https://doi.org/10.5194/tc-6-1221-2012

Martín, C., Hindmarsh, R. C. A., & Navarro, F. J. (2009). On the effects of divide migration, along-ridge flow, and basal sliding on isochrones near an ice divide. *Journal of Geophysical Research*, *114*(F2). https://doi.org/10.1029/2008JF001025

Matsuoka, K., Power, D., Fujita, S., & Raymond, C. F. (2012). Rapid development of anisotropic ice-crystal-alignment fabrics inferred from englacial radar polarimetry, central West Antarctica. *Journal of Geophysical Research: Earth Surface*, *117*(F3), 2012JF002440. https://doi.org/10.1029/2012JF002440

Matsuoka, K., Wilen, L., Hurley, S. P., & Raymond, C. F. (2009). Effects of birefringence within ice sheets on obliquely propagating radio waves. *IEEE Transactions on Geoscience and Remote Sensing*, *47*(5), 1429–1443. https://doi.org/10.1109/TGRS.2008.2005201

Matsuoka, T., Fujita, S., Morishima, S., & Mae, S. (1997). Precise measurement of dielectric anisotropy in ice Ih at 39 GHz. *Journal of Applied Physics*, *81*(5), 2344–2348. https://doi.org/10.1063/1.364238

McCormack, F. S., Warner, R. C., Seroussi, H., Dow, C. F., Roberts, J. L., & Treverrow, A. (2022). Modeling the deformation regime of Thwaites Glacier, West Antarctica, using a simple flow relation for ice anisotropy (ESTAR). *Journal of Geophysical Research: Earth Surface*, *127*(3), e2021JF006332. https://doi.org/10.1029/2021JF006332

Medley, B., Ligtenberg, S. R. M., Joughin, I., Van Den Broeke, M. R., Gogineni, S., & Nowicki, S. (2015). Antarctic firn compaction rates from repeat-track airborne radar data: I. Methods. *Annals of Glaciology*, *56*(70), 155–166. https://doi.org/10.3189/2015AoG70A203

Millan, R., Jager, E., Mouginot, J., Wood, M. H., Larsen, S. H., Mathiot, P., Jourdain, N. C., & Bjørk, A. (2023). Rapid disintegration and weakening of ice shelves in North Greenland. *Nature Communications*, *14*(1), 6914. https://doi.org/10.1038/s41467-023-42198-2

Millstein, J. D., Minchew, B. M., & Pegler, S. S. (2022). Ice viscosity is more sensitive to stress than commonly assumed. *Communications Earth & Environment*, *3*(1), 57. https://doi.org/10.1038/s43247-022-00385-x

Minchew, B. M., Meyer, C. R., Robel, A. A., Gudmundsson, G. H., & Simons, M. (2018). Processes controlling the downstream evolution of ice rheology in glacier shear margins: Case study on Rutford Ice Stream, West Antarctica. *Journal of Glaciology*, *64*(246), 583–594. https://doi.org/10.1017/jog.2018.47

Mojtabavi, S., Wilhelms, F., Cook, E., Davies, S. M., Sinnl, G., Skov Jensen, M., Dahl-Jensen, D., Svensson, A., Vinther, B. M., Kipfstuhl, S., Jones, G., Karlsson, N. B., Faria, S. H., Gkinis, V., . . . Rasmussen, S. O. (2020). A first chronology for the East Greenland Ice-core Project (EGRIP) over the Holocene and last glacial termination. *Climate of the Past*, *16*(6), 2359–2380. https://doi.org/10.5194/cp-16-2359-2020

Montagnat, M., Chauve, T., Barou, F., Tommasi, A., Beausir, B., & Fressengeas, C. (2015). Analysis of dynamic recrystallization of ice from EBSD orientation mapping. *Frontiers in Earth Science*, *3*. https://doi.org/10.3389/feart.2015.00081

Moore, J. C. (1988). Dielectric variability of a 130 m Antarctic ice core: Implications for radar sounding. *Annals of Glaciology*, *11*, 95–99. https://doi.org/10.3189/S026030550000639X

Moran, M. L., Greenfield, R. J., Arcone, S. A., & Delaney, A. J. (2000). Delineation of a complexly dipping temperate glacier bed using short-pulse radar arrays. *Journal of Glaciology*, *46*(153), 274–286. https://doi.org/10.3189/172756500781832882

Moss, G., Višnjević, V., Eisen, O., Oraschewski, F. M., Schröder, C., Macke, J. H., & Drews, R. (2025). Simulation-based inference of surface accumulation and basal melt rates of an Antarctic ice shelf from isochronal layers. *Journal of Glaciology*, *71*, e44. https://doi.org/10.1017/jog.2025.13

NASA Shuttle Radar Topography Mission. (2013). *Shuttle Radar Topography Mission (SRTM) Global*. [dataset]. OpenTopography. https://doi.org/10.5069/G9445JDF

Navarro, P., & Eisen, O. (2009). Ground-penetrating radar in glaciological applications. In P. Pellikka & W. G. Rees (Eds.), *Remote Sensing of Glaciers* (pp. 221–256). CRC Press. https://doi.org/10.1201/b10155-17

NEEM community members. (2013). Eemian interglacial reconstructed from a Greenland folded ice core. *Nature*, *493*(7433), 489–494. https://doi.org/10.1038/nature11789

Ng, F., & King, E. C. (2011). Kinematic waves in polar firn stratigraphy. *Journal of Glaciology*, *57*(206), 1119–1134. https://doi.org/10.3189/002214311798843340

Nicholls, K. W., Corr, H. F. J., Stewart, C. L., Lok, L. B., Brennan, P. V., & Vaughan, D. G. (2015). A ground-based radar for measuring vertical strain rates and time-varying basal melt rates in ice sheets and shelves. *Journal of Glaciology*, *61*(230), 1079–1087. https://doi.org/10.3189/2015JoG15J073

Nye, J. F., Berry, M. V., & Walford, M. E. R. (1972). Measuring the change in thickness of the Antarctic Ice Sheet. *Nature Physical Science*, *240*(97), 7–9. https://doi.org/10.1038/physci240007a0

Oksman, M., Kvorning, A. B., Larsen, S. H., Kjeldsen, K. K., Mankoff, K. D., Colgan, W., Andersen, T. J., Nørgaard-Pedersen, N., Seidenkrantz, M.-S., Mikkelsen, N., & Ribeiro, S. (2022). Impact of freshwater runoff from the southwest Greenland Ice Sheet on fjord productivity since the late 19th century. *The Cryosphere*, *16*(6), 2471–2491. https://doi.org/10.5194/tc-16-2471-2022

Oraschewski, F. M. (2024a). *Oraschewski/pRocESsor: pRocESsor – for layer-optimized SAR processing of mobile pRES profiles* (Version v1.0). [software]. Zenodo. https://doi.org/10.5281/ZENODO.12656458

Oraschewski, F. M. (2024b). Phase-sensitive radar measurements of glacial processes. *Nature Reviews Earth & Environment*, *5*(7), 485–485. https://doi.org/10.1038/s43017-024-00571-9

Oraschewski, F. M., Ershadi, M. R., & Drews, R. (2025a). *Oraschewski/Oraschewski_etal_2025_GRL_PolarimetricCMPs: Forward modeling and inversion of polarimetric CMP data acquired with a phase-sensitive radar* (Version v1.0). [software]. Zenodo. https://doi.org/10.5281/ZENODO.15683530

Oraschewski, F. M., Ershadi, M. R., & Drews, R. (2025b). *Polarimetric wide-angle common midpoint pRES survey near central front of Ekström Ice Shelf, East Antarctica.* [dataset]. PANGAEA. https://doi.org/10.1594/PANGAEA.974475

Oraschewski, F. M., Ershadi, M. R., & Drews, R. (2025c). Polarimetric wide-angle radar detects competing signatures of ice fabric and structural firn anisotropy. *Geophysical Research Letters*, *52*(14), e2024GL113096. https://doi.org/10.1029/2024GL113096

Oraschewski, F. M., & Grinsted, A. (2022). Modeling enhanced firn densification due to strain softening. *The Cryosphere*, *16*(7), 2683–2700. https://doi.org/10.5194/tc-16-2683-2022

Oraschewski, F. M., Koch, I., Ershadi, M. R., Hawkins, J., Eisen, O., & Drews, R. (2024a). *Mobile phase-sensitive radio echo sounder (pRES) profiling data of deep radiostratigraphy of Colle Gnifetti (Swiss–Italian Alps), 2021.* [dataset]. PANGAEA. https://doi.org/10.1594/PANGAEA.965194

Oraschewski, F. M., Koch, I., Ershadi, M. R., Hawkins, J., Eisen, O., & Drews, R. (2024b). *Raw data of mobile phase-sensitive radio echo sounder (pRES) profiling data of deep radiostratigraphy of Colle Gnifetti (Swiss–Italian Alps), 2021.* [dataset]. PANGAEA. https://doi.org/10.1594/PANGAEA.965199

Oraschewski, F. M., Koch, I., Ershadi, M. R., Hawkins, J. D., Eisen, O., & Drews, R. (2024c). Layer-optimized synthetic aperture radar processing with a mobile phase-sensitive radar: A proof of concept for detecting the deep englacial stratigraphy of Colle Gnifetti, Switzerland and Italy. *The Cryosphere*, *18*(8), 3875–3889. https://doi.org/10.5194/tc-18-3875-2024

Paden, J. (2006). *Synthetic aperture radar for imaging the basal conditions of the polar ice sheets* [Doctoral dissertation, University of Kansas]. https://web.archive.org/web/20170808175054id_/https://people.cresis.ku.edu/~paden/padenDissertation.pdf

Parrella, G., Hajnsek, I., & Papathanassiou, K. P. (2021). Retrieval of firn thickness by means of polarisation phase differences in L-band SAR data. *Remote Sensing*, *13*(21), 4448. https://doi.org/10.3390/rs13214448

Peters, M. E., Blankenship, D. D., Carter, S. P., Kempf, S. D., Young, D. A., & Holt, J. W. (2007). Along-track focusing of airborne radar sounding data from West Antarctica for improving basal reflection analysis and layer detection. *IEEE Transactions on Geoscience and Remote*

Sensing, *45*(9), 2725–2736. https://doi.org/10.1109/TGRS.2007.897416

Peters, M. E., Blankenship, D. D., & Morse, D. L. (2005). Analysis techniques for coherent airborne radar sounding: Application to West Antarctic ice streams. *Journal of Geophysical Research: Solid Earth*, *110*(B6), 2004JB003222. https://doi.org/10.1029/2004JB003222

Pfeffer, W. T., & Mrugala, R. (2002). Temperature gradient and initial snow density as controlling factors in the formation and structure of hard depth hoar. *Journal of Glaciology*, *48*(163), 485–494. https://doi.org/10.3189/172756502781831098

Pickell, D. J., & Hawley, R. L. (2024). Performance characterization of a new, low-cost multi-GNSS instrument for the cryosphere. *Journal of Glaciology*, 1–7. https://doi.org/10.1017/jog.2023.97

Pollard, D., & DeConto, R. M. (2012). Description of a hybrid ice sheet-shelf model, and application to Antarctica. *Geoscientific Model Development*, *5*(5), 1273–1295. https://doi.org/10.5194/gmd-5-1273-2012

Preunkert, S., Wagenbach, D., & Legrand, M. (2003). A seasonally resolved Alpine ice core record of nitrate: Comparison with anthropogenic inventories and estimation of preindustrial emissions of NO in Europe. *Journal of Geophysical Research: Atmospheres*, *108*(D21), 2003JD00–3475. https://doi.org/10.1029/2003JD003475

Raju, G., Xin, W., & Moore, R. K. (1990). Design, development, field observations, and preliminary results of the Coherent Antarctic Radar Depth Sounder (CARDS) of the University of Kansas, U.S.A. *Journal of Glaciology*, *36*(123), 247–254. https://doi.org/10.3189/S0022143000009503

Ranganathan, M., Minchew, B., Meyer, C. R., & Peč, M. (2021). Recrystallization of ice enhances the creep and vulnerability to fracture of ice shelves. *Earth and Planetary Science Letters*, *576*, 117219. https://doi.org/10.1016/j.epsl.2021.117219

Rasmussen, S. O., Abbott, P. M., Blunier, T., Bourne, A. J., Brook, E., Buchardt, S. L., Buizert, C., Chappellaz, J., Clausen, H. B., Cook, E., Dahl-Jensen, D., Davies, S. M., Guillevic, M., Kipfstuhl, S., . . . Winstrup, M. (2013). A first chronology for the North Greenland Eemian Ice Drilling (NEEM) ice core. *Climate of the Past*, *9*(6), 2713–2730. https://doi.org/10.5194/cp-9-2713-2013

Rathmann, N. M., Hvidberg, C. S., Grinsted, A., Lilien, D. A., & Dahl-Jensen, D. (2021). Effect of an orientation-dependent non-linear grain fluidity on bulk directional enhancement factors. *Journal of Glaciology*, *67*(263), 569–575. https://doi.org/10.1017/jog.2020.117

Rathmann, N. M., Lilien, D. A., Grinsted, A., Gerber, T. A., Young, T. J., & Dahl-Jensen, D. (2022). On the limitations of using polarimetric radar sounding to infer the crystal orientation fabric of ice masses. *Geophysical Research Letters*, *49*(1), e2021GL096244. https://doi.org/10.1029/2021GL096244

Reese, R., Garbe, J., Hill, E. A., Urruty, B., Naughten, K. A., Gagliardini, O., Durand, G., Gillet-Chaulet, F., Gudmundsson, G. H., Chandler, D., Langebroek, P. M., & Winkelmann, R. (2023). The stability of present-day Antarctic grounding lines – Part 2: Onset of irreversible retreat of Amundsen Sea glaciers under current climate on centennial timescales cannot be excluded. *The Cryosphere*, *17*(9), 3761–3783. https://doi.org/10.5194/tc-17-3761-2023

Reese, R., Gudmundsson, G. H., Levermann, A., & Winkelmann, R. (2018). The far reach of ice-shelf thinning in Antarctica. *Nature Climate Change*, *8*(1), 53–57. https://doi.org/10.1038/s41558-017-0020-x

Richards, D. H., Pegler, S. S., Piazolo, S., & Harlen, O. G. (2021). The evolution of ice fabrics: A continuum modelling approach validated against laboratory experiments. *Earth and Planetary Science Letters*, *556*, 116718. https://doi.org/10.1016/j.epsl.2020.116718

Richards, D. H., Pegler, S. S., Piazolo, S., Stoll, N., & Weikusat, I. (2023). Bridging the gap between experimental and natural fabrics: Modeling ice stream fabric evolution and its comparison with ice-core data. *Journal of Geophysical Research: Solid Earth*, *128*(11), e2023JB027245. https://doi.org/10.1029/2023JB027245

Rignot, E., Mouginot, J., Scheuchl, B., van den Broeke, M., van Wessem, M. J., & Morlighem, M. (2019). Four decades of Antarctic Ice Sheet mass balance from 1979–2017. *Proceedings of the National Academy of Sciences*, *116*(4), 1095–1103. https://doi.org/10.1073/pnas.1812883116

Robin, G. d. Q. (1975). Radio-echo sounding: Glaciological interpretations and applications. *Journal of Glaciology*, *15*(73), 49–64. https://doi.org/10.3189/S0022143000034262

Rodriguez-Morales, F., Byers, K., Crowe, R., Player, K., Hale, R. D., Arnold, E. J., Smith, L., Gifford, C. M., Braaten, D., Panton, C., Gogineni, S., Leuschen, C. J., Paden, J. D., Li, J., . . . Patel, A. (2014). Advanced multifrequency radar instrumentation for polar research. *IEEE Transactions on Geoscience and Remote Sensing*, *52*(5), 2824–2842. https://doi.org/10.1109/TGRS.2013.2266415

Ross, N., Corr, H., & Siegert, M. (2020). Large-scale englacial folding and deep-ice stratigraphy within the West Antarctic Ice Sheet. *The Cryosphere*, *14*(6), 2103–2114. https://doi.org/10.5194/tc-14-2103-2020

Rounce, D. R., Hock, R., Maussion, F., Hugonnet, R., Kochtitzky, W., Huss, M., Berthier, E., Brinkerhoff, D., Compagno, L., Copland, L., Farinotti, D., Menounos, B., & McNabb, R. W. (2023). Global glacier change in the 21st century: Every increase in temperature matters. *Science*, *379*(6627), 78–83. https://doi.org/10.1126/science.abo1324

Rutishauser, A., Scanlan, K. M., Vandecrux, B., Karlsson, N. B., Jullien, N., Ahlstrøm, A. P., Fausto, R. S., & How, P. (2024). Mapping the vertical heterogeneity of Greenland's firn from 2011–2019 using airborne radar and laser altimetry. *The Cryosphere*, *18*(5), 2455–2472. https://doi.org/10.5194/tc-18-2455-2024

Scanlan, K. M., Rutishauser, A., Young, D. A., & Blankenship, D. D. (2020). Interferometric discrimination of cross-track bed clutter in ice-penetrating radar sounding data. *Annals of Glaciology*, *61*(81), 68–73. https://doi.org/10.1017/aog.2020.20

Schannwell, C., Murray, T., Kulessa, B., Gusmeroli, A., Saintenoy, A., & Jansson, P. (2014). An automatic approach to delineate the cold–temperate transition surface with ground-penetrating radar on polythermal glaciers. *Annals of Glaciology*, *55*(67), 89–96. https://doi.org/10.3189/2014AoG67A102

Schlegel, R., Kulessa, B., Murray, T., & Eisen, O. (2022). Towards a common terminology in radioglaciology. *Annals of Glaciology*, *63*(87–89), 8–12. https://doi.org/10.1017/aog.2023.2

Schroeder, D. M., Bingham, R. G., Blankenship, D. D., Christianson, K., Eisen, O., Flowers, G. E., Karlsson, N. B., Koutnik, M. R., Paden, J. D., & Siegert, M. J. (2020). Five decades of radioglaciology. *Annals of Glaciology*, *61*(81), 1–13. https://doi.org/10.1017/aog.2020.11

Schroeder, D. M., Castelletti, D., & Pena, I. (2019). Revisting the limits of azimuth processing gain for radar sounding. *2019 IEEE International Geoscience and Remote Sensing Symposium (IGARSS)*, 994–996. https://doi.org/10.1109/IGARSS.2019.8898737

Schultz, T., Müller, R., Gross, D., & Humbert, A. (2022). On the contribution of grain boundary sliding type creep to firn densification – an assessment using an optimization approach. *The Cryosphere*, *16*(1), 143–158. https://doi.org/10.5194/tc-16-143-2022

Schwikowski, M., Doscher, A., Gaggeler, H. W., & Schotterer, U. (1999). Anthropogenic versus natural sources of atmospheric sulphate from an Alpine ice core. *Tellus B*, *51*(5), 938–951. https://doi.org/10.1034/j.1600-0889.1999.t01-4-00006.x

Shi, L., Allen, C. T., Ledford, J. R., Rodriguez-Morales, F., Blake, W. A., Panzer, B. G., Prokopiack, S. C., Leuschen, C. J., & Gogineni, S. (2010). Multichannel Coherent Radar Depth Sounder for NASA Operation Ice Bridge. *2010 IEEE International Geoscience and Remote Sensing Symposium (IGARSS)*, 1729–1732. https://doi.org/10.1109/IGARSS.2010.5649518

Sigl, M., Abram, N. J., Gabrieli, J., Jenk, T. M., Osmont, D., & Schwikowski, M. (2018a). 19th century glacier retreat in the Alps preceded the emergence of industrial black carbon deposition on high-alpine glaciers. *The Cryosphere*, *12*(10), 3311–3331. https://doi.org/10.5194/tc-12-3311-2018

Sigl, M., Abram, N. J., Gabrieli, J., Jenk, T. M., Osmont, D., & Schwikowski, M. (2018b). *Black carbon (rBC), bismuth, lead and others from 1741 to 2015 AD from Colle Gnifetti ice core (Swiss/Italian Alps)*. [dataset]. PANGAEA. https://doi.org/10.1594/PANGAEA.894788

Sihvola, A. H., & Kong, J. A. (1988). Effective permittivity of dielectric mixtures. *IEEE Transactions on Geoscience and Remote Sensing*, *26*(4), 420–429. https://doi.org/10.1109/36.3045

Smith, E. C., Baird, A. F., Kendall, J. M., Martín, C., White, R. S., Brisbourne, A. M., & Smith, A. M. (2017). Ice fabric in an Antarctic ice stream interpreted from seismic anisotropy. *Geophysical Research Letters*, *44*(8), 3710–3718. https://doi.org/10.1002/2016GL072093

Stern, W. (1929). *Versuch einer elektrodynamischen Dickenmessung von Gletschereis* [Doctoral dissertation, University of Frankfurt a. M.].

Still, H., Odolinski, R., Bowman, M. H., Hulbe, C., & Prior, D. J. (2023). Observing glacier dynamics with low-cost, multi-GNSS positioning in Victoria Land, Antarctica. *Journal of Glaciology*, 1–18. https://doi.org/10.1017/jog.2023.101

Stoll, N., Eichler, J., Hörhold, M., Erhardt, T., Jensen, C., & Weikusat, I. (2021). Microstructure, micro-inclusions, and mineralogy along the EGRIP ice core – Part 1: Localisation of inclusions and deformation patterns. *The Cryosphere*, *15*(12), 5717–5737. https://doi.org/10.5194/tc-15-5717-2021

Stolt, R. H. (1978). Migration by Fourier transform. *Geophysics*, *43*(1), 23–48. https://doi.org/10.1190/1.1440826

Sutter, J., Fischer, H., & Eisen, O. (2021). Investigating the internal structure of the Antarctic Ice Sheet: The utility of isochrones for spatiotemporal ice-sheet model calibration. *The Cryosphere*, *15*(8), 3839–3860. https://doi.org/10.5194/tc-15-3839-2021

Taylor, C., Robinson, T. R., Dunning, S., Rachel Carr, J., & Westoby, M. (2023). Glacial lake outburst floods threaten millions globally. *Nature Communications*, *14*(1), 487. https://doi.org/10.1038/s41467-023-36033-x

The Firn Symposium team, Amory, C., Buizert, C., Buzzard, S., Case, E., Clerx, N., Culberg, R., Datta, R. T., Dey, R., Drews, R., Dunmire, D., Eayrs, C., Hansen, N., Humbert, A., . . . Wouters, B. (2024). Firn on ice sheets. *Nature Reviews Earth & Environment*. https://doi.org/10.1038/s43017-023-00507-9

The IMBIE Team. (2020). Mass balance of the Greenland Ice Sheet from 1992 to 2018. *Nature*, *579*(7798), 233–239. https://doi.org/10.1038/s41586-019-1855-2

The IMBIE team. (2018). Mass balance of the Antarctic Ice Sheet from 1992 to 2017. *Nature*, *558*(7709), 219–222. https://doi.org/10.1038/s41586-018-0179-y

Ueltzhöffer, K. J., Bendel, V., Freitag, J., Kipfstuhl, S., Wagenbach, D., Faria, S. H., & Garbe, C. S. (2010). Distribution of air bubbles in the EDML and EDC (Antarctica) ice cores, using a new method of automatic image analysis. *Journal of Glaciology*, *56*(196), 339–348. https://doi.org/10.3189/002214310791968511

van Westen, R. M., Kliphuis, M., & Dijkstra, H. A. (2024). Physics-based early warning signal shows that AMOC is on tipping course. *Science Advances*, *10*(6), eadk1189. https://doi.org/10.1126/sciadv.adk1189

van den Broeke, M., Bamber, J., Ettema, J., Rignot, E., Schrama, E., van de Berg, W. J., van Meijgaard, E., Velicogna, I., & Wouters, B. (2009). Partitioning recent Greenland mass loss. *Science*, *326*(5955), 984–986. https://doi.org/10.1126/science.1178176

Vaňková, I., Cook, S., Winberry, J. P., Nicholls, K. W., & Galton-Fenzi, B. K. (2021). Deriving melt rates at a complex ice shelf base using in situ radar: Application to Totten Ice Shelf. *Geophysical Research Letters*, *48*(7), e2021GL092692. https://doi.org/10.1029/2021GL092692

Vaňková, I., Nicholls, K. W., Corr, H. F. J., Makinson, K., & Brennan, P. V. (2020a). Observations of tidal melt and vertical strain at the Filchner-Ronne Ice Shelf, Antarctica. *Journal of Geophysical Research: Earth Surface*, *125*(1), e2019JF005280. https://doi.org/10.1029/2019JF005280

Vaňková, I., Nicholls, K. W., Xie, S., Parizek, B. R., Voytenko, D., & Holland, D. M. (2020b). Depth-dependent artifacts resulting from ApRES signal clipping. *Annals of Glaciology*, *61*(81), 108–113. https://doi.org/10.1017/aog.2020.56

Vaňková, I., Voytenko, D., Nicholls, K. W., Xie, S., Parizek, B. R., & Holland, D. M. (2018). Vertical structure of diurnal englacial hydrology cycle at Helheim Glacier, East Greenland. *Geophysical Research Letters*, *45*(16), 8352–8362. https://doi.org/10.1029/2018GL077869

Wagenbach, D., Bohleber, P., & Preunkert, S. (2012). Cold, alpine ice bodies revisited: What may we learn from their impurity and isotope content? *Geografiska Annaler: Series A, Physical Geography*, *94*(2), 245–263. https://doi.org/10.1111/j.1468-0459.2012.00461.x

Wåhlin, A., Alley, K. E., Begeman, C., Hegrenæs, Ø., Yuan, X., Graham, A. G. C., Hogan, K., Davis, P. E. D., Dotto, T. S., Eayrs, C., Hall, R. A., Holland, D. M., Kim, T. W., Larter, R. D., . . . Heywood, K. J. (2024). Swirls and scoops: Ice base melt revealed by multibeam imagery of an Antarctic ice shelf. *Science Advances*, *10*(31), eadn9188. https://doi.org/10.1126/sciadv.adn9188

Waite, A., & Schmidt, S. (1962). Gross errors in height indication from pulsed radar altimeters operating over thick ice or snow. *Proceedings of the IRE*, *50*(6), 1515–1520. https://doi.org/10.1109/JRPROC.1962.288195

Walford, M. E. R., & Harper, M. F. L. (1981). The detailed study of glacier beds using radio-echo techniques. *Geophysical Journal International*, *67*(2), 487–514. https://doi.org/10.1111/j.1365-246X.1981.tb02762.x

Walford, M. E. R., Holdorf, P. C., & Oakberg, R. G. (1977). Phase-Sensitive radio-echo sounding at the Devon Island Ice Cap, Canada. *Journal of Glaciology*, *18*(79), 217–229. https://doi.org/10.3189/S0022143000021316

Wang, W., Li, J., & Zwally, H. J. (2012). Dynamic inland propagation of thinning due to ice loss at the margins of the Greenland ice sheet. *Journal of Glaciology*, *58*(210), 734–740. https://doi.org/10.3189/2012JoG11J187

Wang, Z., Chung, A., Steinhage, D., Parrenin, F., Freitag, J., & Eisen, O. (2023). Mapping age and basal conditions of ice in the Dome Fuji region, Antarctica, by combining radar internal layer stratigraphy and flow modeling. *The Cryosphere*, *17*(10), 4297–4314. https://doi.org/10.5194/tc-17-4297-2023

Weikusat, I., Jansen, D., Binder, T., Eichler, J., Faria, S. H., Wilhelms, F., Kipfstuhl, S., Sheldon, S., Miller, H., Dahl-Jensen, D., & Kleiner, T. (2017). Physical analysis of an Antarctic ice core—towards an integration of micro- and macrodynamics of polar ice. *Philosophical Transactions of the Royal Society A: Mathematical, Physical and Engineering Sciences*, *375*(2086), 20150347. https://doi.org/10.1098/rsta.2015.0347

Westhoff, J., Stoll, N., Franke, S., Weikusat, I., Bons, P., Kerch, J., Jansen, D., Kipfstuhl, S., & Dahl-Jensen, D. (2021). A stratigraphy-based method for reconstructing ice core orientation. *Annals of Glaciology*, *62*(85–86), 191–202. https://doi.org/10.1017/aog.2020.76

Winkelmann, R., Martin, M. A., Haseloff, M., Albrecht, T., Bueler, E., Khroulev, C., & Levermann, A. (2011). The Potsdam Parallel Ice Sheet Model (PISM-PIK) – Part 1: Model description. *The Cryosphere*, *5*(3), 715–726. https://doi.org/10.5194/tc-5-715-2011

Winter, A., Steinhage, D., Creyts, T. T., Kleiner, T., & Eisen, O. (2019). Age stratigraphy in the East Antarctic Ice Sheet inferred from radio-echo sounding horizons. *Earth System Science Data*, *11*(3), 1069–1081. https://doi.org/10.5194/essd-11-1069-2019

Winter, K., Woodward, J., Ross, N., Dunning, S. A., Hein, A. S., Westoby, M. J., Culberg, R., Marrero, S. M., Schroeder, D. M., Sugden, D. E., & Siegert, M. J. (2019). Radar-detected englacial debris in the West Antarctic Ice Sheet. *Geophysical Research Letters*, *46*(17–18), 10454–10462. https://doi.org/10.1029/2019GL084012

Wittlinger, G., & Farra, V. (2015). Evidence of unfrozen liquids and seismic anisotropy at the base of the polar ice sheets. *Polar Science*, *9*(1), 66–79. https://doi.org/10.1016/j.polar.2014.07.006

Wolovick, M. J., & Creyts, T. T. (2016). Overturned folds in ice sheets: Insights from a kinematic model of traveling sticky patches and comparisons with observations. *Journal of Geophysical Research: Earth Surface*, *121*(5), 1065–1083. https://doi.org/10.1002/2015JF003698

Xu, B., Lang, S., Cui, X., Li, L., Liu, X., Guo, J., & Sun, B. (2022). Focused synthetic aperture radar processing of ice-sounding data collected over East Antarctic Ice Sheet via spatial-correlation-based algorithm using fast back projection. *IEEE Transactions on Geoscience and Remote Sensing*, *60*, 1–9. https://doi.org/10.1109/TGRS.2022.3198432

Young, T. J., Martín, C., Christoffersen, P., Schroeder, D. M., Tulaczyk, S. M., & Dawson, E. J. (2021a). Rapid and accurate polarimetric radar measurements of ice crystal fabric orientation at the Western Antarctic Ice Sheet (WAIS) Divide ice core site. *The Cryosphere*, *15*(8), 4117–4133. https://doi.org/10.5194/tc-15-4117-2021

Young, T. J., Schroeder, D. M., Jordan, T. M., Christoffersen, P., Tulaczyk, S. M., Culberg, R., & Bienert, N. L. (2021b). Inferring ice fabric from birefringence loss in airborne radargrams: Application to the eastern shear margin of Thwaites Glacier, West Antarctica. *Journal of Geophysical Research: Earth Surface*, *126*(5), e2020JF006023. https://doi.org/10.1029/2020JF006023

Young, T. J., Schroeder, D. M., Christoffersen, P., Lok, L. B., Nicholls, K. W., Brennan, P. V., Doyle, S. H., Hubbard, B., & Hubbard, A. (2018). Resolving the internal and basal geometry of ice masses using imaging phase-sensitive radar. *Journal of Glaciology*, *64*(246), 649–660. https://doi.org/10.1017/jog.2018.54

Zeising, O., Gerber, T. A., Eisen, O., Ershadi, M. R., Stoll, N., Weikusat, I., & Humbert, A. (2023). Improved estimation of the bulk ice crystal fabric asymmetry from polarimetric phase co-registration. *The Cryosphere*, *17*(3), 1097–1105. https://doi.org/10.5194/tc-17-1097-2023

Zeising, O., Neckel, N., Dörr, N., Helm, V., Steinhage, D., Timmermann, R., & Humbert, A. (2024). Extreme melting at Greenland's largest floating ice tongue. *The Cryosphere*, *18*(3), 1333–1357. https://doi.org/10.5194/tc-18-1333-2024

Zeising, O., Steinhage, D., Nicholls, K. W., Corr, H. F. J., Stewart, C. L., & Humbert, A. (2022). Basal melt of the southern Filchner Ice Shelf, Antarctica. *The Cryosphere*, *16*(4), 1469–1482. https://doi.org/10.5194/tc-16-1469-2022

Zirizzotti, A., Urbini, S., Cafarella, L., & A.Baskaradas, J. (2010). Radar systems for glaciology. In G. Kouemou (Ed.), *Radar Technology*. InTech. https://doi.org/10.5772/7179